The Spectral Energy Distributions of Red Two Micron All Sky Survey Active Galactic Nuclei

THE SPECTRAL ENERGY DISTRIBUTIONS OF RED TWO MICRON ALL SKY SURVEY ACTIVE GALACTIC NUCLEI

Joanna Kuraszkiewicz[1], Belinda J. Wilkes[1], Gary Schmidt[2], Himel Ghosh[3], Paul S. Smith[2], Roc Cutri[4], Dean Hines[5],
Eric M. Huff[2,6], Jonathan C. McDowell[1], and Brant Nelson[4]

[1] Harvard-Smithsonian Center for Astrophysics, Cambridge, MA 02138, USA
[2] Steward Observatory, University of Arizona, Tucson, AZ 85721, USA
[3] Department of Astronomy, Ohio State University, Columbus, OH 43210-1173, USA
[4] IPAC, Caltech, MS 100-22, Pasadena, CA 91125, USA
[5] Space Science Institute, 4750 Walnut Street, Suite 205, Boulder, CO 80301, USA

ABSTRACT

We present infrared (IR) to X-ray spectral energy distributions (SEDs) for 44 red active galactic nuclei (AGNs) selected from the Two Micron All Sky Survey (2MASS) survey on the basis of their red $J - K_S$ color (> 2 mag) and later observed by *Chandra*. In comparison with optically-, radio-, and X-ray-selected AGNs, their median SEDs are red in the optical and near-IR (NIR) with little/no blue bump. Comparison of the various broadband luminosity ratios shows that the main differences lie at the blue end of the optical and in the NIR to far-IR ratios (when available), with the red 2MASS AGNs being redder than the other samples. It thus seems that NIR color selection isolates the reddest subset of AGNs that can be classified optically. The shape of the SEDs is generally consistent with modest absorption by gas (in the X-ray) and dust (in the optical–IR), as demonstrated by comparing the optical and NIR colors with a reddened median SED and observed optical+NIR to intrinsic X-ray ratios. The levels of obscuration, estimated from X-rays, far-IR, and our detailed optical/NIR color modeling, are all consistent implying $N_H \leqslant$ few $\times 10^{22}$ cm^{-2}. We present SED models that show how the AGN optical/NIR colors change due to differing amounts of reddening, AGN to host galaxy ratio, redshift, and scattered light emission, and apply them to the sources in the sample. We find that the 2MASS AGN optical color, $B - R$, and to a lesser extent the NIR color, $J - K_S$, are strongly affected by reddening, host galaxy emission, redshift, and in few, highly polarized objects also by scattered AGN light ($<2\%$ of intrinsic AGN light in the R band is scattered; this contribution becomes significant as the direct AGN light is absorbed). The lack of low equivalent widths in the distribution of the [O III] $\lambda 5007$ emission line implies a predominance of inclined objects in the red 2MASS sample. The obscuration/inclination of the AGN allows us to see weaker emission components which are generally swamped by the AGN.

Key words: galaxies: active – quasars: general

Online-only material: color figures

1. INTRODUCTION

The orientation dependence of the appearance of an active galactic nucleus (AGN) has been well known for many years. Radio observations clearly demonstrate extended, often very large structures that appear different as a function of their orientation (Barthel 1989) to our line of sight. Optical polarization reveals the presence of AGNs in scattered light that are not visible directly due to high obscuration (Antonucci & Miller 1985). These results led to the development of unification models which relate observationally different AGNs and radio galaxies to one another via viewing angle (Antonucci 1993). It is clear that obtaining an unbiased view of the AGN population is a challenge and, since most initial surveys were carried out in optical wavebands and based on a search for blue sources, obscured and/or edge-on AGNs have been missed. Even within the optically selected subset of AGNs, radio-X-ray spectral energy distributions (SEDs) show a wide variety of properties that affect selection (Elvis et al. 1994).

Evidence for a large, obscured subset of the AGN population which is mostly "missing" was demonstrated by modeling of the cosmic X-ray background (CXRB; Comastri et al. 1995; Gilli et al. 1999). Initial reports of a red, obscured population missed

by traditional optical surveys was based on radio-selected AGNs (Webster et al. 1995; Kim & Elvis 1999). Detailed study has shown that these can be explained in terms of an additional, red nonthermal synchrotron continuum component, linked to the radio emission (Francis et al. 2001; but see Richards et al. 2002). The importance of this particular set of red AGNs to the population seems not to be large (Boyle & di Matteo 1995). Much effort has been made both to reduce selection bias in sample selection and to understand the angular dependence and thus the relation between those selected in different wavebands. The Sloan Digital Sky Survey (SDSS), while still an optical survey, has developed sophisticated color selection techniques which successfully reveal AGNs with a variety of nonstellar colors, many much redder than found in previous optically selected samples of AGNs (Richards et al. 2002). The Two Micron All Sky Survey (2MASS) revealed a significant subset of predominantly broad-lined AGNs through their red near-IR (NIR) colors. Their number density rivals that of optically selected AGNs at low redshifts (Cutri et al. 2002). In addition, the typically high optical polarization (Smith et al. 2002, 2003) of the 2MASS AGNs suggests substantial obscuration around the nuclear energy source. *Chandra* observations show weak, hard X-ray emission compared with normal, low-redshift AGNs (Wilkes et al. 2002). These properties suggest that they are AGNs obscured at a level intermediate between the well-studied, unobscured, broad-lined AGNs revealed by optical surveys

---

[6] Current address: Department of Astronomy, University of California, Berkeley, CA 94720, USA.

(face-on in the Unified Scheme; Antonucci & Miller 1985) and the obscured narrow-lined AGNs believed to be viewed edge-on.

The advent of the Great Observatories: *Chandra* and *Spitzer* over the past 5–10 years have facilitated many deeper, multi-wavelength surveys that have extended sufficiently deeply into the population to reveal large numbers of previously unknown AGNs with properties very different from the traditional broad emission-line AGNs (Alexander et al. 2003; Polletta et al. 2006, 2007). These new AGNs also extend the observed properties of AGN SEDs over a much wider range. With a large number of new candidate AGNs covering a wide range of properties, the quest to understand the AGN population and the nature and variety of the structure of their central regions is only now beginning in earnest. The most recent version of CXRB models, based on results from the current deep X-ray surveys (Gilli et al. 2007), includes a population of moderately obscured AGNs, which may be explained by a combination of the new AGN candidates, but still calls for a significant highly obscured population that has not yet been found, although recent *Spitzer* and *Chandra* results are suggestive (Daddi et al. 2008; Fiore et al. 2008).

The importance of red AGNs to the total population thus remains uncertain. At low redshift, the 2MASS red AGNs may account for as much as 20% of the AGN population (Francis et al. 2004), and likely represent a significant subset of the moderately obscured AGNs required by current CXRB models. Many of these red AGNs, especially those with lower obscuration ($A_V \lesssim$ few), should be picked up by the SDSS. However, those AGNs with higher obscuration whose optical colors are dominated by the host galaxy will not, since their colors will lie too close to the stellar locus to be classified as a quasar.[7] The high-redshift population corresponding the red 2MASS sources is not yet known due to the combination of the bright magnitude limit of the 2MASS survey and the lower efficiency of the NIR selection as the optical emission shifts into the observed waveband. They most likely overlap with higher-redshift populations of red AGNs being found in the longer-wavelength *Spitzer* surveys (Treister et al. 2006; Lacy et al. 2007).

As transition objects between unobscured, face-on and Compton-thick, edge-on sources, the 2MASS red AGNs provide a unique view of the AGN central regions. The partial obscuration of the bright, direct AGN light facilitates study of weaker components (Pounds et al. 2005; Wilkes et al. 2008) and thus of the complex structure of material close to the nucleus that not only reprocesses the light, but also may be integral to fueling the AGN itself, as well as the powerful radio jets and outflowing material we observe on a wide variety of spatial scales.

We have embarked on a multiwavelength study of a bright subset of the 2MASS red AGNs that have been observed by *Chandra*. In this paper, we present our X-ray and optical data, collated with data from the literature to generate IR–X-ray

SEDs. The properties of the SEDs are presented including previously unpublished optical spectra, polarimetry and spectrophotometry, and measurements of the continuum and emission-line properties. These properties are compared with those of more traditional AGNs to identify similarities and differences and therefore probe the structure and properties of the AGNs. We conclude that, orientation-dependent obscuration, host galaxy properties and scattering effects are factors in determining the SED properties of these red AGNs. However, as we show in a companion paper (Kuraszkiewicz et al. 2009), where we perform principal component analysis (PCA) on the SED and emission-line properties, the $L/L_{\rm Edd}$ ratio is a dominant factor.

2. THE SAMPLE

The 2MASS (Skrutskie et al. 2006) is yielding a catalog of NIR-selected AGNs (Cutri et al. 2002) larger and deeper than those discovered by *IRAS* (Soifer et al. 1984). Spectroscopic follow-up of red candidates, selected to have $J - K_S > 2$ from the high galactic latitude 2MASS Point Source Catalog, reveals that ∼75% are previously unidentified emission-line AGNs, with ∼85% showing broad optical emission lines (Types 1–1.9: Seyfert 1, intermediate and QSO), and the remainder being narrow-line objects (Type 2: Seyfert 2, QSO 2, and LINER; Cutri et al. 2002). They span a redshift range $0.1 < z < 2.3$ with median ∼0.25. The inferred surface density is ∼0.5 deg^{-2} brighter than $K_s < 14.5$ mag, higher than that of optically selected AGNs at the same IR magnitudes and indicating that 2MASS may reveal >25,000 such objects over the sky (R. M. Cutri et al. 2009, in preparation). Red $J - K_S$ selection is inhomogeneous with redshift, since the $J - K_S$ color is an NIR spectral index for $z < 0.25$, an IR-to-optical index for $0.25 < z < 1.2$, and an optical spectral index for $z > 1.2$. Hence reddened AGNs (that show no 1 μm inflection) will be picked up by the red $J - K_S$ selection at all redshifts, while the "normal" blue AGNs, with red NIR colors, will be only picked up at low redshift (see also Figure 5 in Barkhouse & Hall 2001, who find a large number of blue AGNs with $J - K_S > 2$ at $z < 0.5$). In this paper we study a well-defined, flux-limited, color-selected subset of 44 red 2MASS AGNs (for a list of objects see Table 1) selected to have $B - K_S > 4.3$ and $K_S < 13.8$. This subsample is representative[8] of the low-redshift red AGN population, with $0 < z < 0.37$, a full range of spectral types (7 Type 1, 11 Type 2, and 26 intermediate-type sources), a wide range of observed K_S-band-to-X-ray (1 keV) slopes: $1.1 \lesssim \alpha_{KX} \lesssim 2$, and a broad range of observed optical polarization fraction at R band $0 < P(\%) < 13$. This subset was observed by *Chandra* and was shown to be relatively X-ray faint and hard in comparison with optically selected broad-line AGNs (Wilkes et al. 2002). Assuming the spectral hardness is due to absorption, deduced equivalent hydrogen column densities are at the level of log $N_{\rm H} \sim 21$–23 and absorption-corrected X-ray fluxes are at the low end of the expected range based on the assumption that the K magnitude is intrinsic (Wilkes et al. 2002), even lower if the K magnitude is also affected by absorption.

3. MULTIWAVELENGTH OBSERVATIONS

3.1. Chandra Data

Chandra ACIS-I/ACIS-S observations have been obtained for all 44 2MASS AGNs in our sample. The observations

---

[7] We have cross-correlated the 44 red 2MASS AGNs in our sample with the SDSS dr6 database and found 23 2MASS AGNs in the area covered by the SDSS. Using the *ugri* color–color, low-*z* QSO selection criteria from Richards et al. (2002) we find that six of these sources would have been excluded : three (13%) blue sources (NLS1/BALQSOs with optical colors dominated by AGN emission) due to $(u - g) < 0.5$ criterion and three (13%) red sources (with optical colors dominated by host galaxy and $A_V > 10$) whose optical colors fall too close (within the 2σ–4σ error) to the stellar locus. However, the red 2MASS sample used here is not complete and these conclusions should be treated with caution.

[8] However, sources that fulfil the color selection but are not detected at *J* are not included in the sample.

Table 1
2MASS Red AGN Observed with *Chandra*

Name 2MASSJ (1)	Redshift (2)	Type (3)	$P \pm \sigma_P$ (%) (4)	Reference (5)	$J - K_S$ (6)	$B - R$ (7)	$B - K_s$ (8)	B^{USNO} (9)	R^{USNO} (10)	B^{sc} (11)	R_1^{sc} (12)	R_2^{sc} (13)	I^{sc} (14)	J (15)	H (16)	K_S (17)
00070361+1554237	0.114	1.5	0.99 ± 0.81	2	2.099	1.43	5.21	17.40[a]	16.10[a]	18.379	17.363	16.946	16.632[a]	15.264 ± 0.058	14.278 ± 0.059	13.165 ± 0.044
00505569+2933280	0.136	2.0	2.47 ± 0.49	2	2.137	1.31	5.59	18.90	16.20[a]	18.846	17.883	17.535	16.853	15.390 ± 0.068	14.289 ± 0.061	13.253 ± 0.043
01083514+2148184	0.285	1.9	5.07 ± 0.11	3	2.685	1.83	5.79	20.00	17.30[a]	19.420	17.465	17.588	17.267	16.317 ± 0.128	14.877 ± 0.075	13.632 ± 0.050
01572104+1712481	0.213	2.0	1.44 ± 0.47	2	2.706	1.59	6.84	20.50	18.70	20.016	18.869	18.424	17.997	15.886 ± 0.082	14.557 ± 0.060	13.180 ± 0.042
02215061+1327407	0.140	1.8	0.39 ± 0.24	2	2.365	2.09	5.71	18.90	16.40[a]	18.986	17.392	16.892	16.522	15.646 ± 0.082	14.532 ± 0.085	13.281 ± 0.053
02343064+2438355[b]	0.310	1.5	2.57 ± 0.46	2	2.160	1.18	4.57	21.00[a]	21.00[a]	18.391			17.209	16.958	15.983 ± 0.095	14.942 ± 0.081	13.823 ± 0.052
03485765+1255474	0.210	2.0	2.23 ± 0.73	2	3.294	1.54	6.77	19.70[a]	18.60	20.328	19.057	18.789	18.120	16.851 ± 0.153	15.344 ± 0.109	13.557 ± 0.050
04092486+0758563	0.091	1.5	1.14 ± 0.18	1	2.167	1.20	4.98	17.40	16.20	17.651	16.648[a]	17.197[a]	16.604[a]	14.842 ± 0.054	13.828 ± 0.054	12.675 ± 0.043
04203206−2047592	0.208	1.5	13.02 ± 0.05	1	2.573	1.88	5.85	18.30[a]	17.50	19.015	17.311	17.135	16.738	15.739 ± 0.059	14.613 ± 0.063	13.166 ± 0.034
07482519+6947121	0.231	1.9	2.25 ± 0.34	1	3.193	1.47	6.60	18.70[a]	18.20	19.740	18.285	18.268	17.532	16.329 ± 0.096	14.652 ± 0.060	13.136 ± 0.037
09184860+2117170	0.149	1.5	6.49 ± 0.02	3	2.232	1.47	5.78	18.50	16.40	18.358	16.948	16.887	16.237	14.814 ± 0.042	13.740 ± 0.044	12.582 ± 0.034
09384445+0057156	0.170	1.2	6.36 ± 0.10	1	2.412	1.35	6.45	17.20	15.80	18.234	17.277	16.885	15.623	14.198 ± 0.044	13.126 ± 0.046	11.786 ± 0.037
09550454+1705564	0.139	1.2	0.34 ± 0.18	2	2.028	1.20	4.69	18.10	17.00	17.245[a]	17.216	17.075	15.985[a]	15.439 ± 0.070	14.409 ± 0.054	13.411 ± 0.040
10212671+6311302	0.138	2.0	1.02 ± 0.32	1	2.585	1.46	5.94	18.80	17.60	19.122	17.955	17.666	17.315	15.769 ± 0.085	14.526 ± 0.081	13.184 ± 0.049
10272497+1219196	0.231	1.5	1.34 ± 0.10	2	2.025	1.49	5.00	19.40	17.20	18.296	17.071	16.810	16.149	15.320 ± 0.042	14.422 ± 0.050	13.295 ± 0.036
10404364+5934092[c]	0.148	1.9	1.44 ± 0.31	1	3.020	1.50	7.43	18.40[a]	17.50[a]	19.246	18.087	17.741	16.600	14.836 ± 0.069	13.455 ± 0.055	11.816 ± 0.034
10494335+5837504	0.115	1.8	2.7[d]	4	1.964	...	4.62	17.70	14.60[e]	...	...	...	...	15.043 ± 0.169	14.086 ± 0.119	13.079 ± 0.066
10514425+3539306	0.158	1.9	1.18 ± 0.11	3	2.080	1.42	5.49	18.60	16.00	19.020	18.046	17.602	16.336	15.610 ± 0.061	14.548 ± 0.058	13.530 ± 0.044
11275112+2432078	0.088	1.5	0.59 ± 0.17	1, 2	1.969	...	4.94	17.90[a]	15.90[a]	...	...	...	...	14.933 ± 0.058	13.951 ± 0.057	12.964 ± 0.047
12301552+0302546	0.137	1.5	2.21 ± 0.19	1	2.387	1.42	5.79	17.50[a]	16.20[a]	18.518	16.049	17.099	15.707	15.113 ± 0.063	13.995 ± 0.055	12.726 ± 0.045
12434935−0802483	0.192	1.9	2.27 ± 0.23	1	2.420	1.43	5.54	18.00[a]	16.90	18.603	17.184	17.174	16.344	15.484 ± 0.075	14.428 ± 0.054	13.064 ± 0.046
12580745+2329216[b]	0.259	1.0	1.00 ± 0.03	3	2.043	0.68	3.62[f]	18.00[a]	17.10[a]	17.079	16.800	16.395	15.837	15.505 ± 0.062	14.653 ± 0.055	13.462 ± 0.043
13000534+1632149	0.080	2.0	2.76 ± 0.01	3	2.165	1.63	5.83	17.10	14.00[a]	17.699	16.463	16.067	15.088	14.035 ± 0.043	13.016 ± 0.042	11.870 ± 0.032
13070062+2338052	0.275	2.5[g]	2.45 ± 0.63	2	3.314	1.73	7.36	21.03	19.51	20.829	19.202	19.096	18.361	16.786 ± 0.165	15.090 ± 0.076	13.472 ± 0.045
13170436−1739126	0.216	1.5	4.24 ± 0.22	1	2.073	1.47	5.66	17.20[a]	15.70[a]	18.480	...	17.012	15.819	14.896 ± 0.050	14.001 ± 0.060	12.823 ± 0.043
13503735−0632153	0.229	1.0	1.71 ± 0.07	1	2.273	1.20	4.19	16.80	15.60	16.234[a]			15.156[a]	14.298[a]	14.322 ± 0.049	13.305 ± 0.052	12.049 ± 0.037
14025120+2631175	0.187	1.0	0.21 ± 0.21	2	2.081	0.64	4.41	17.10	16.50	16.230[a]	16.205[a]	15.586[a]	15.737	14.771 ± 0.042	13.758 ± 0.040	12.690 ± 0.032
14184990+6804097	0.077	1.5	0.73 ± 0.09	1	2.131	1.48	5.25	17.00[a]	14.50[a]	17.853	16.996	16.371	15.932	14.730 ± 0.057	13.582 ± 0.052	12.599 ± 0.040

Table 1
(continued)

Name 2MASSJ	Redshift	Type	$P \pm \sigma_P$ (%)	Reference	$J - K_S$	$B - R$	$B - K_s$	B^{USNO}	R^{USNO}	B^{sc}	R_1^{sc}	R_2^{sc}	I^{sc}	J	H	K_S
(1)	(2)	(3)	(4)	(5)	(6)	(7)	(8)	(9)	(10)	(11)	(12)	(13)	(14)	(15)	(16)	(17)
14533150+1353585	0.139	2.0/LINER	0.31 ± 0.19	1	2.194	1.57	5.59	18.50	15.60[a]	18.702	17.051	17.133	16.443	15.304 ± 0.079	14.352 ± 0.065	13.110 ± 0.047
15011320+2329082	0.258	1.0	3.04 ± 0.04	3	2.490	1.85	6.07	20.30	17.30	19.563	17.986	17.714	16.867	15.983 ± 0.098	14.722 ± 0.076	13.493 ± 0.054
15070636−1225158	0.185	2.0	1.61 ± 0.18	1	2.711	1.71	6.05	18.20	17.10	18.596	17.153	16.886	16.362	15.254 ± 0.054	13.934 ± 0.051	12.543 ± 0.038
15114126+0518092	0.085	1.8	0.46 ± 0.08	1	2.639	1.36	5.83	16.70[a]	15.30[a]	17.993	16.430	16.634	15.886	14.798 ± 0.058	13.580 ± 0.055	12.159 ± 0.026
15165323+1900482	0.190	1.0	9.27 ± 0.01	3	2.168	1.30	6.06	15.80	14.50	17.440[a]	16.638[a]	16.244[a]	13.134[a]	13.544 ± 0.029	12.613 ± 0.031	11.376 ± 0.025
15362773+6146417	0.173	2.0	0.78 ± 0.10	1	2.209	1.67	5.30	17.40[a]	15.40[a]	18.378	17.286	16.710	16.048	15.287 ± 0.060	14.164 ± 0.057	13.078 ± 0.036
16370022+2221140	0.211	1.5	2.49 ± 0.04	3	2.040	1.53	5.57	19.00	17.10	19.207	17.869	17.681	16.918	15.673 ± 0.074	14.616 ± 0.065	13.633 ± 0.053
16593976+1834367	0.170	1.5	5.33 ± 0.03	3	2.139	1.70	5.48	18.20	16.50	. . .	. . .	. . .	. . .	15.071 ± 0.044	14.118 ± 0.041	12.932 ± 0.035
17144278+2602485[c]	0.163	1.0	0.86 ± 0.33	2	2.210	0.52	4.38	17.50	16.60	. . .	. . .	. . .	. . .	15.329 ± 0.056	14.242 ± 0.054	13.119 ± 0.039
17550379+6751083	0.243	2.0	0.54 ± 0.60	1	2.789	1.33	7.34	19.30[a]	18.60	20.425	19.246	19.096	18.015	15.879 ± 0.080	14.403 ± 0.051	13.090 ± 0.038
20242055−5723436	0.353	1.9	. . .	. . .	2.173	2.34	5.87	18.00	16.40	18.936	16.307	16.595	16.806[a]	15.238 ± 0.062	14.099 ± 0.070	13.065 ± 0.050
20255073−4958129	0.320	1.5	. . .	. . .	2.122	1.70	5.65	17.90[a]	16.70	18.777	16.907	17.074	16.309	15.245 ± 0.059	14.260 ± 0.071	13.123 ± 0.047
22220221+1952316	0.366	1.5	11.04 ± 0.04	3	3.050	1.36	6.17	19.50	18.30	19.392	18.361	18.035	17.616	16.274 ± 0.118	14.787 ± 0.082	13.224 ± 0.042
22222113+1959474	0.211	1.5	1.02 ± 0.02	3	2.062	0.98	4.61	17.50	16.60	16.762[a]	16.379[a]	15.781[a]	14.848[a]	14.951 ± 0.055	14.108 ± 0.056	12.889 ± 0.036
22255425+1958372	0.147	2.0	0.28 ± 0.03	3	1.903	1.42	4.87	18.80[a]	15.50[a]	18.513	17.466	17.091	16.490	15.548 ± 0.089	14.768 ± 0.104	13.645 ± 0.061
23444958+1221432	0.199	1.0	1.01 ± 0.24	2	1.997	1.37	5.46	17.40	16.10	18.425	16.347	17.054	16.090	14.966 ± 0.053	14.122 ± 0.045	12.969 ± 0.038

Notes. Columns: (1) 2MASS object name; (2) spectroscopic redshift; (3) optical type; (4) degree of linear polarization at R photometric band; (5) references from which the degree of polarization in (4) is quoted: 1, this paper; 2, Smith et al. (2002); 3, Smith et al. (2003); 4, Schmidt et al. (2007); (6) $J - K_S$ color; (7) $B - R$ color (SuperCOSMOS magnitudes were used, unless they did not fit to the overall SED, then USNO-A2 magnitudes were used); (8) $B - K_S$ color (SuperCOSMOS B magnitude was generally used unless it did not fit to the overall SED, then USNO-A2 magnitude was used); (9), (10) B and R magnitudes from the USNO-A2.0 Catalog (Monet et al. 1998); (11)–(14) B, R (two epochs), and I magnitudes from the SuperCOSMOS Sky Survey (Hambly et al. 2001a, 2001b, 2001c); (15)–(17) J, H, K_S magnitudes are from the 2MASS database. We adopt 0.4 mag errors for USNO-A2 photometry and 0.3 mag for SuperCOSMOS photometry (see Section 3.3 for details).
[a] This magnitude was not used in compiling the SEDs as it is inconsistent with the overall SED shape.
[b] SuperCOSMOS photometry of 0234+2438 and 1258+2329 is inconsistent with the steep, blue optical spectrum.
[c] USNO-A2 photometry of 1040+5934 and 1714+2602 is inconsistent with the optical spectrum.
[d] The degree and position angle of polarization in this object vary with λ implying two scattering components: one with $P \geqslant 8\%$ and the other dominating at $\lambda \lesssim 4500$ Å with $P > 20\%$.
[e] The Digital Palomar Observatory Sky Survey catalog quotes a 14.6 mag in R filter for this object. This number is incorrect and shown by the SDSS to be 16.11 mag. The DPOSS number is possibly for an object $1''$ away.
[f] The $B - K_S$ color was calculated using SuperCOSMOS B magnitude; when USNO B magnitude is used $B - K_S = 4.54$ mag.
[g] Spectrum used to classify the optical type of this object does not cover Hβ wavelengths; it does, however, cover Hα which is narrow, hence Type 2.5.

Table 2
HST Spectroscopy

Name	Date	Instrument	Grating
0918+2117	2002 Apr 27	*HST*/STIS	PRISM
0955+1705	2002 Apr 26	*HST*/STIS	PRISM
1516+1900	2002 Feb 11	*HST*/STIS	G140L, G230L
1714+2602	2002 Jan 25	*HST*/STIS	PRISM
2222+1959	2002 May 3	*HST*/STIS	PRISM

were designed to detect each AGN based on its K_S magnitude combined with the lowest known X-ray to K flux ratio for an AGN at the time $\alpha_{KX} = 2$ (MKN 231; Turner 1999). A wide range of net counts was found, from three sources with few (∼5) counts to several with >200 counts, implying a range of ×100 in observed X-ray to K flux across the sample (Wilkes et al. 2002).

Spectral fits were made to the *Chandra* X-ray data to provide the best estimate of the X-ray fluxes. For the higher count sources ($\gtrsim 80$, referred to as "*C*" fits), a simple power-law plus rest-frame absorption was fitted with both parameters free. For sources with counts between ∼ 30–80, the power-law was fixed to $\Gamma = 2$ but the N_H remained free ("*B*" fits). For the lowest count sources, $\lesssim 30$ counts ("*A*" fits), fits were made using a power law with $\Gamma = 2$ and $N_H = 7.6 \times 10^{21}$ cm^{-2} (the median absorption from the *C* fits). In a few cases where the *B* fits did not converge, *A* fits were made despite higher counts. This fitting is described and presented in more detail in a companion paper (B. J. Wilkes et al. 2008, in preparation), where we present the X-ray fluxes used in the SEDs. When available, we also included in the SEDs the X-ray fluxes from the WGA Catalog of *ROSAT* point sources[9] (White et al. 1994).

3.2. HST Spectroscopy

The ultraviolet (UV) spectrophotometry for nine objects was obtained using the Space Telescope Imaging Spectrograph (STIS) aboard the *Hubble Space Telescope* (*HST*). Only five objects had sufficient signal to noise to be used here. Four objects were observed with the PRISM grating, and one (1516+1900) was observed with the higher-resolution gratings G140L and

---

[9] http://heasarc.gsfc.nasa.gov/W3Browse/all/wgacat.html

G230L (see Table 2 for details). No emission-line analysis was done for these spectra, since so few objects were detected. For the purpose of including the *HST* spectra in the SEDs, the underlying continuum was fitted using the IRAF[10] "continuum" task. The fitted continuum was then binned into broader wavelength bands to delineate the SEDs.

3.3. Optical and IR Photometry

The NIR flux densities for the sample were compiled using the J, H, K_S magnitudes from the 2MASS Point Source Catalog. The optical (B, R, I) photometry was taken from the Digital Palomar Observatory Sky Survey (DPOSS I and II) photographic plates and retrieved through the SuperCOSMOS Sky Survey (Hambly et al. 2001a, 2001b, 2001c) or/and the USNO-A2.0 Catalog (Monet et al. 1998). A 0.3 magnitude uncertainty was adopted for SuperCOSMOS data and 0.4 mag uncertainty for USNO-A2 data. These uncertainties account for the photometric accuracy of the plates and the different photographic emulsions used at different epochs. The 2MASS and DPOSS magnitudes for our red 2MASS AGN sample objects are presented in Table 1 (note that in most cases SuperCOSMOS R magnitudes were taken at two epochs denoted here as R1 and R2). A small number of AGNs were also found in the SDSS database. These objects are presented in Table 3. In a few cases, optical (B, R) photometry from the DPOSS II plates differed substantially from the SDSS data (u, g, r, i magnitudes were translated to B, V, R following Jester et al. 2005) or from the shape of the optical spectrum described below. For such objects (see Table 1) only SDSS photometry was used for the SEDs, as it is a CCD-based photometry with typical accuracies of 0.03 mag.

3.4. Optical Spectrophotometry

Optical spectroscopy of the red 2MASS AGN was obtained between 1998 and 2005, primarily with the Norris Spectrograph on the Palomar 200 inch Hale telescope and/or the Boller & Chivens Spectrograph on the 90 inch Bok telescope at Kitt

---

[10] IRAF (Image Reduction and Analysis Facility) is distributed by the National Optical Astronomy Observatory, which is operated by the Association of Universities for Research in Astronomy, Inc., under cooperative agreement with the National Science Foundation.

Table 3
SDSS Photometry

Name	u	g	r	i	B	V	R	I
0007+1554	18.695 ± 0.035	17.594 ± 0.008	16.840 ± 0.005	16.072 ± 0.005	17.891	17.172	16.610	15.787
0938+0057[a]	18.927 ± 0.021	17.584 ± 0.005	16.664 ± 0.004	15.702 ± 0.003	17.922	17.076	16.440	15.477
1021+6311	20.879 ± 0.117	19.123 ± 0.015	18.113 ± 0.010	17.530 ± 0.009	19.532	18.568	18.076	17.386
1027+1219[a]	20.082 ± 0.044	18.525 ± 0.008	17.441 ± 0.005	16.833 ± 0.005	18.900	17.931	17.430	16.723
1040+5934	20.450 ± 0.165	18.664 ± 0.011	17.712 ± 0.008	16.876 ± 0.006	19.078	18.139	17.551	16.679
1049+5837[b]	18.568 ± 0.061	17.192 ± 0.008	16.344 ± 0.005	15.604 ± 0.004	17.536	16.721	16.170	15.367
1051+3539	20.105 ± 0.147	18.291 ± 0.011	17.125 ± 0.007	16.469 ± 0.006	18.709	17.655	17.135	16.393
1230+0302[a]	18.815 ± 0.028	17.819 ± 0.007	17.103 ± 0.005	16.400 ± 0.005	18.098	17.417	16.880	16.103
1402+2631	17.146 ± 0.009	16.971 ± 0.004	16.609 ± 0.004	16.087 ± 0.004	17.111	16.753	16.284	15.639
1501+2329	21.042 ± 0.188	19.220 ± 0.015	17.809 ± 0.008	17.189 ± 0.007	19.640	18.456	17.951	17.234
1511+0518	18.721 ± 0.028	17.190 ± 0.004	16.301 ± 0.004	15.804 ± 0.004	17.560	16.698	16.239	15.611
1637+2221	20.125 ± 0.086	18.710 ± 0.013	17.583 ± 0.008	16.988 ± 0.009	19.061	18.094	17.598	16.899
1659+1834[a]	19.024 ± 0.028	17.992 ± 0.006	17.069 ± 0.005	16.455 ± 0.004	18.277	17.482	16.979	16.267
1714+2602	17.060 ± 0.010	17.027 ± 0.005	16.927 ± 0.005	16.564 ± 0.005	17.143	16.945	16.537	16.006

Notes. u, g, r, i magnitudes are from SDSS. These are converted to B, V, R, I magnitudes using transformations for quasars from Jester et al. (2005).
[a] These objects appear in the SDSS Quasar Catalog by Schneider et al. (2007).
[b] SDSS photometry does not fit the overall SED.

Table 4
Optical Spectroscopy

Name	Date (yyyy/mm/dd)	Telescope	Slit ($''$)	Factor[a]
0007+1554a	1998/07/17	Palomar200/NORRIS	2	1.8
0007+1554b	2001/10/18	KPNO/BOK	4.5	1.7
0050+2933	1998/01/24	FAST/Tillinghast	3	1.2
0108+2148	1998/11/15	Palomar200/NORRIS	2	1.2
0157+1712	1998/09/20	Palomar200/NORRIS	2	1.0
0221+1327	1998/11/15	Palomar200/NORRIS	2	2.0
0234+2438	1998/09/20	Palomar200/NORRIS	2	0.65
0348+1255	1998/11/14	Palomar200/NORRIS	2	2.0
0409+0758a	1998/07/17	Palomar200/NORRIS	2	0.4
0409+0758b	2005/12/30	KPNO/BOK	3	1.0
0420−2047	2000/12/29	Palomar200/NORRIS	2	2.2
0748+6947a	2000/01/11	Palomar200/NORRIS	2	2.5
0748+6947b	2005/04/14, 15	KPNO/BOK	2	2.5
0918+2117a	1999/01/10	Palomar200/NORRIS	2	1.3
0918+2117b	2001/10/18	KPNO/BOK	4.5	2.0
0938+0057	2000/12/02	KPNO/BOK	2.5	1.0
0955+1705a	1997/12/24	Palomar200/NORRIS	2	0.7
0955+1705b	2002/01/13	KPNO/BOK	4.5	0.6
1021+6311a	2000/12/27	Palomar200/NORRIS	2	1.0
1021+6311b	2005/04/13	KPNO/BOK	1	2.0
1027+1219a	1998/11/14	Palomar200/NORRIS	2	0.65
1027+1219b	2005/04/14, 15	KPNO/BOK	2	1.0
1040+5934a	2000/12/28	Palomar200/NORRIS	2	0.18
1040+5934b	2005/04/14	KPNO/BOK	2	1.3
1049+5837	2001/02/16	Palomar200/NORRIS	2	3.8
1051+3539a	1999/01/10	Palomar200/NORRIS	2	3.3
1051+3539b	2002/01/13	KPNO/BOK	4.5	4.2
1127+2432a	2001/04/11	KPNO/BOK	2.5	2.4
1127+2432b	2005/12/30	KPNO/BOK	3	1.0
1230+0302a	2001/02/16	Palomar200/NORRIS	2	3.7
1230+0302b	2005/04/13	KPNO/BOK	2	4.0
1243−0802a	2000/05/01	SSO/2.3 m	2	2.5
1243−0802b	2005/12/30	KPNO/BOK	3	1.0
1258+2329	1998/03/01	FAST/Tillinghast	3	1.0
1300+1632a	1998/07/19	Palomar200/NORRIS	2	4.0
1300+1632b	2002/01/13	KPNO/BOK	4.5	4.0
1307+2338	2001/09/06	Keck II	2	1.2
1317−1739	2001/04/11	SSO/2.3 m	2	3.2
1350−0632	2000/01/06	SSO/2.3 m	4.5	2.7
1402+2631	1998/03/03	FAST/Tillinghast	3	1.2
1418+6804a	2000/07/03	Palomar200/NORRIS	2	1.4
1418+6804b	2005/04/13, 15	KPNO/BOK	1	1.3
1453+1353a	1998/09/21	Palomar200/NORRIS	2	3.2
1453+1353b	2005/04/13, 15	KPNO/BOK	1	1.0
1501+2329a	1998/09/21	Palomar200/NORRIS	2	0.7
1501+2329b	2001/03/30	MMT	2	2.2
1507−1225a	2000/01/05	SSO/2.3 m	2	2.2
1507−1225b	2005/04/13	KPNO/BOK	2	4.6
1511+0518a	2001/04/12	KPNO/BOK	2.5	0.6
1511+0518b	2005/12/30	KPNO/BOK	3	1.0
1516+1900a	2002/01/16	KPNO/BOK	4.5	1.0
1516+1900b	1998/03/03	FAST/Tillinghast	3	1.0
1536+6146[b]	2001/06/12	KPNO/BOK	2.5	...
1637+2221	1998/09/21	Palomar200/NORRIS	2	3.0
1659+1834	1998/09/20	Palomar200/NORRIS	2	1.0
1714+2602a	1998/07/17	Palomar200/NORRIS	2	1.0
1714+2602b	2001/10/18	KPNO/BOK	4.5	0.7
1755+6751a	2000/07/02	Palomar200/NORRIS	2	0.9
1755+6751b	2005/04/13, 14	KPNO/BOK	2	1.0
2024−5723	2000/01/02	SSO/2.3 m	2	1.4
2025−4958	2000/01/01	SSO/2.3 m	2	1.0
2222+1952	1998/07/17	Palomar200/NORRIS	2	0.7
2222+1959a	1998/07/17	Palomar200/NORRIS	2	1.0
2222+1959b	2001/10/18	KPNO/BOK	4.5	0.63
2225+1958	1998/07/17	Palomar200/NORRIS	2	0.5
2344+1221	1998/09/20	Palomar200/NORRIS	2	1.0

Notes.
[a] Factor by which the spectrum was multiplied (grayshifted) to match the optical photometry.
[b] Spectrum not used in SEDs and emission-line measurements.

Peak. Six spectra were taken with the 2.3 m telescope at the Siding Spring Observatory and four spectra with the FAST Spectrograph on the 1.5 m Tillinghast telescope, one spectrum on the 6.5 m MMT telescope on Mt. Hopkins, and one spectrum with the Keck II telescope on Mauna Kea. Details of the observations are shown in Table 4 and the spectra are presented in Figure 1 (right column). For the purpose of including the optical spectra in the SEDs, we used (as before for the *HST* spectra) the IRAF "continuum" task to obtain the underlying continuum, which was then binned into broader wavelength bands to delineate the SEDs. Due to slit losses and observations made under nonphotometric conditions, some of our optical spectra had to be grayshifted to match the optical photometry from DPOSS and/or SDSS surveys (the factor by which the spectra were multiplied is also shown in Table 4). Where possible, the long wavelength end of the grayshifted spectrum was also matched with a linear interpolation between the *J* and *I* photometry (spectra ending at wavelengths between the *J* and *I* filters) or between *I* and *R* photometry (spectra ending at shorter wavelengths). In a few cases where the *I* photometry did not fit the overall SED, the long wavelength end of the spectrum was grayshifted to agree with a linear interpolation between *J* and *R* photometry.

3.5. Optical Polarimetry

Optical polarimetry was obtained as an extension of the detailed optical study of red 2MASS AGNs by Smith et al.

Table 5
New Polarimetry of 2MASS AGN[a]

Object	Date (yyyy/mm/dd)	P [b] $\pm \sigma_P$ (%)	θ [b] $\pm \sigma_\theta$ (deg)
0409+0758	2003/09/22	1.14 ± 0.18	135.7 ± 4.4
0420−2047	2003/09/22	10.94 ± 0.31	158.3 ± 0.8
	2003/10/29	13.02 ± 0.05	156.7 ± 0.1
0748+6947	2004/02/22	1.34 ± 0.48	142.4 ± 11.4
	2005/04/14, 15	2.25 ± 0.34	129.3 ± 4.3
0938+0057	2004/02/21	7.12 ± 0.24[c]	49.3 ± 1.0[c]
	2004/04/25	6.36 ± 0.10	50.9 ± 0.5
1021+6311	2004/02/21	1.02 ± 0.32	2.1 ± 8.9
	2005/04/13	2.22 ± 0.55	8.6 ± 7.1
1027+1219	2005/04/14, 15	1.34 ± 0.10	147.5 ± 2.1
1040+5934	2004/02/21	1.43 ± 0.31	66.0 ± 6.1
	2005/04/14	1.77 ± 0.29	91.4 ± 4.7
1127+2432	2004/02/21	0.59 ± 0.17	60.3 ± 8.2
1230+0302	2004/02/21	2.21 ± 0.19	17.8 ± 2.4
	2005/04/13	3.15 ± 1.25	10.3 ± 11.4
1243−0802	2004/02/22	2.27 ± 0.23	67.6 ± 2.8
1317−1739	2004/02/22	4.24 ± 0.22	73.7 ± 1.5
	2004/04/25	4.91 ± 0.15	75.9 ± 0.9
1350−0632	2004/05/23	1.71 ± 0.07	172.7 ± 1.1
1418+6804	2004/05/23	1.28 ± 0.18	63.2 ± 4.1
	2005/04/13, 15	0.73 ± 0.09	65.9 ± 3.3
1453+1353	2005/04/13, 15	0.31 ± 0.09	63.2 ± 8.6
1507−1225	2004/05/23	1.62 ± 0.18	84.7 ± 3.2
	2005/04/13	2.35 ± 1.20	123.6 ± 14.6
1511+0518	2004/05/23	0.46 ± 0.08	4.0 ± 5.2
1536+6146	2004/04/26	0.78 ± 0.10	17.8 ± 3.7
1755+6751	2003/09/22	0.54 ± 0.60	...
	2005/04/13, 14	1.56 ± 0.35	24.8 ± 6.4

Notes.
[a] Measurements are in the *R* photometric band.
[b] P is linear polarization in the *R* band; θ is the position angle of the polarization.
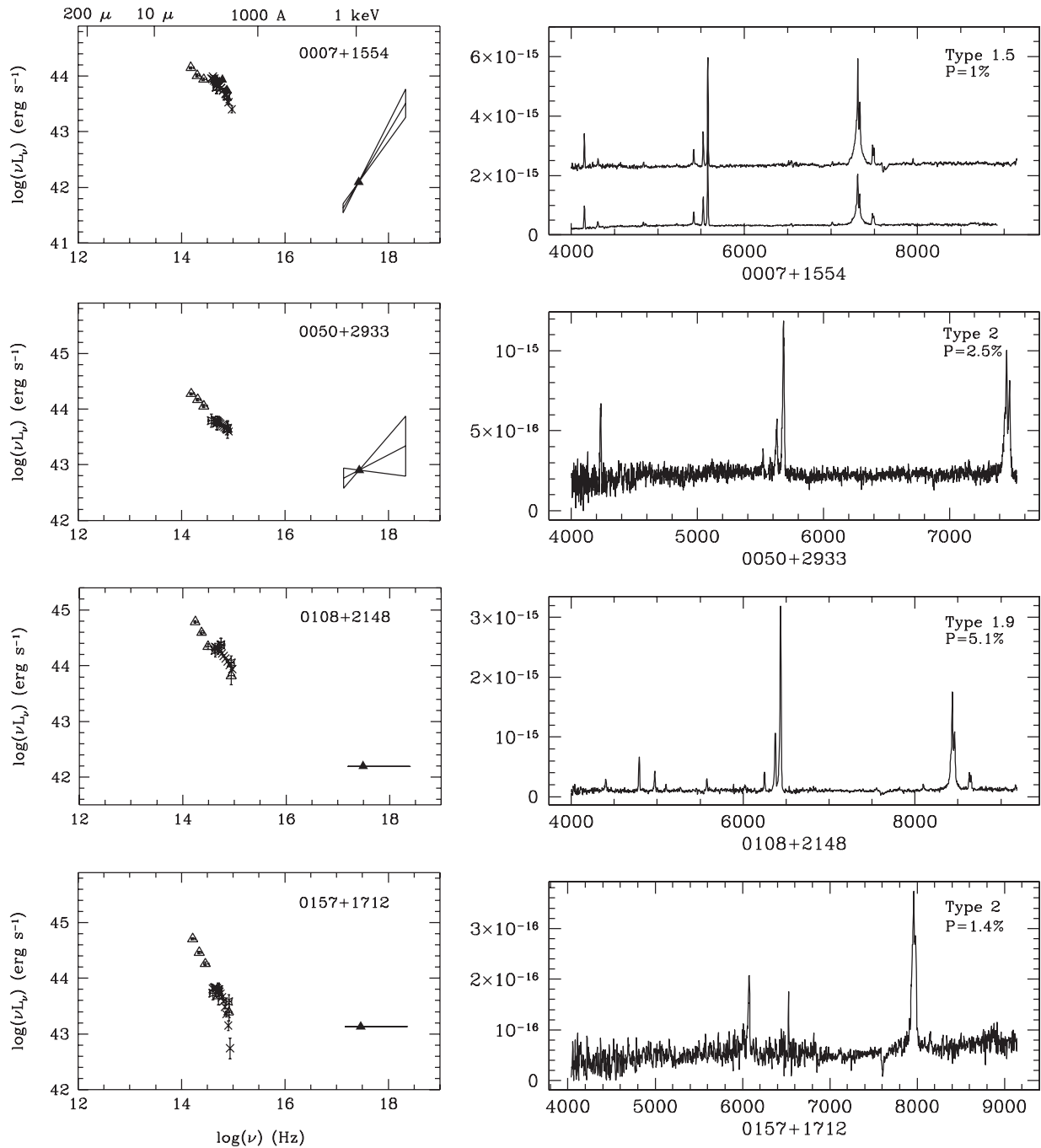[c] Measured in the *V* photometric band.

Figure 1. Left column: rest-frame far-IR to X-ray SEDs for AGN in our sample. The host galaxies have not been subtracted. *IRAS*, 2MASS (J, H, K_S), and USNO-A2.0 (B, R) photometry are indicated by open triangles, SDSS and *Chandra* data by filled triangles, SuperCOSMOS photometry and *HST* spectrophotometry by stars, optical spectrophotometry by crosses, and *ROSAT* data by open pentagons. Right column: optical spectra on an F_λ (erg s^{-1} cm^{-2} Å^{-1}) vs. λ (Å) scale. If two spectra are present for one object then spectrum "a" from Table 4 is grayshifted and plotted above spectrum "b."

(2002, 2003), and details of the observational procedures can be found in those publications. Briefly, *R*-band imaging polarimetry was generally acquired for all sources using the CCD Imaging/Spectropolarimeter SPOL (Schmidt et al. 1992) at the 2.3 m Bok telescope. This was followed up by spectropolarimetry of the more strongly polarized targets at the 6.5 m MMT and 2.3 m Bok telescope to ascertain the polarization characteristics of the continuum versus broad and narrow emission lines. In a few cases, only spectropolarimetry was acquired and the quoted *R*-band values were derived from an integration of the results over the filter passband. The spectropolarimetric observations also provide high-quality, low-resolution ($\sim$15 Å) total

flux spectra, suitable for accurate optical classification and the measurement of line strengths, host galaxy contributions, and continuum slopes as well as suitable for including in the SEDs. The new polarimetry results are listed in Table 5. Figure 2 shows the spectropolarimetry data for those sources where it has not been previously published. For those objects having linear polarization previously measured by Smith et al. (2002, 2003) we recall these values in Column 4 of Table 1.

3.6. IRAS Photometry

Twelve sources in our red 2MASS AGN sample were found to have *IRAS* fluxes in the Faint Source Catalog version 2 (Moshir
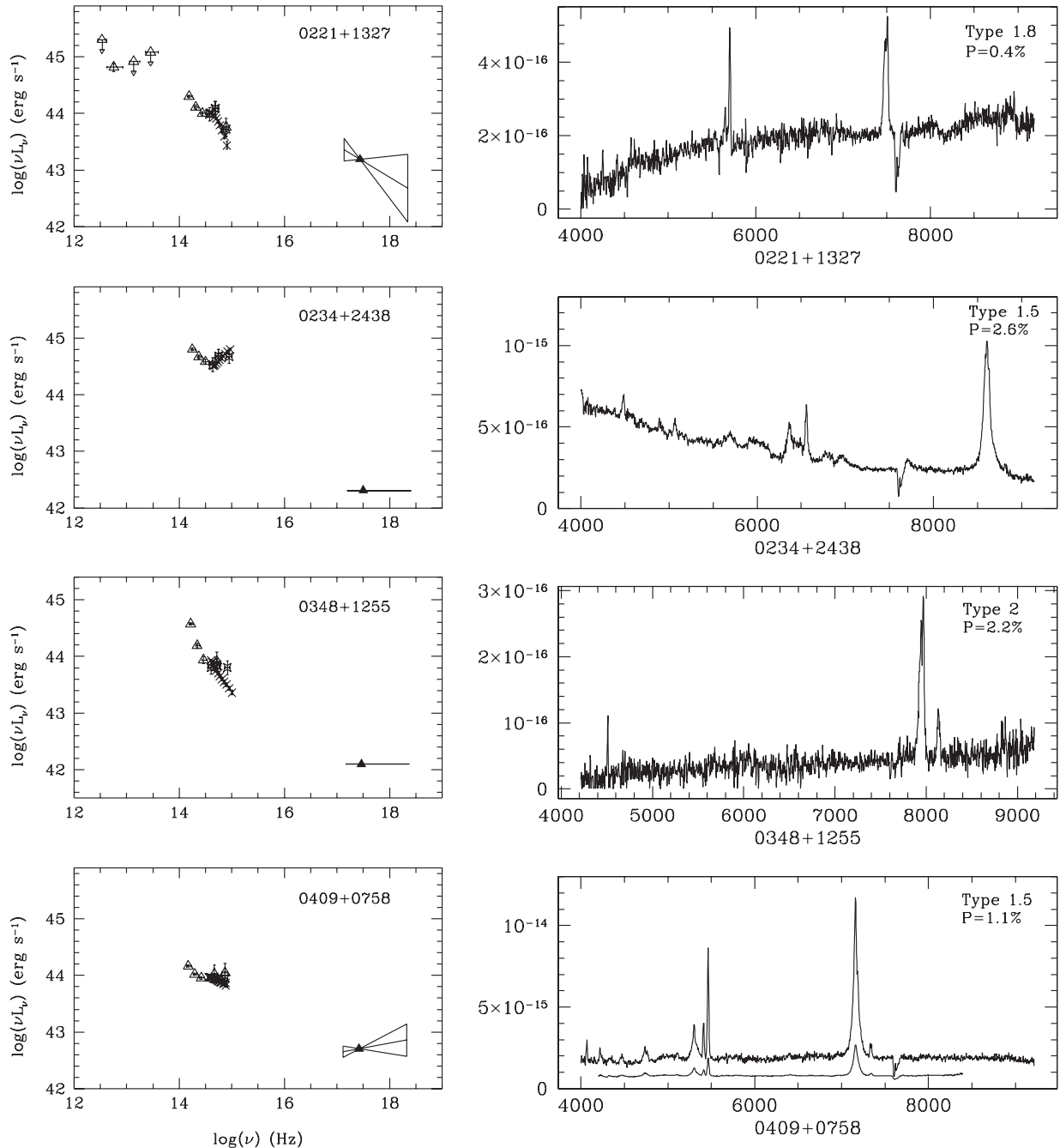
Figure 1. (Continued)

et al. 1990). The 12, 25, 60, and 100 μm fluxes are presented in Table 6.

4. IR TO X-RAY SPECTRAL ENERGY DISTRIBUTIONS (SEDS)

The multiwavelength data described in the Section 3 were combined to generate SEDs of the red 2MASS objects together with the far-IR to X-ray data available in the NASA/IPAC Extragalactic Database (NED). A summary of all references used in the compilation of the SEDs is presented in Table 7. The full SEDs (except for the X-rays, which were corrected for N_H during X-ray spectral fitting described in Section 3.1) were then corrected for galactic extinction using the Galactic neutral hydrogen column from Dickey & Lockman (1990) and Stark et al. (1992) and assuming a fixed conversion of

$N(\text{H\,I})/E(B-V) = 5.0 \times 10^{21}$ cm^2 mag^{-1} (Burstein & Heiles 1978). After this, the data were shifted to the rest frame using a cosmological model with $\Omega_o = 1$ and $H_o = 75$ km s^{-1} Mpc^{-1} (Mould et al. 2000). No k-corrections and no assumptions about the intrinsic spectrum were required, since we are working with the complete SEDs. No host galaxy subtraction was made, since there is no consistent way to estimate the strength of the host galaxy emission for the full sample. The resulting, rest-frame far-IR to X-ray SEDs of the full sample are presented in Figure 1.

4.1. Comparison of the SEDs and Broadband Optical and IR Colors with Other AGN Samples

In Figure 3(a) we plot the median SED for our red 2MASS AGN normalized at 1.5 μm, together with the 68, 90, and 100 Kaplan–Neilson percentile envelopes (Feigelson & Nelson 1985;
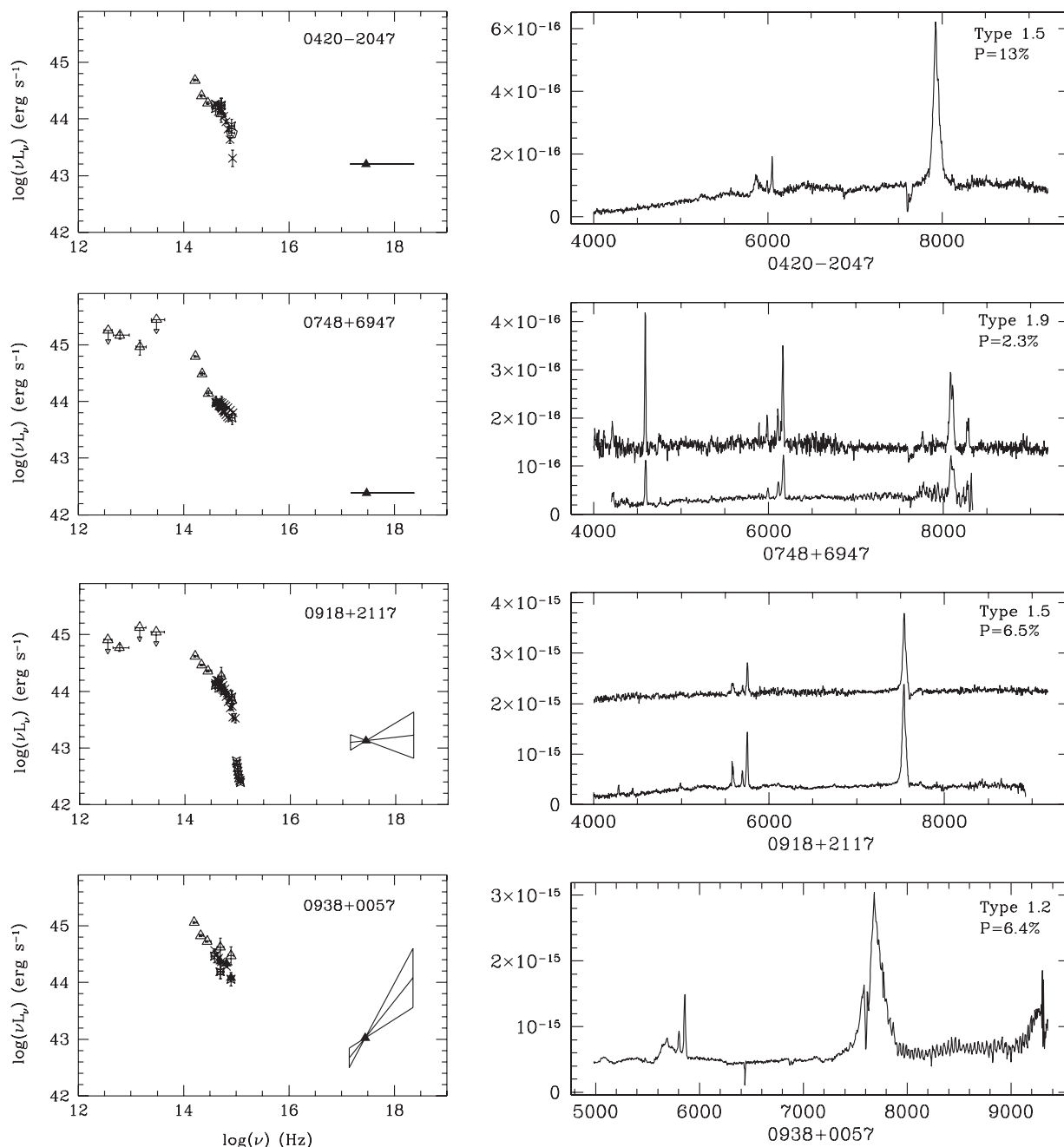
Figure 1. (Continued)

Isobe et al. 1986), which take into account upper limits in the data (mostly in IRAS data). In Figure 3(b), we compare this median with the medians (redshift and host galaxy corrected) of the optically- and radio-selected AGNs from Elvis et al. (1994; hereafter E94) and the hard-X-ray-selected AGNs from Kuraszkiewicz et al. (2003; hereafter the *HEAO* sample). All three samples have similar redshift ranges $0 < z \lesssim 0.37$. Optical selection will pick mostly unobscured ($N_{\rm H} < 10^{21}\,{\rm cm}^{-2}$) AGNs. Hard-X-ray selection, on the other hand, has the advantage of finding samples that are more representative of the real AGN population, since it is less biased by the effects of obscuration along the line of sight. It is apparent from the comparison of the medians of these three samples that in the optical and UV, the 2MASS median occupies the redder envelope of the *HEAO* (i.e., representative) AGN sample, while the optically selected AGN

occupy the bluer envelope. The median 2MASS AGN SED is also relatively bright in the IR (has a more pronounced IR bump due to the $J - K_S > 2$ selection) in comparison with the other two samples.

Differences in the median SEDs are confirmed by comparing the distributions of various (octave and decade) IR, optical, and UV luminosity ratios in these samples. We find that the distributions of the following luminosity ratios were significantly different (>99% in the two-tailed K–S test) when the 2MASS sample was compared with the *HEAO* sample and the optically/radio-selected E94 sample: $L(0.2$–$0.4\ \mu{\rm m})/L(0.4$–$0.8\ \mu{\rm m})$, $L(0.2$–$0.4\ \mu{\rm m})/L(0.8$–$1.6\ \mu{\rm m})$, $L(0.4$–$0.8\ \mu{\rm m})/L(0.8$–$1.6\ \mu{\rm m})$, and $L(1$–$10\ \mu{\rm m})/L(10$–$100\ \mu{\rm m})$. These distributions are presented in Figure 4. Objects that have *HST* spectra are marked with "x." Note that, although the 3000 Å bump (Wills et al.
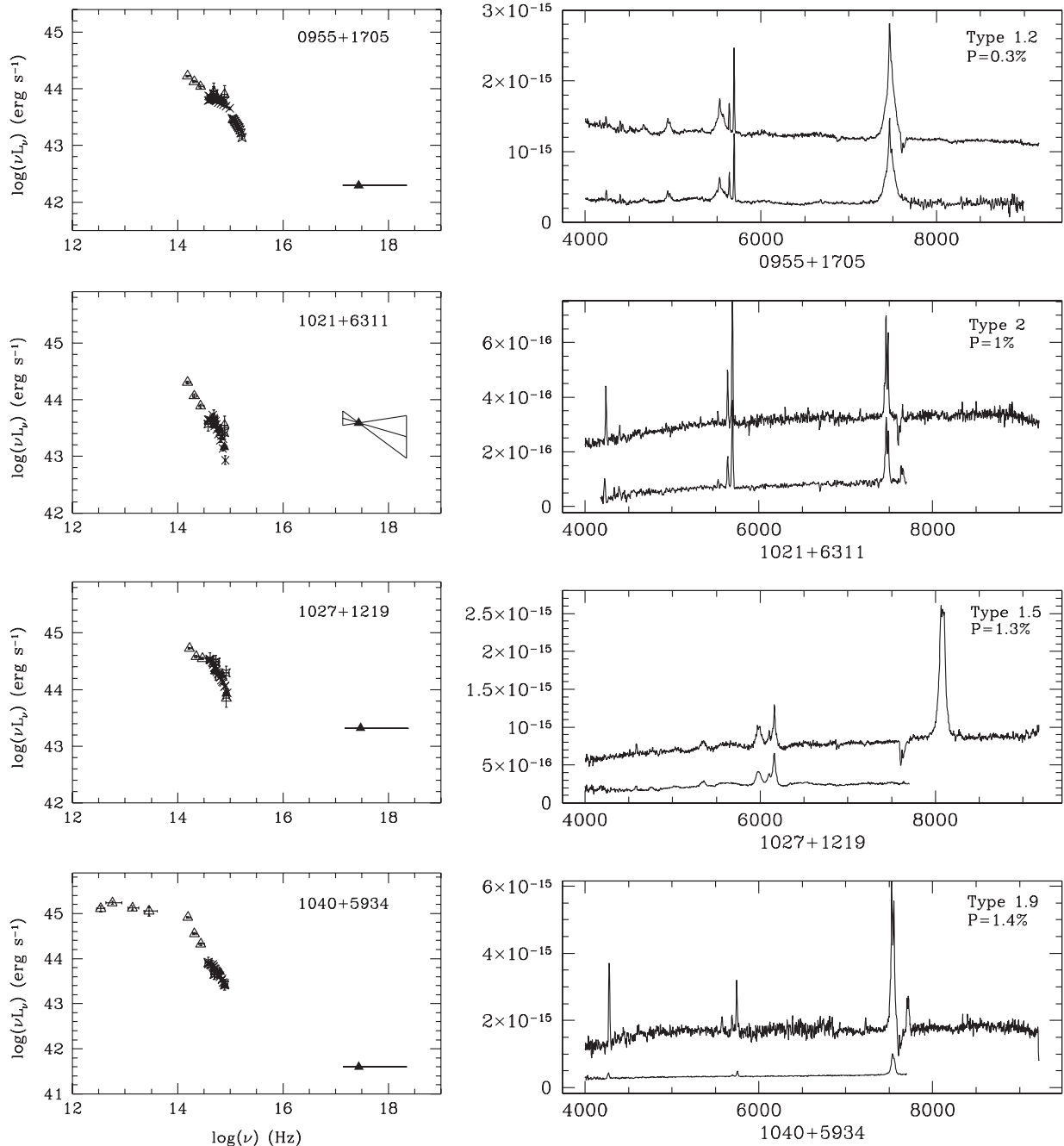
Figure 1. (Continued)

Table 6
IRAS Photometry

| Name	12 μm (Jy)	25 μm (Jy)	60 μm (Jy)	100 μm (Jy)
0221+1327	< 0.119	< 0.172	0.327 ± 0.052	< 1.674
0748+6947	< 0.098	0.068 ± 0.020	0.261 ± 0.039	< 0.531
0918+2117	< 0.097	< 0.245	0.260 ± 0.039	< 0.597
1040+5934	0.100 ± 0.023	0.248 ± 0.025	0.770 ± 0.054	0.954 ± 0.143
1307+2338	< 0.101	< 0.173	0.721 ± 0.058	0.686 ± 0.123
1418+6804	< 0.073	0.054 ± 0.015	0.191 ± 0.032	0.651 ± 0.163
1453+1353	< 0.094	0.149 ± 0.037	0.556 ± 0.061	0.702 ± 0.168
1507−1225	< 0.146	0.283 ± 0.051	0.666 ± 0.087	< 0.717
1536+6146	< 0.079	0.143 ± 0.014	0.286 ± 0.029	< 0.459
1637+2221	< 0.056	< 0.105	0.179 ± 0.036	< 0.086
1659+1834	< 0.119	0.163 ± 0.024	0.277 ± 0.041	< 0.853
2024−5723	0.097 ± 0.023	0.193 ± 0.029	0.273 ± 0.049	< 0.737
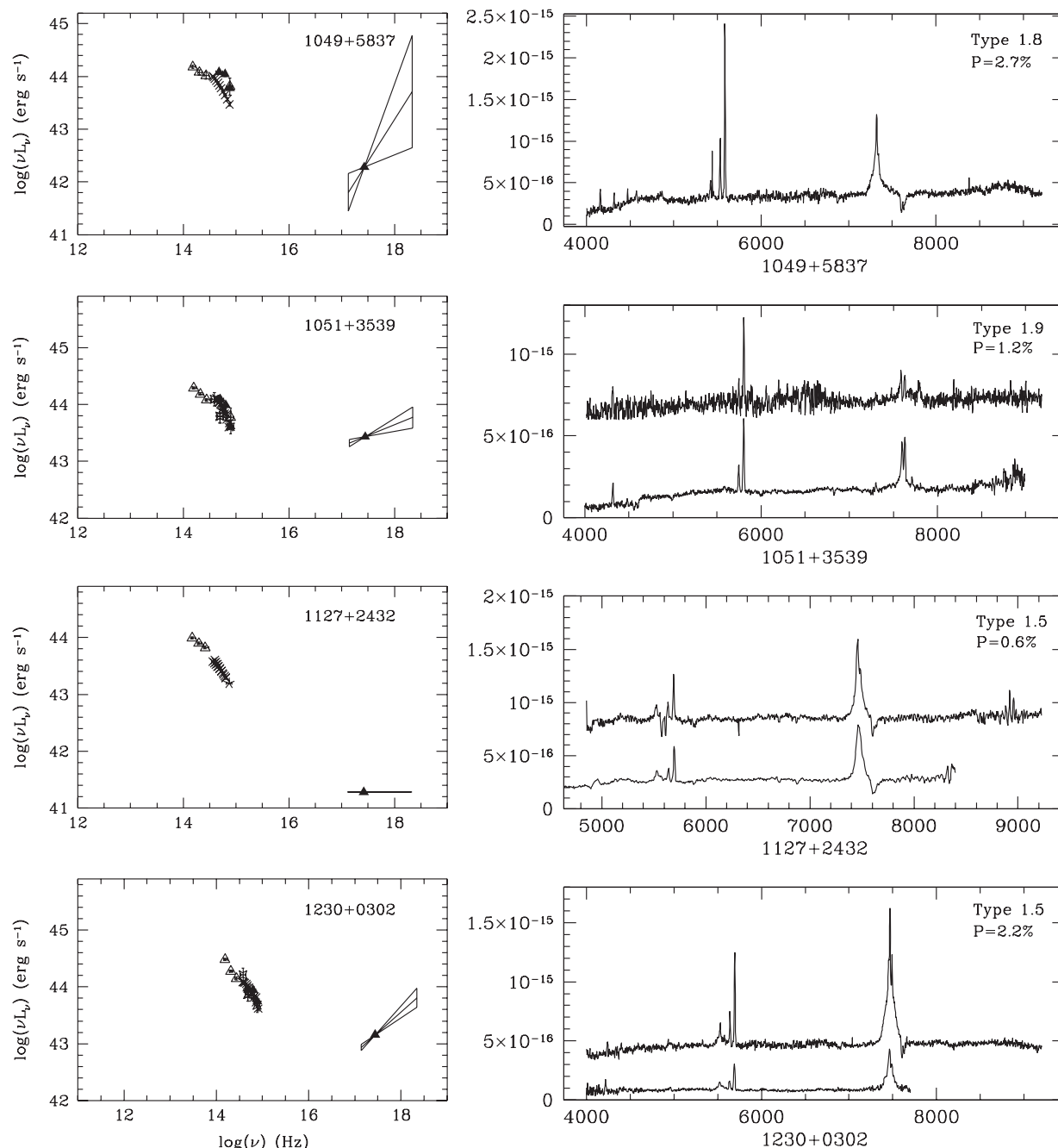
Figure 1. (Continued)

1985) lies in the 0.2–0.4 μm range, our luminosity estimates are not contaminated by this bump since our SEDs were compiled using the underlying continuum fits to the optical/UV spectra (Sections 3.2 and 3.4). Objects with high polarization values ($P > 3\%$) are marked in Figure 4 with "p." If higher polarization in these objects was due to the presence of larger amounts of dust in the nucleus (as in the case of the highly polarized 2MASX J10494334+5837501, see Schmidt et al. 2007), we might expect to find all highly polarized objects among the reddest AGNs in our 2MASS sample. However, these objects span a range of UV/opt and opt/IR ratios (see Figure 4) and do not tend to group toward the reddest 2MASS objects. It is possible that the reddest (most obscured) AGNs do not show high polarization because scattered nuclear light is diluted by host galaxy emission (Smith et al. 2002, 2003) and/or

the optical/IR colors of the highly polarized sources are made bluer by host galaxy emission and the scattered light itself, which certainly is the case in our 2MASS AGN as discussed in Section 5.2.

We present in Figure 5 a comparison of the NIR-selected 2MASS sample with the hard-X-ray (Kuraszkiewicz et al. 2003) and optically and radio-selected (E94) samples in a two-color ($L(0.4–0.8\ \mu m)/L(0.8–1.6\ \mu m)$ versus $L(0.2–0.4\ \mu m)/L(0.8–1.6\ \mu m)$) diagram. The hard-X-ray-selected *HEAO* sample covers the entire range of parameter space occupied by the other two samples. The 2MASS sample includes the redder objects, and the optical/radio-selected sample has bluer colors with little overlap between the two. Clearly, the hard-X-ray (2–10 keV) selection of the *HEAO* sample is an efficient way to select AGN regardless of their optical/IR properties.
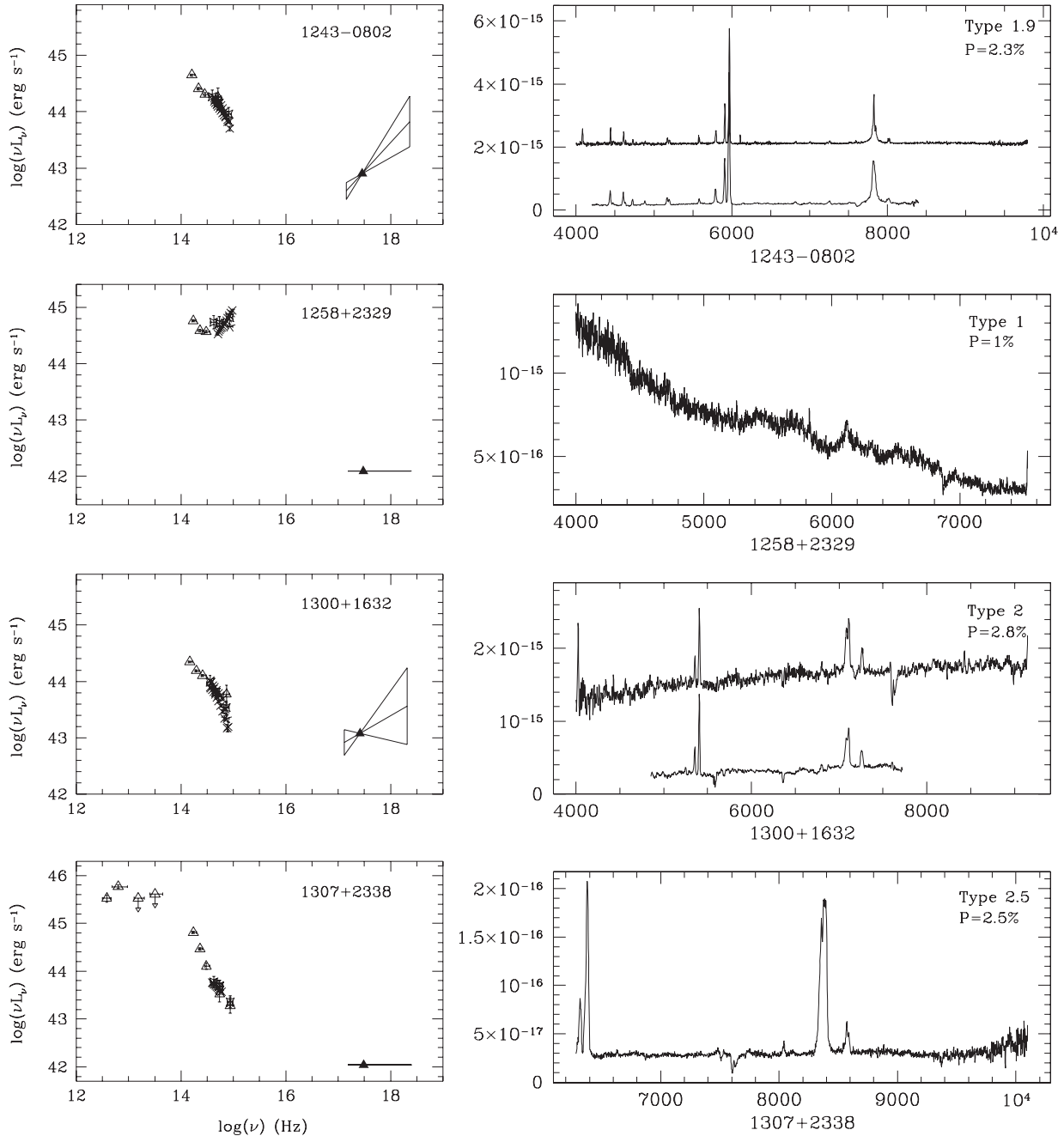
Figure 1. (Continued)

5. ANALYSIS OF THE OPTICAL/IR COLORS

5.1. The 2MASS $B - R$ and $J - K_S$ Colors

In Figure 6, we plot the observed $J - K_S$ versus $B - R$ colors of the red 2MASS AGN and compare them with the observed colors of E94 AGN (crosses). The colors of both samples have not been corrected for host galaxy emission. The conversion from $J - K$ to $J - K_S$ colors of the E94 AGN was made using transformations from Bessell (2005). The 2MASS objects cover the $B - R$ colors of the E94 sample and extend toward redder optical colors. The $J - K_S$ colors are on average 1 mag redder than those of the optical/radio-selected AGN (E94) due to the red $J - K_S > 2$ selection.

Let us assume that the optical/radio-selected AGNs from E94 are representative of the unobscured AGN population. We show their median colors ($z = 0$ SED, individual SEDs comprising the median were corrected for host galaxy emission) in Figure 6 by a filled circle and denote by "$A_V = 0$." The long-dash-short-dash line shows the change in color when this median SED is obscured by Milky Way dust, with extinctions ranging from $A_V = 0$ to 4 mag (filled circles at the loci). The dotted line shows these colors for an AGN at $z = 0.3$, i.e., at a redshift close to the highest redshift in the 2MASS sample (see Section 5.5 for a detailed discussion of the redshift dependence of optical/IR colors). We see that the range of $B - R$ colors shown by the red 2MASS AGN translates into A_V between 0 and 3 mag, while the range of $J - K_S$ colors translates into A_V between 0 to 10 mag (0 to 7 mag for an AGN with $z = 0.3$). Possible explanations for finding lower extinction estimated from the $B - R$ color than the $J - K_S$ color include the following.
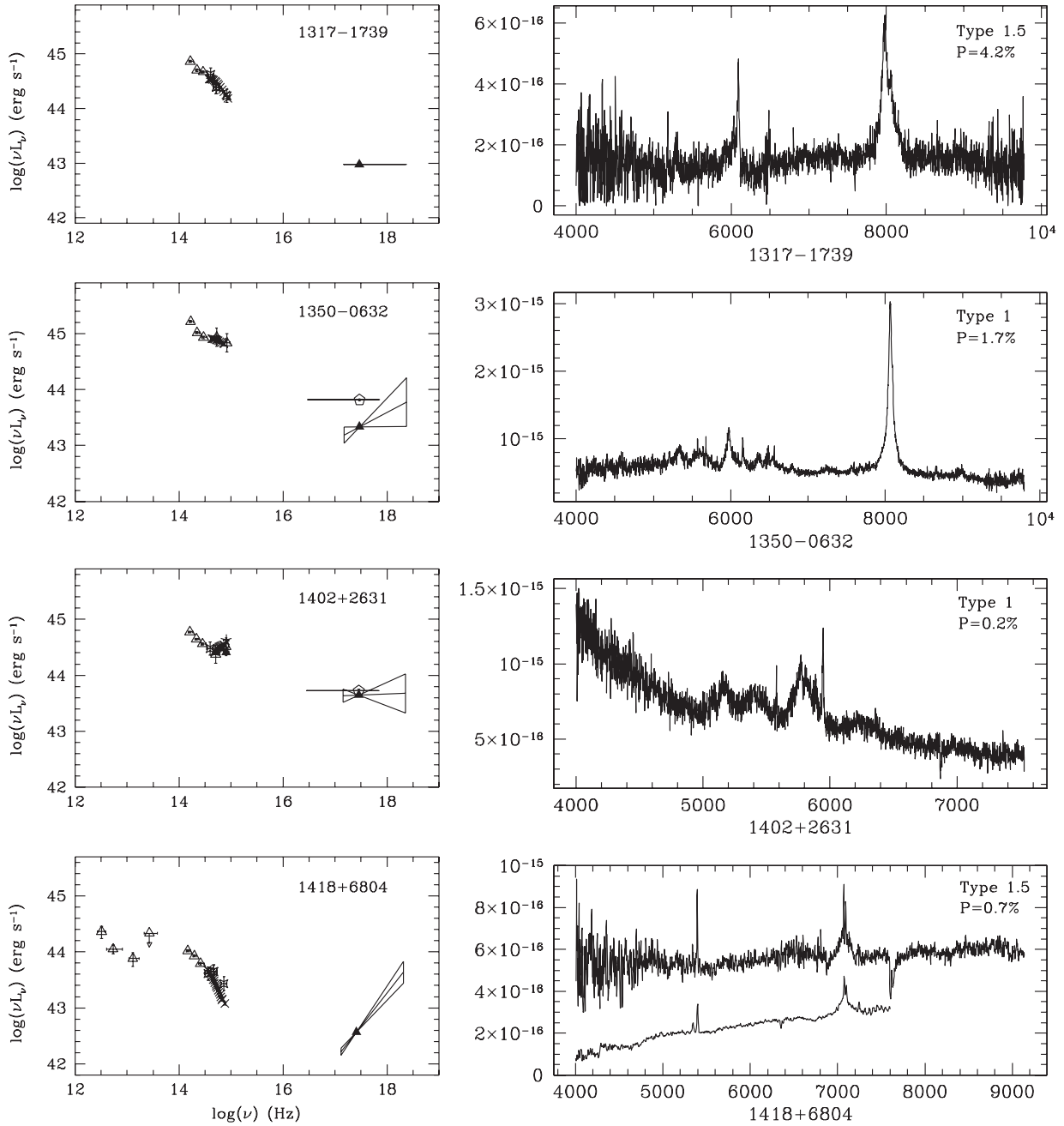
Figure 1. (Continued)

1. Optical colors of a highly reddened AGN are affected (bluened) by significant host galaxy emission (for $A_V \geqslant 2$ reddened AGN colors are redder than the host galaxy colors, see discussion in Section 5.2).

2. A significant scattered light component, as indicated by high polarization levels, bluens the optical colors.

3. Large amounts of hot circumnuclear dust are present, which does not obscure the optically emitting region, but does produce stronger NIR emission.

4. The intrinsic SEDs for the reddest $J - K_S$ objects have a much steeper/more pronounced intrinsic big blue bump (BBB) than the E94 median; applying the large A_V inferred from the $J - K_S$ colors would then produce bluer than expected $B - R$.

5. Dust composition/grain size differs from the Milky Way dust composition.

We will discuss points 1 and 2 in greater detail in Sections 5.2 and 5.3. The possibility of hot dust in few objects will be discussed in Section 8.1. For option 4, to produce the reddest $J - K_S$ objects ($J - K_S = 3.5$) from a standard E94 median AGN SED, an extinction of $A_V \sim 10$ mag is needed (if AGN is at $z = 0$). To obtain a reddened $B - R = 1.5$ mag color observed in these objects, we would need to start with a $B - R = -1$ mag, much bluer than the $B - R = -0.2$ mag expected from a pure standard accretion disk model, where $F_\nu \propto \nu^{1/3}$ (Shakura & Sunyaev 1973). This is also much bluer than the bluest observed colors of the optical/radio-selected QSOs from E94 (indicated by crosses in Figure 6) that extend to $B - R = 0.4$ mag, and the SDSS QSOs that
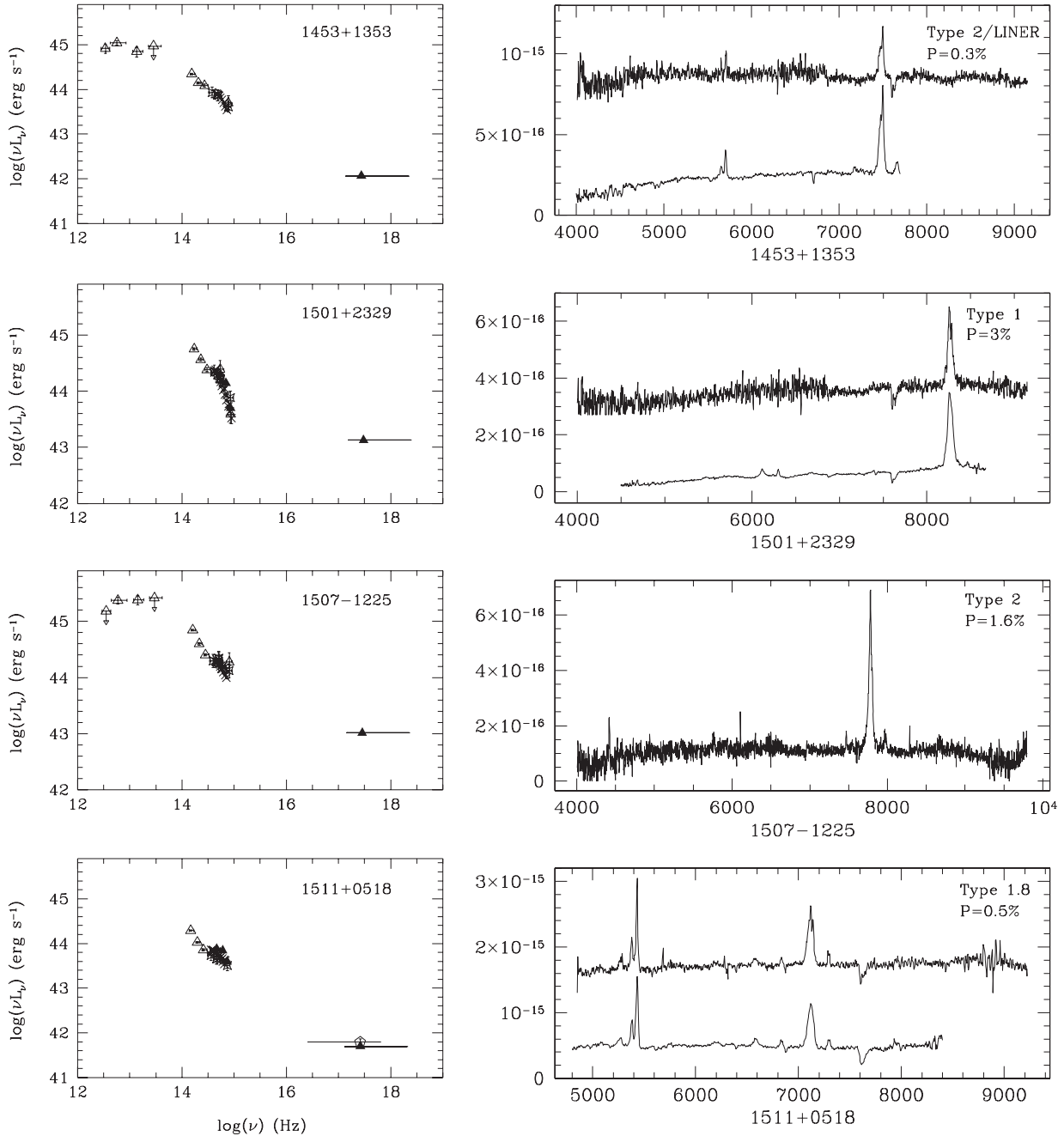
Figure 1. (Continued)

extend to the expected, from accretion disk modeling, limit of $B - R = -0.2$ mag. Therefore, we can rule out an extremely blue BBB.

Czerny et al. (1995) calculated extinction curves for different grain sizes and compositions including graphite, amorphous carbon, and a mixture of carbon and silicate grains. All extinction curves are very similar at optical wavelengths ($\lambda > 3000$ Å), but differ significantly in the UV, where the Milky Way and pure graphite dust show the lowest absorption in the UV. If the dust composition is different from Milky Way or pure graphite dust, or the grains are small, the dust will more easily absorb the UV, heat up and produce stronger NIR emission. Unfortunately, none of the reddest $J - K_S$ sources have UV (*HST* or *GALEX*) measurements, so option 5 is difficult to confirm/rule out.

5.2. Effects of Host Galaxy on the $B - R$ and $J - K_S$ Colors

Imaging of the 2MASS AGNs at *R* band shows that the observed, nuclear to host galaxy flux ratio is $10\times$ lower when compared with the ratio found in the normal/blue-selected AGNs (Hutchings et al. 2003). This suggests that the 2MASS AGNs have relatively weaker observed nuclear flux and/or higher host galaxy contribution at optical wavelengths than normal AGNs. We test that this is indeed the case. In Figure 7, we plot the effects of host galaxy on AGN optical/NIR colors by adding to Figure 6 curves showing the colors of a reddened AGN modified by the host galaxy emission. We use host galaxy template models (evolutionary stellar population synthesis models along the Hubble morphological sequence) from Buzzoni (2005) that take into account both the morphological type of the galaxy and
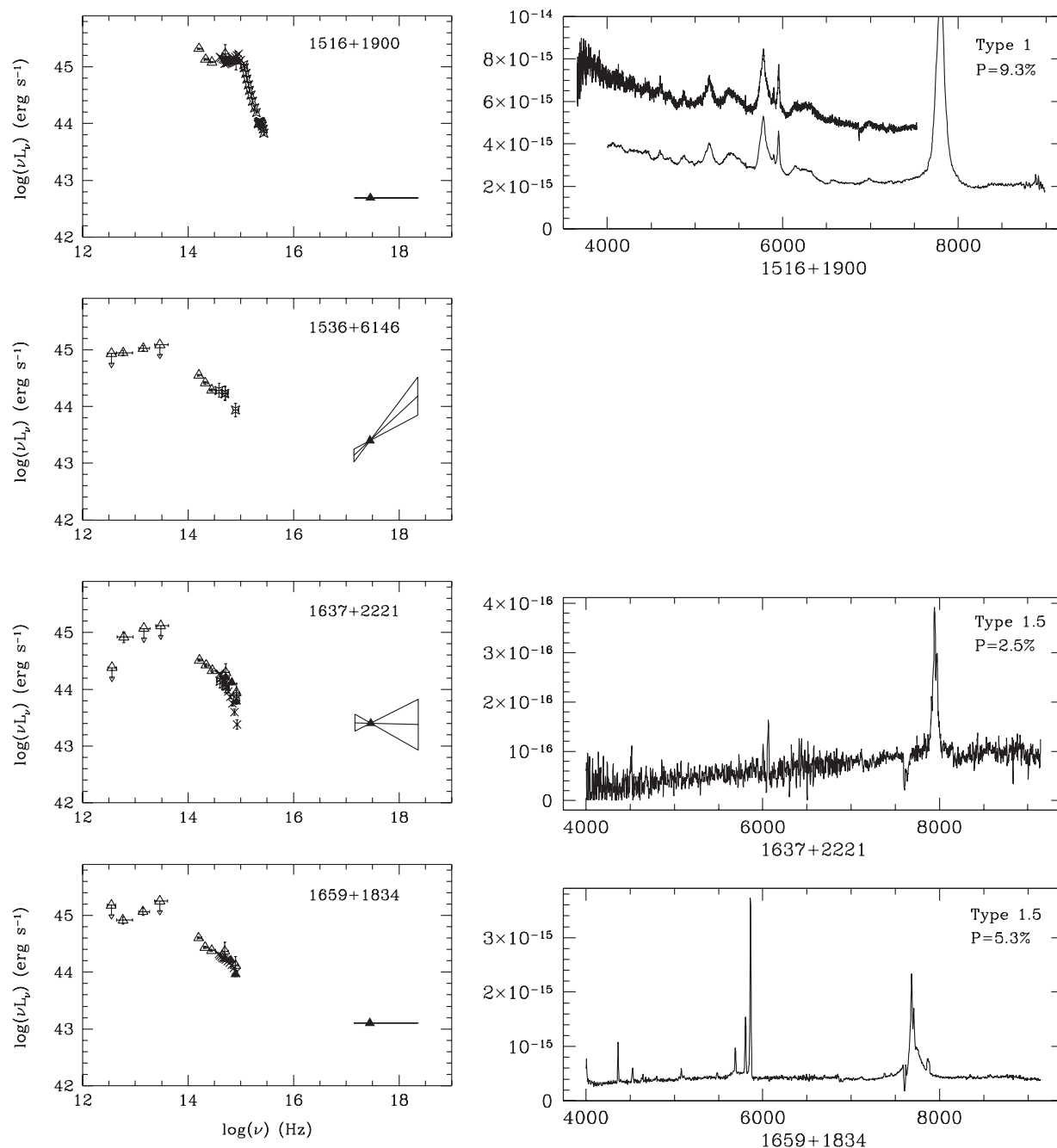
Figure 1. (Continued)

the age of the stars ranging from 1 to 15 Gyr. We select their reddest host in $B - R$, which is an elliptical galaxy with a 15 Gyr stellar population (E15) and the bluest host, being an Sd galaxy with a 5 Gyr stellar population (Sd05), and an intermediate color host: an Sa galaxy with a 5 Gyr stellar population (Sa05). These host galaxy templates were combined with a reddened AGN generated from the E94 median SED, using Milky Way dust with A_V ranging between 0 and 10 mag in steps of 1 mag. This demonstrates the range of possible colors. In each case a range of host galaxy strength relative to the intrinsic, *unreddened* AGN is shown, normalized in the R band to be 2, 5, 10, 20, 30, 40 times weaker than the AGN. For example, an Sd05 galaxy with five times brighter intrinsic (unreddened) AGN than host galaxy at R band is indicated by (Sd05;5). The same notation applies to the AGN + elliptical E15 (reddest possible) host galaxy models.

By comparing the colors of a pure reddened AGN (long-dash–short-dash line) with the colors of a reddened AGN+host galaxy in Figure 7, we see that the optical $B - R$ colors are strongly affected by host galaxy emission. For a high host galaxy contribution (e.g., (E15;2) and (Sd05;5)), the $B - R$ colors become bluer and more consistent with the host galaxy colors (represented by thick solid lines) at $A_V > 2$. For smaller host galaxy contribution ((E15;40), (Sa05;40), and (Sd05;40)), $B - R$ colors become dominated by host galaxy at $A_V > 4$. The $J - K_S$ colors, on the other hand, are much less dependent on reddening and host galaxy. They reach a peak at higher A_V whose value is dependent on the AGN/host galaxy ratio. AGNs with weaker host galaxies peak at redder $J - K_S$ color and higher A_V (compare for example curves (Sa05;40) and (Sd05,5) where the peak is at $A_V = 14$ and $A_V = 8$, respectively). The
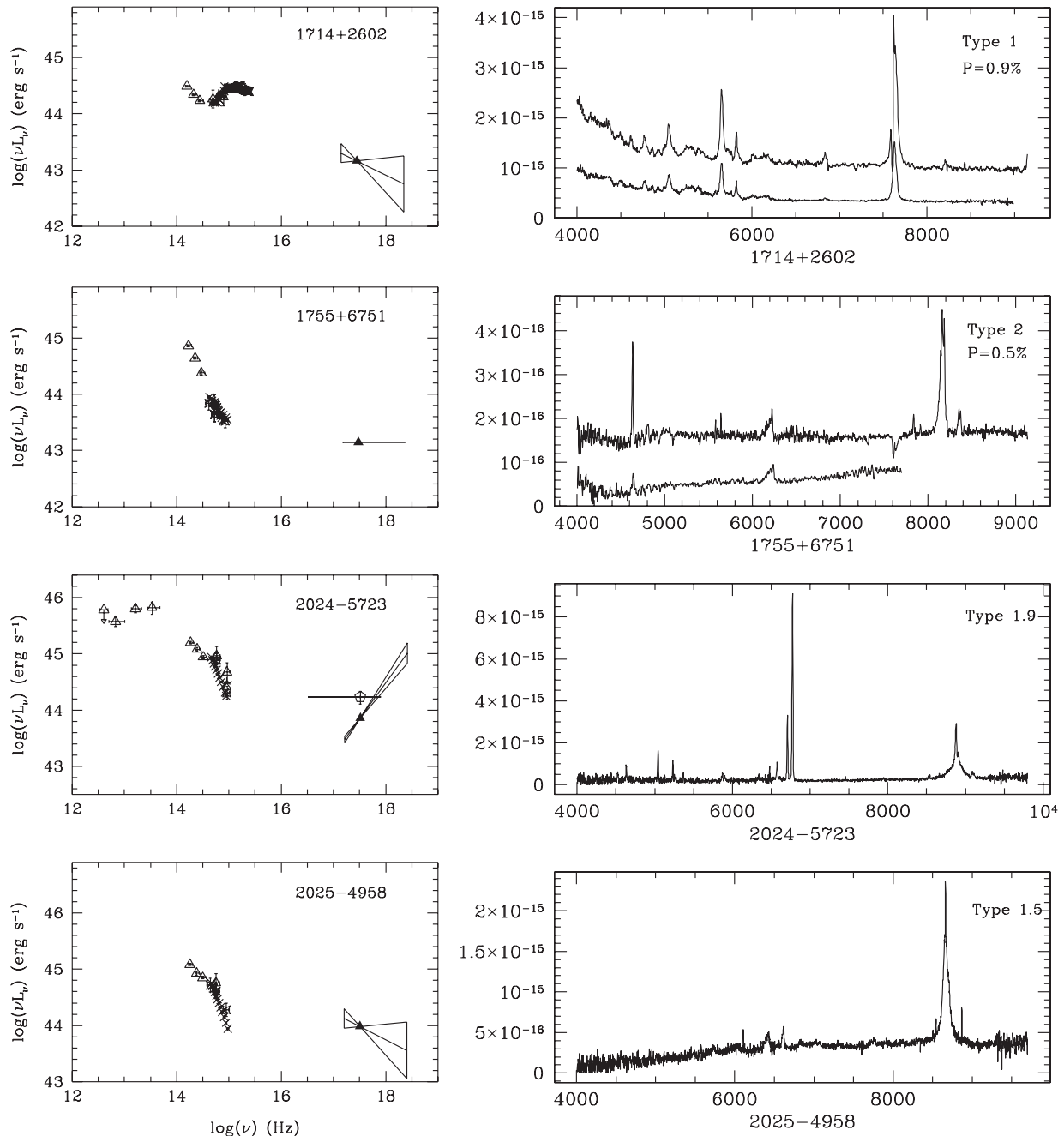
Figure 1. (Continued)

$J - K_S$ colors then plummet toward bluer colors with increasing A_V, reaching the host galaxy colors at $A_V \gg 20$.

The colors of the four reddest $J - K_S > 3$ sources can be modeled by a highly reddened AGN with $A_V = 11$–12 mag and a relatively weak host galaxy (e.g., (Sa05;40)). In this case the $B - R$ colors are consistent with the host galaxy colors, while the red $J - K_S$ colors are due to the reddened AGN.

To better understand the dependence of the $B - R$ and $J - K_S$ colors on AGN reddening and host galaxy contribution, we plot in Figure 8 a reddened AGN SED (E94 median AGN SED reddened by Milky Way dust—solid lines) and three (E15, Sd05 and Sa05) host galaxies from Buzzoni (2005) normalized to be five times (strong host galaxy contribution) and 40 times (weak host galaxy contribution) weaker at R band than the AGN

nucleus (dotted lines). The above conclusions from the color–color modeling are now clearer.

5.3. Effects of Scattered Light on the $B - R$ and $J - K_S$ Colors

Since many of the 2MASS sources are highly polarized, we investigate the effect of including AGN scattered light to our modeling. We use as the scatterer the average Milky Way dust, modeled by Draine (2003a) as a mixture of carbonaceous grains and amorphous silicate grains, with size distributions from the Weingartner & Draine (2001) case A model for $R_V = 3.1$, and renormalized according to Draine (2003a). The scattering cross section ($\sigma_{\rm sca}(\lambda)$) for such a mixture is obtained by multiplying the albedo (scattering cross section/extinction cross section) by the extinction cross section per H nucleon ($C_{\rm ext}/H$ in cm^2/H),
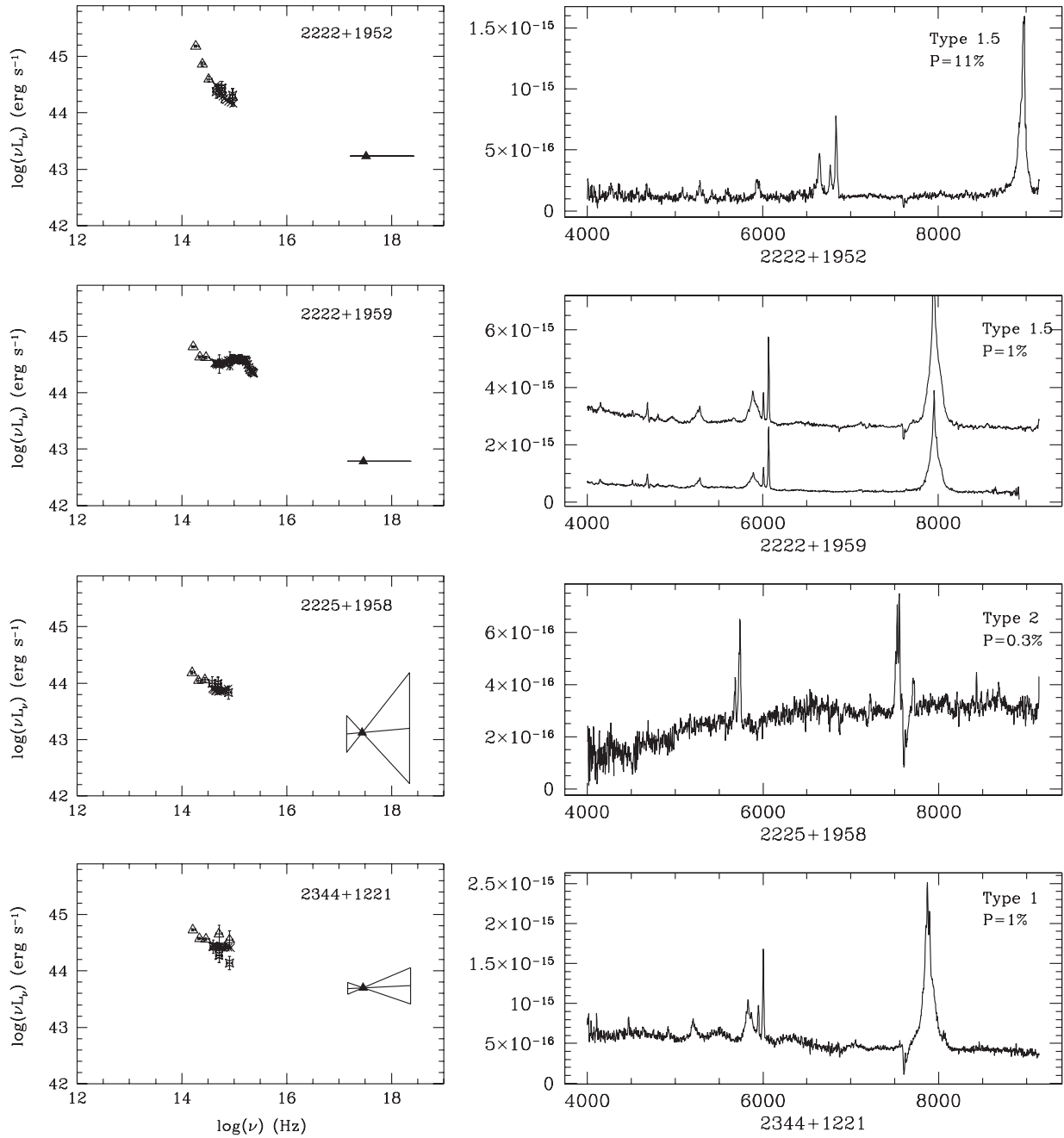
Figure 1. (Continued)

which depends on the wavelength of incident light (λ) and is presented by Draine (2003b):

$$\sigma_{\mathrm{sca}}(\lambda) = \mathrm{albedo}(\lambda) * C_{\mathrm{ext}}/H(\lambda). \qquad (1)$$

The amount of scattered light is then estimated at B, R, J, K effective wavelengths by multiplying the scattering cross section σ_{sca}, phase function $\phi_0(\theta)$, and scattering dust+gas column N_{H}. The function $\phi_0(\theta)$ is the Henyey & Greenstein phase function from Draine (2003a, Equation (4)):

$$\phi_0 = \frac{1}{4\pi} \frac{1 - g^2}{(1 + g^2 - 2g\cos\theta)^{3/2}}, \qquad (2)$$

where $g = \langle\cos\theta\rangle$ is a function of λ and its values are also taken from Draine (2003b). For simplicity, we use a scattering angle

$\theta = 90°$. We do not assume any particular value for N_{H}, but indirectly obtain it when normalizing the amount of scattered AGN light to the total (AGN + scattered + host galaxy) light at R band to be consistent with the observed value.

In Figure 9, we present the effect of adding scattered intrinsic (unreddened) AGN light (E94 median SED) to a reddened AGN nucleus (E94 median SED reddened by Milky Way dust), on the $B - R$ and $J - K_S$ colors. Similar to the effect of host galaxy emission, the addition of scattered AGN light changes primarily the optical $B - R$ colors, which become much bluer than the pure reddened AGN colors (long-dash–short-dash line) once the direct AGN light is absorbed away ($A_V \gtrsim 2$–4 mag depending on the scattered light contribution; see also Zakamska et al. 2006). $J - K_S$ colors are affected at higher ($P \gg 7\%$) scattered light contribution and higher A_V (see also Figure 8 which shows this from the SED point of view). Comparison of curves that include

Figure 2. Optical Spectropolarimetry for $2MASSJ04203206 - 2047592$, $2MASSJ09384445+0057156$, $2MASSJ13170436 - 1739126$, $2MASSJ13503735 - 0632153$, and $2MASSJ15362773+6146417$. The panels show from top to bottom the position angle of polarization (θ), the percentage polarization (q'), the polarized flux density ($q' \times F_\lambda$), and total flux density (F_λ).
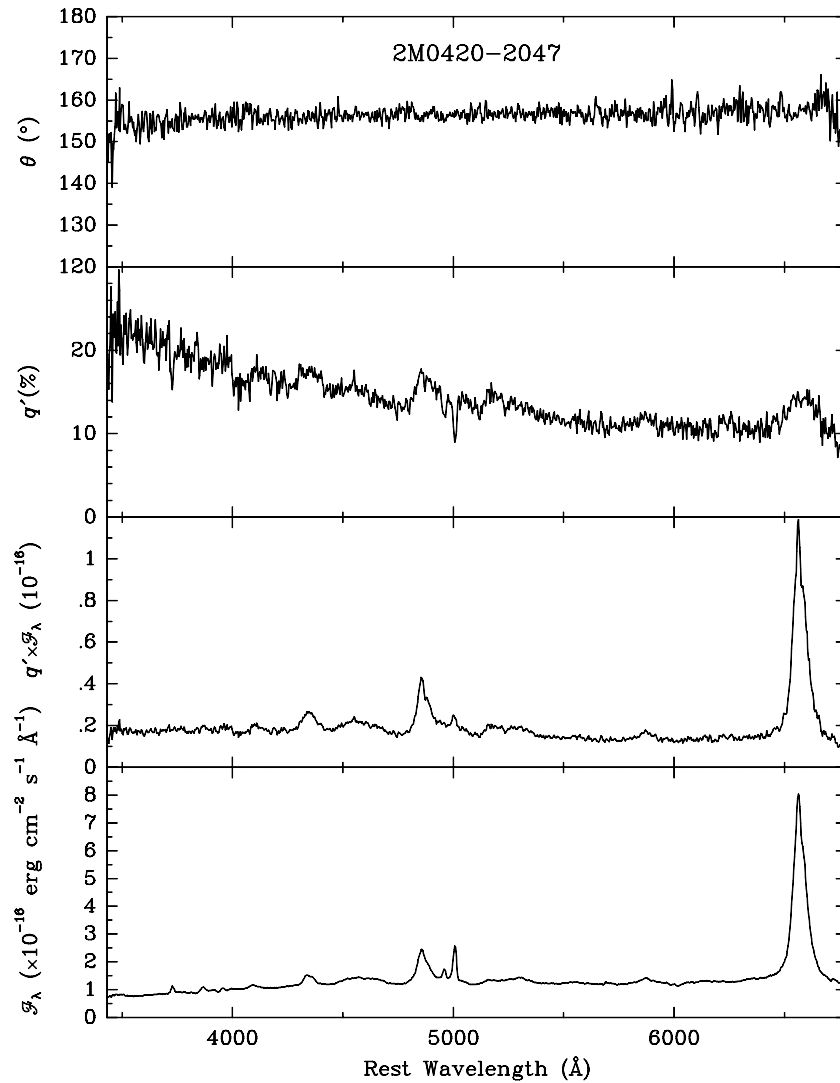
scattering off dust and electrons shows that dust scattering, as expected, gives bluer $B - R$ and slightly redder $J - K_S$ colors than scattering off electrons.

5.4. The Combined Effects of Scattered Light and Host Galaxy Contributions

In Figure 10, we present the effects of both host galaxy and polarization on the colors of a reddened AGN (thick curves) and compare them with the colors of a pure reddened AGN (long-dash–short-dash line). The optical and IR colors both become bluer relative to the pure reddened AGN light as scattered light and host galaxy contribution is increased, although the effects on the $J - K_S$ colors are weaker, especially for smaller scattered light and host galaxy contributions. The optical/IR colors are also bluer when compared to the colors of a reddened AGN+host galaxy (dotted curves).

5.5. Colors and Redshift

5.5.1. Redshift Dependence of Pure AGN Color

An AGN's observed optical/NIR continuum colors change significantly with redshift. In this section, we calculate the

$J - K$, $B - K$, and $B - R$ colors of a pure median AGN SED from E94 (blue AGN sample with host galaxy subtracted; the emission lines are *not* explicitly included as discrete features[11]) as a function of redshift and present them in Figures 11(a)–(c) (see Maddox & Hewett 2006 for simulations of redshift dependence of other colors measured between passbands used by the SDSS and 2MASS). In all figures, the bottom (bluest) curve (thick line) is plotted for the unreddened E94 median SED (see Table 8 for the approximate linear fits of this dependence). Above this curve the colors of the reddened AGN are plotted, where Milky Way dust extinction law from Savage & Mathis (1979) was used, with the 2200 Å feature removed, since it is not observed in AGN. The dependence of the 2MASS median SED on redshift (dotted line) shows optical/NIR colors that have values in between the E94 SED reddened by $A_V = 1$ and by $A_V = 2$.

For the unreddened E94 SED, the $J - K$ color becomes bluer with redshift due to the optical blue bump moving into the NIR spectral region, which is one of the reasons for the predominance

---

[11] However note that the individual SEDs used to calculate the E94 median SED had the emission lines included in their broadband bins.
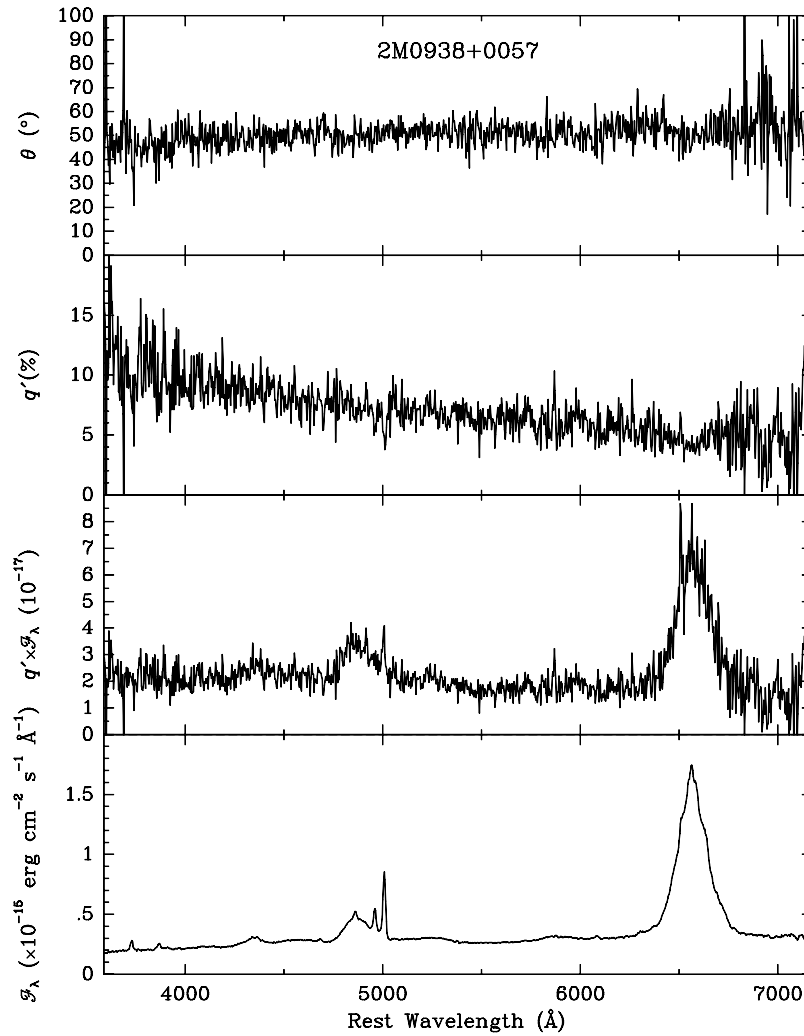
Figure 2. (Continued)

of low-redshift QSOs in the 2MASS sample (Cutri et al. 2002; see also Barkhouse & Hall 2001). In comparison, the behavior of the $J - K$ color for the 2MASS median (dotted curve) is different due to the shape of the 2MASS SED which lacks the BBB (see Figure 3). Due to the recovery of the red $J - K$ color at $z \sim 2$, objects with SEDs similar to the red 2MASS AGN SEDs at $z > 2$ should be picked up by deep NIR surveys by virtue of their red $J - K_S > 2$ color.

In Figures 11(b) and (c), where the $B - K$ and $B - R$ dependence on redshift is shown, the unreddened E94 median at low redshifts also becomes bluer due to the blue bump moving toward longer wavelengths. As A_V increases from 1 to 10 mag, the $J - K$, $B - K$, and $B - R$ colors become redder. As the redshift increases, the colors also become redder, since the BBB becomes redder at shorter wavelengths due to increasing extinction. A strong increase in Galactic dust extinction (used in our models without the 2200 Å feature) at $\lambda > 1500$ Å($\log \nu = 15.3$) explains the strong rise to redder $B - K$ and $B - R$ colors at $z > 2$.

5.5.2. Redshift Dependence of AGN + Host Galaxy + Scattered Light Color

The redshift range of the red 2MASS AGN sample is small, but we have shown that the colors change significantly even over a small range. We therefore investigate the effects of redshift on our color–color analysis.

Buzzoni (2005) presents fluxes and colors of the host galaxy templates in the Johnson $UBVRIJHK$ filters. Since the templates are not smooth, we avoid interpolating between filters by calculating the colors of an AGN+host galaxy redshifted to $z = 0.31$ (which is also the approximate highest redshift of the 2MASS sample), for which the fluxes in the U, V, I, H bands at the rest frame transform to the fluxes in B, R, J, K bands in the observed frame. We present this in Figure 12(a) and, for comparison, we plot the observed colors of a pure reddened AGN at $z = 0$. In comparison with the $z = 0$ models, the redshifted $z = 0.31$ reddened AGN+host galaxy models have less host galaxy (and more AGN) contribution at the observed B and R bands and so extend to redder $B - R$ colors, closer to the original, pure reddened AGN colors. The contribution of host galaxy at observed J and K bands is slightly larger for AGN at $z = 0.31$ than at $z = 0$, hence the AGN+host galaxy curves peak at slightly bluer $J - K_S$ color than the $z = 0$ curves.

In Figure 12(b), we compare the colors of a reddened AGN + intrinsic AGN light scattered off dust models from Section 5.3 at two different redshifts: $z = 0$ (dotted lines) and $z = 0.31$ (solid lines). The observed $B - R$ and $J - K_S$ colors at $z = 0.31$ become bluer (closer to the scattered intrinsic AGN light colors) when compared to the $z = 0$ models, as the dust scattering efficiency increases with decreasing wavelength (a $\propto \lambda^{-2}$ Reyleigh scattering dependence is assumed).
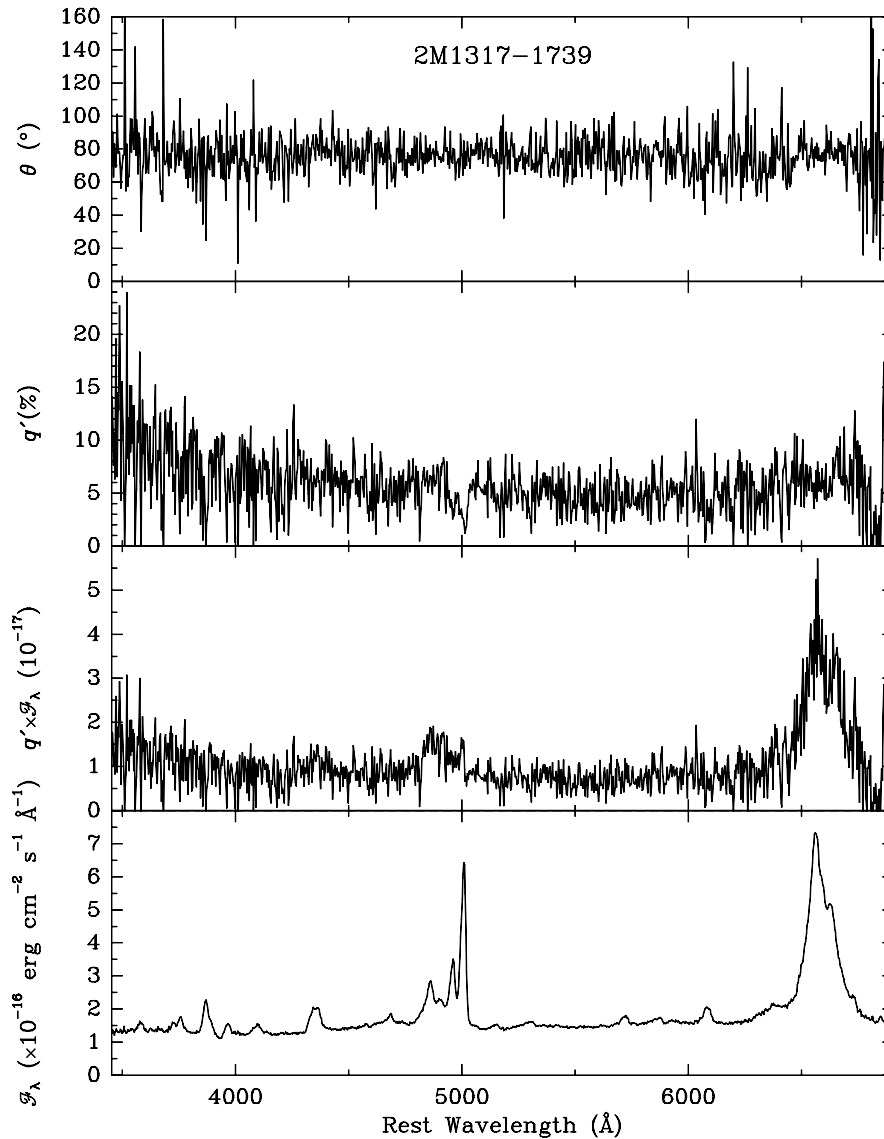
Figure 2. (Continued)

When both host galaxy emission and scattered AGN light are added to the reddened AGN (Figure 13) the $z = 0.31$ models reach redder $B - R$ colors than the $z = 0$ only if the host galaxy contribution is high (e.g., compare (E15;5;1%;z) and (E15;5;1%) curves). The $z = 0.31$ models also peak at bluer $J - K_S$ colors, when compared to the models where the contribution of host galaxy is low (compare (Sd05;20;1%;z) and (Sd05;20;1%)).

5.6. Estimates of the 2MASS AGN Parameters from Optical/IR Colors

In Table 7, Columns 8–13 present model parameters of the 2MASS AGN that were obtained from the $B - R$ and $J - K_S$ color modeling described in Sections 5.2–5.5.2. These are the AGN A_V (Column 8), host galaxy type and intrinsic AGN/host galaxy ratio at R band (Column 9), and amount of scattered light relative to the intrinsic and the reddened AGN (Columns 10 and 11). Since redshift affects the colors significantly over our redshift range we use the higher-redshift models (Sections 5.5.1 and 5.5.2) to interpret the sources with $z \geqslant 0.3$ (these are marked in Column 12). If more than one model fit

the optical/IR colors, we chose the reddening value closest to the X-ray-fitted N_H (Column 6). If N_H was not available we looked at the optical type (Table 1 and Figure 1) and chose lower reddening values for Types 1–1.5 and higher for Types 1.8–2.0. Our modeling results were compared with Marble et al. (2003), who studied the *HST*/WFPC2 *I*-band images of the 2MASS AGN and present the AGN-to-total light ratio and host galaxy type in which the AGN resides. Fifteen out of 16 objects in common had an AGN-to-total light ratio and host galaxy Hubble type consistent with Marble et al. (2003). We also compare our modeling results with the host galaxy to total light ratios obtained from stellar absorption features by Smith et al. (2003). Our sample includes 11 sources in common, all having consistent ratios.

Our modeling brakes down for one highly polarized ($P = 11\%$), high-z object 2222+1952, where our optical/IR modeling gives a 54% observed AGN, 34% host galaxy, and a 12% scattered light contribution to total light at R band, while Marble et al. (2003) quote 99% AGN emission with no host galaxy contribution at $\sim$8100 Å. Our X-ray fitting gives low values of N_H consistent with the Marble et al. (2003) results, but our modeling requires higher reddening to reproduce the red $J - K_S$
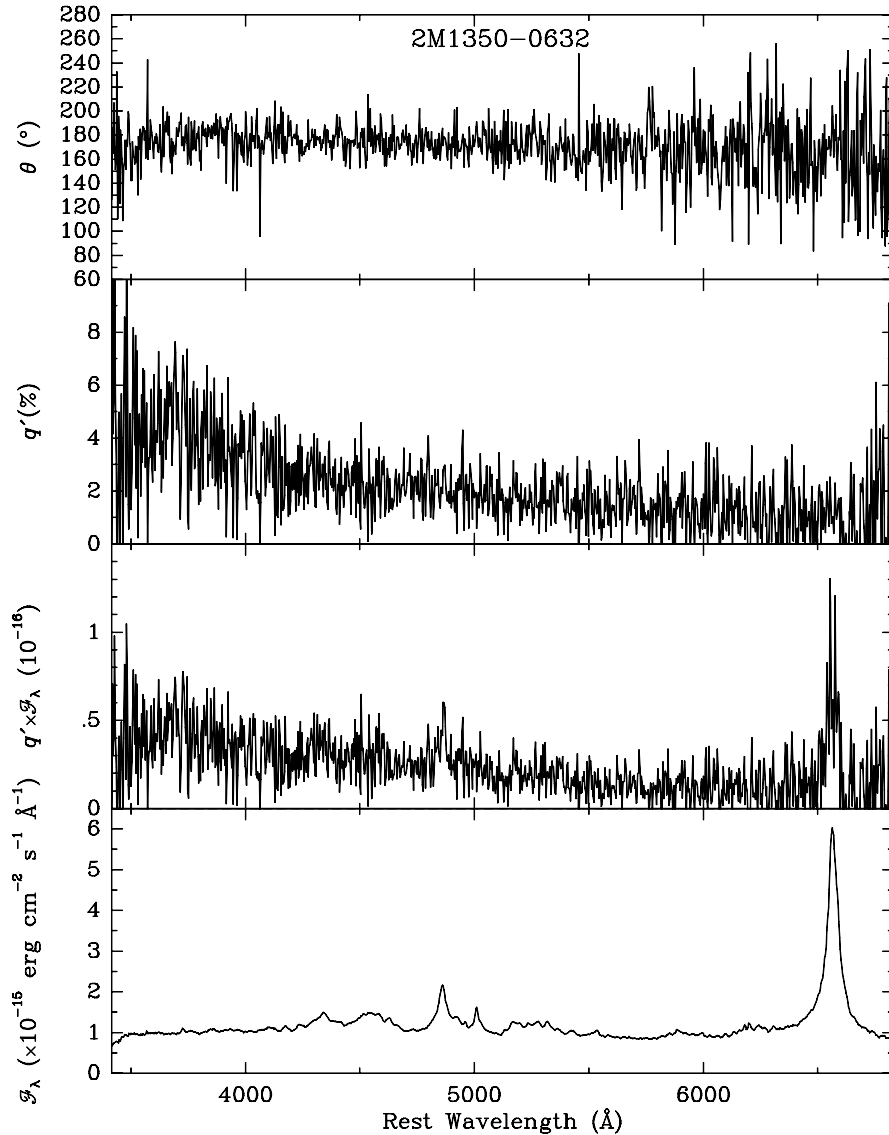
Figure 2. (Continued)

= 3.05 mag color. In this object the red $J - K_S$ color is most likely due to very hot dust lying close to the nucleus, and not due to the reddening of the nucleus, predicted by the model.

6. X-RAY PROPERTIES

We will now concentrate on the X-ray properties of the red 2MASS AGNs and compare them with the optical/radio-selected AGNs from E94. In Figure 14, we present the relations between the ratio of intrinsic X-ray flux at 1 keV (corrected for Galactic and intrinsic extinction) to the observed optical flux in B band ($F(1 \text{ keV})/F_B$) and the ratios of intrinsic 1 keV flux to the observed fluxes measured at R and K bands ($F(1 \text{ keV})/F_{R,K}$). The $F_{B,R,K}$ fluxes are corrected for Galactic dust absorption only. Intrinsic $F_{B,R,K}$ fluxes are difficult to obtain since (1) the host galaxy contribution at optical/NIR wavelengths is nonnegligible (see Section 5), (2) the reddening and host galaxy contribution estimated from the $B - R$ and $J - K_S$ colors (Section 5; Table 7) are crude, and (3) estimates of dust reddening from the measured X-ray absorption are not useful since optical dust and X-ray gas column densities are frequently observed to disagree in quasars by up to 3 orders

of magnitude (Maiolino et al. 2001). The 2MASS sources in Figure 14 cover the range of the unreddened E94 sources and extend to 10–100× lower $F_X/F_{B,R,K}$ ratios.

In Figure 14(b) (F_X/F_B vs. F_X/F_K relation) one can roughly estimate the amount of dust reddening at optical wavelengths in the 2MASS sample, relative to the unreddened E94 sample. Since dust absorption is high at B and low at K band, the F_X/F_B changes strongly with reddening while the F_X/F_K does not. The 2MASS sample shows a shift/scatter toward larger F_X/F_B values relative to the E94 sample, implying a range in reddening of $E(B - V) \sim 0.86$ ($N_H = 5 \times 10^{21} \text{ cm}^{-2}$ assuming a standard Milky Way dust-to-gas ratio), as shown by the arrow. This is a lower limit as some of the reddest sources have a nonnegligible contribution from the host galaxy (as shown in Section 5), which decreases the effect of reddening on the optical/IR colors.

Since reddening by dust moves objects toward higher $F_X/F_{B,R,J,K}$ values in these figures, the 2MASS sources with $F_X/F_{B,R,J,K}$ ratios lower than E94 must be either intrinsically weaker or more obscured in X-rays (a 10× lower 1 keV flux is obtained by obscuring the intrinsic continuum with gas column of $N_H = 10^{22} \text{ cm}^{-2}$). The sources with the lowest $F_X/F_{B,R,J,K}$
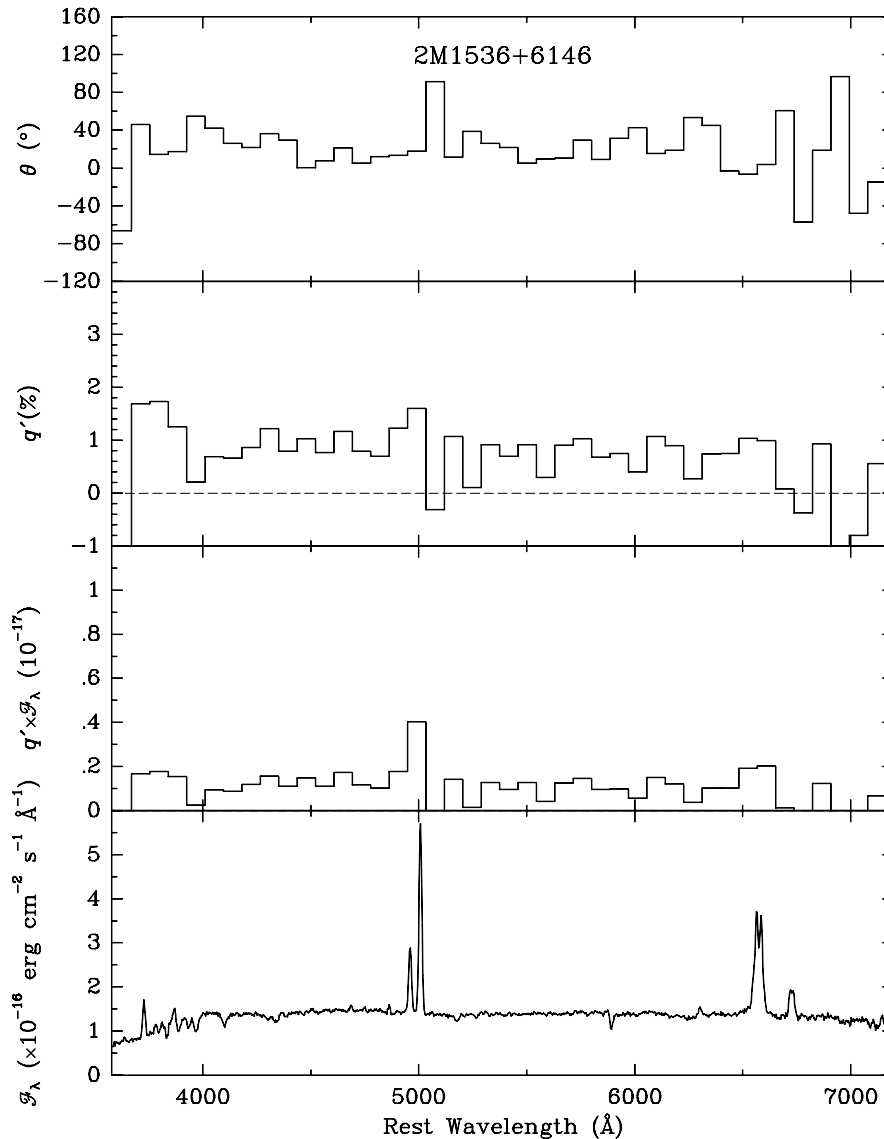
Figure 2. (Continued)

are mainly the lowest signal-to-noise ratio (S/N; A) *Chandra* sources, where an average $N_H = 7.6 \times 10^{21}$ cm^{-2} value was assumed (see Section 3.1). Their properties will be discussed in the following section.

6.1. [O III] Versus Hard-X-Ray Relation

The luminosity of the [O III] $\lambda5007$ emission line ($L_{[O\,III]}$), originating from the narrow-line region (NLR), has long been suggested to be an indicator of the intrinsic nuclear luminosity of the AGN due to the similarity of the [O III]-to-hard-X-ray flux ratio between Seyfert 1 and Seyfert 2 galaxies (Mulchaey et al. 1994; Alonso-Herrero et al. 1997; Turner et al. 1997). This, in turn, can be used as a test for a Compton-thick AGN (Ptak et al. 2003), in which the X-rays are so heavily absorbed that the observed emission is dominated by scattered light that appears unabsorbed, but unusually weak in comparison with $L_{[O\,III]}$. More recently, Maiolino et al. (1998) and Bassani et al. (1999) suggest that an extinction-corrected $L_{[O\,III]}$ is more appropriate, though the uncertainties in such extinction corrections in AGNs are generally large. In Figure 15, we present the relation between the *Chandra* 2–10 keV X-ray flux and the narrow emission-line [O III] $\lambda5007$ flux. Seyfert 1s and Seyfert 2s from

Mulchaey et al. (1994) sample have [O III] fluxes uncorrected for extinction, and the intrinsic hard X-ray (2–10 keV) fluxes estimated from the EXOSAT and Ginga spectra by fitting a power law with Galactic and intrinsic absorption. Most objects in the Mulchaey et al. (1994) sample cluster around a line that represents the log $F([O\,III])/F(2$–10 keV) mean of -1.89 ± 0.25 (1σ uncertainty) for Seyfert 1s and Compton-thin Seyfert 2s. However NGC 1068, a Seyfert 2, shows an exceptionally strong [O III] to hard-X-ray flux ratio, that is interpreted as being due to obscuration of the direct X-ray light by Compton-thick ($N_H \geqslant 10^{24}$ cm^{-2}) material (Turner et al. 1997; Antonucci & Miller 1985) so that scattered light dominates the X-ray emission.

We identify the 2MASS objects in Figure 15 according to the quality of their *Chandra* spectra. We show two versions of the figure: Figure 15(a) uses the observed [O III] flux with no extinction correction applied and Figure 15(b) shows the [O III] fluxes corrected for reddening estimated from the ratio of the narrow Hβ to Hα lines, assuming an unreddened (case B) value of 3. Emission from Fe II and [N II] lines was subtracted for the measurements of Hβ and Hα, respectively. We circled objects in Figure 15(b) that have undetermined reddening corrections
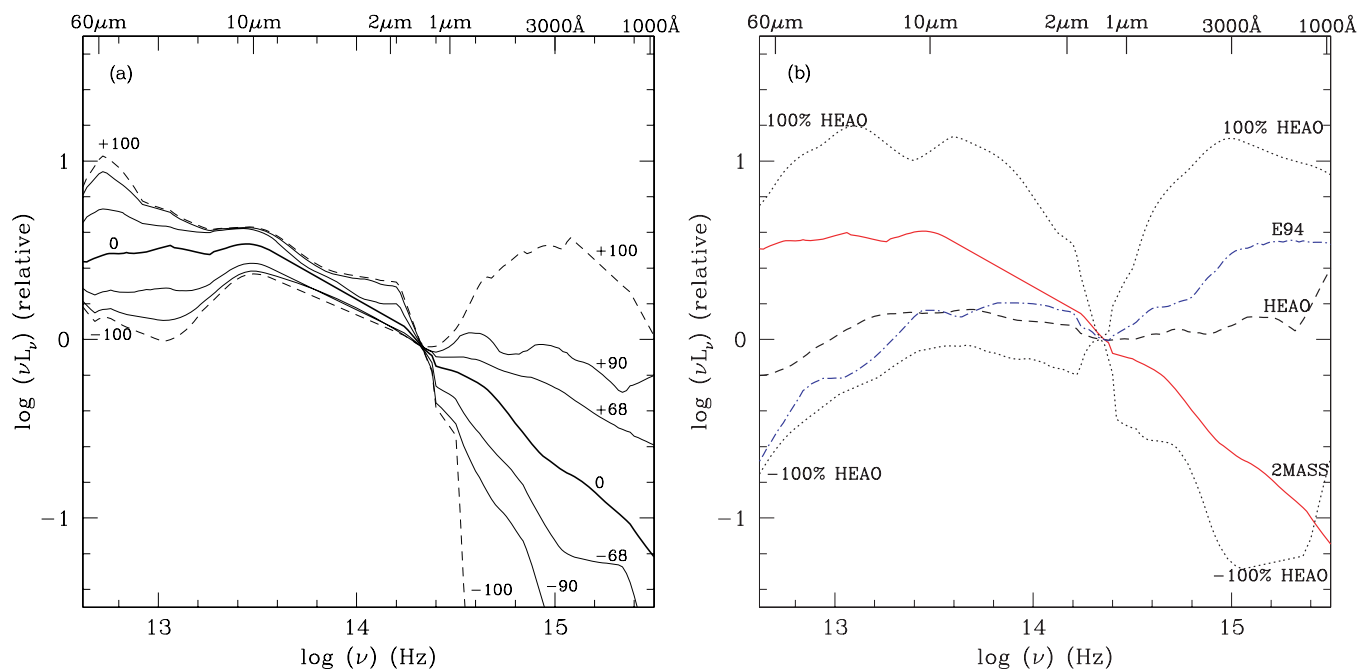
Figure 3. (a) Median spectral energy distributions for the red 2MASS AGN sample normalized at 1.5 μm along with the 68, 90, and 100 (dashed line) Kaplan–Meier percentile envelopes. (b) Comparison between medians normalized at 1.5 μm of the red 2MASS AGN sample (solid line), hard-X-ray-selected *HEAO* AGN sample from Kuraszkiewicz et al. (2003; dashed line), and optical/radio-selected Einstein QSO sample from Elvis et al. (1994; dot-dashed line). The dotted lines show the Kaplan–Meier 100 percentile envelopes for the *HEAO* sample.

(A color version of this figure is available in the online journal.)

Figure 4. Histograms of the optical, UV, and IR luminosity ratios. The shaded area: current 2MASS AGN sample; thick solid line: the hard-X-ray-selected *HEAO* AGN sample of Kuraszkiewicz et al. (2003); and the dashed line: the optical/radio-selected Einstein QSO sample from Elvis et al. (1994). Objects with *HST* spectra are marked by "x" and objects with high polarization ($P > 3\%$) with "p."

Table 7
Summary of the Data Sources for the SEDs and Parameters Used in Optical/IR Color Modeling

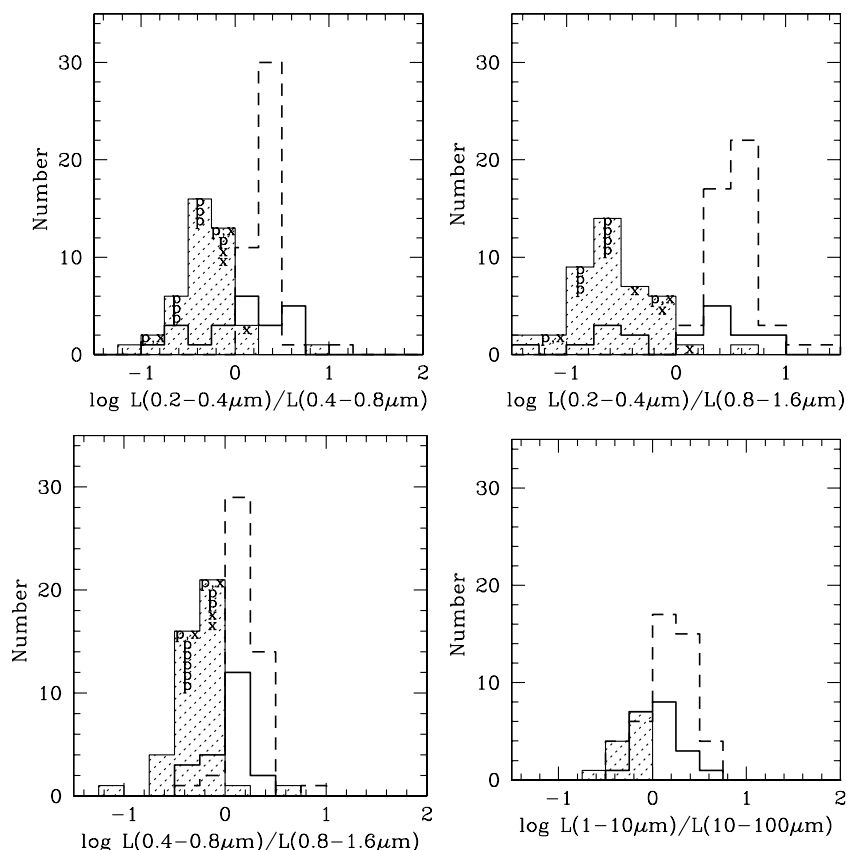| Name	IR	Optical	UV	X-ray	N_H $(10^{22}$ cm$^{-2})$	$A_V(N_H)$ (mag)	A_V^{mod} (mag)	Host Galaxy	P_{mod} (%)	P_{obs} (%)	High z?	Host (%)
(1)	(2)	(3)	(4)	(5)	(6)	(7)	(8)	(9)	(10)	(11)	(12)	(13)
0007+1554	2	5, 6		C	1.22 ± 0.15	7.60 ± 0.92	3	(Sd05,5)	. . .	. . .	. . .	61
0050+2933	2	5, 6		C	1.12 ± 0.66	6.96 ± 4.07	4	(Sd05,5)	. . .	. . .	. . .	76
0108+2148	2	5, 6		A	. . .	. . .	5	(Sd05,20)	0.5	6	y	58
0157+1712	2	5, 6		B	2.83 ± 1.40	17.60 ± 8.70	7	(Sa05,20)	. . .	. . .	. . .	86
0221+1327	1, 2	5, 6		C	1.66 ± 0.58	10.29 ± 3.60	4–5	(E15,10)	. . .	. . .	. . .	62–76
0234+2438	2	5, 6		A	. . .	. . .	1	Pure AGN	. . .	. . .	. . .	0
0348+1255	2	5, 6		A	. . .	. . .	11	(Sa05,40)	. . .	. . .	. . .	98
0409+0758	2	5, 6		C	0.33 ± 0.13	2.04 ± 0.79	1	Pure AGN	. . .	. . .	. . .	0
0420−2047	2	3, 5, 6		B	4.01 ± 1.51	24.91 ± 9.38	5	(E15,20)	1.2	13	. . .	53
0748+6947	1, 2	5, 6		A	. . .	. . .	10	(Sa05,40)	. . .	. . .	. . .	96
0918+2117	1, 2	5, 6	7	C	0.22 ± 0.21	1.39 ± 1.28[a]	3	(Sa05,20)	1.2	6.5	. . .	27
0938+0057	2	5, 6		C	0.76 ± 0.62	4.73 ± 3.82	5	(Sa05,40)	0.6	7	. . .	57
0955+1705	2	5, 6	7	A	. . .	. . .	1	(Sd05,10)	. . .	. . .	. . .	17
1021+6311	2	5, 6		C	2.37 ± 0.55	14.72 ± 3.39	22	(Sa05,20)	. . .	. . .	. . .	100
1027+1219	2	5, 6		B	4.34 ± 2.57	26.98 ± 15.95	15	(Sa05,5)	. . .	. . .	. . .	100
1040+5934	1, 2	5, 6		A	. . .	. . .	10	(Sa05,20)	. . .	. . .	. . .	98
1049+5837[b]	2	6		C	4.22 ± 4.18	26.21 ± 25.95	. . .	. . .	. . .	. . .	. . .	. . .
1051+3539	2	5, 6		C	0.56 ± 0.14	3.48 ± 0.89	3	(Sd05,5)	. . .	. . .	. . .	61
1127+2432[b]	2	4, 6		A	. . .	. . .	. . .	. . .	. . .	. . .	. . .	. . .
1230+0302	2	5, 6		C	0.33 ± 0.10	2.08 ± 0.61	1–2	Pure AGN	. . .	. . .	. . .	0
1243−0802	2	5, 6		C	0.78 ± 0.43	4.84 ± 2.67	4	(Sd05,10)	. . .	. . .	. . .	61
1258+2329	2	4, 5, 6		A	. . .	. . .	0	Pure AGN	. . .	. . .	. . .	0
1300+1632	2	4, 5, 6		C	1.79 ± 1.08	11.09 ± 6.68	10	(E15,5)	. . .	. . .	. . .	96
1307+2338	1, 2	5, 6		A	. . .	. . .	11	(Sa05,>40)	. . .	. . .	. . .	98
1317−1739	2	5, 6		A	. . .	. . .	2	(Sa05,40)	1.5	5	. . .	13
1350−0632	2	5, 6		C, 8	0.02 ± 0.16	0.14 ± 1.00	1	Pure AGN	. . .	. . .	. . .	0
1402+2631	2	4, 5, 6		C, 8	0.01 ± 0.11	0.09 ± 0.71	0	Pure AGN	. . .	. . .	. . .	0
1418+6804	1, 2	5, 6		C	0.73 ± 0.22	4.54 ± 1.34	4	(Sd05,10)	. . .	. . .	. . .	61
1453+1353	1, 2	5, 6		A	. . .	. . .	14	(Sd05,10)	. . .	. . .	. . .	100
1501+2329	2	5, 6		B	0.56 ± 0.31	3.46 ± 1.94	3	(Sd05,20)	. . .	. . .	. . .	29
1507−1225	1, 2	5, 6		B	2.67 ± 1.11	16.61 ± 6.88	20	(E05,20)	. . .	. . .	. . .	100
1511+0518	2	4, 5, 6		B, 8	0.03 ± 0.00	0.21 ± 0.00	6	(Sd05,20)	. . .	. . .	. . .	76
1516+1900	2	5, 6	7	A	. . .	. . .	3	(Sa05,20)	2	10	. . .	26
1536+6146	1, 2	4, 5, 6		C	2.27 ± 0.61	14.12 ± 3.82	18	(E15,10)	. . .	. . .	. . .	100
1637+2221	1, 2	5, 6		C	0.83 ± 0.32	5.16 ± 1.98	2–3	(Sa05,5)	. . .	. . .	. . .	44–61
1659+1834	1, 2	6		A	. . .	. . .	3	(E15,10)	1.2	5	. . .	42
1714+2602	2	6	7	C	0.14 ± 0.17	0.89 ± 1.03	0–1	Pure AGN	. . .	. . .	. . .	0
1755+6751	2	5, 6		B	2.87 ± 1.25	17.81 ± 7.74	22	(Sa05,20)	. . .	. . .	. . .	100
2024−5723	1, 2	4, 5, 6		C, 8	0.33 ± 0.13	2.06 ± 0.83	3	(E15,20)	. . .	. . .	y	29
2025−4958	2	5, 6		C	0.71 ± 0.24	4.42 ± 1.47	4–5	(Sd05,4)	. . .	. . .	y	80–89
2222+1952	2	5, 6		B	0.05 ± 0.22	0.29 ± 1.36	10	(Sd05,50)	0.7	12	y	34
2222+1959	2	4, 5, 6	7	A	. . .	. . .	0–1	(E15,30)	. . .	. . .	. . .	6
2225+1958	2	5, 6		C	3.07 ± 2.06	19.04 ± 12.78	17	(Sa05,5)	. . .	. . .	. . .	100
2344+1221	2	5, 6		C	0.40 ± 0.18	2.50 ± 1.09	1	(E15,10)	. . .	. . .	. . .	17

Notes. Column 1: object name; Columns 2–5 show data sources used for the SEDs: 1, The *IRAS* Faint Source Catalog, Moshir et al. (1990); 2, 2MASS database photometry; 3, Maddox et al. (1990); 4, *B* magnitude from NED; 5, SuperCOSMOS photometry; 6, USNO-A2 photometry; 7, *HST*/STIS archive; 8, WGA Catalog; Column 5 also shows information on whether the *Chandra* spectrum had high (A), medium (B), or low (C) signal to noise; Column 6 gives column density obtained from *Chandra* spectral fitting; Column 7 reddening obtained from Column 6 using the following conversion: $N_H = A_V * 1.61 \times 10^{21}$ cm^{-2}, which assumes the Galactic gas-to-dust ratio; Columns 8–13 give AGN parameters obtained from the optical/IR color modeling described in Section 5 where (8) AGN reddening; (9) type of host galaxy and intrinsic AGN/host galaxy ratio (e.g., (Sd05,5) denotes an Sd host galaxy with 5 Gyr stars, and intrinsic AGN/host galaxy ratio at *R* band = 5); (10) polarization fraction at *R* band relative to the intrinsic AGN; (11) observed polarization fraction at *R* band relative to the reddened AGN; (12) shows whether the AGN is at high ($z \geqslant 0.3$) redshift which needed to be taken into account during modeling (see Sections 5.5.1 and 5.5.2); (13) observed host galaxy contribution at *R* band.
[a] High S/N *XMM-Newton* spectra found *0918+2117* to be variable in X-rays and to have absorption, $N_H \sim 4 \times 10^{21}$ cm^{-2} in the higher flux state (Pounds & Wilkes 2007), which is consistent with our optical/IR color modeling.
[b] This object does not have good *B* and *R* photometry to model the optical/IR colors.

because the extremely weak Hβ defied measurement. Such weak Hβ is possibly due to high extinction, so these objects may have higher intrinsic L([O III]).

All of the 2MASS objects with relatively well-determined *Chandra* C and B fluxes (with the exception of 0409+0758 and 2222+1952) follow the Mulchaey et al. (1994) relation to lower
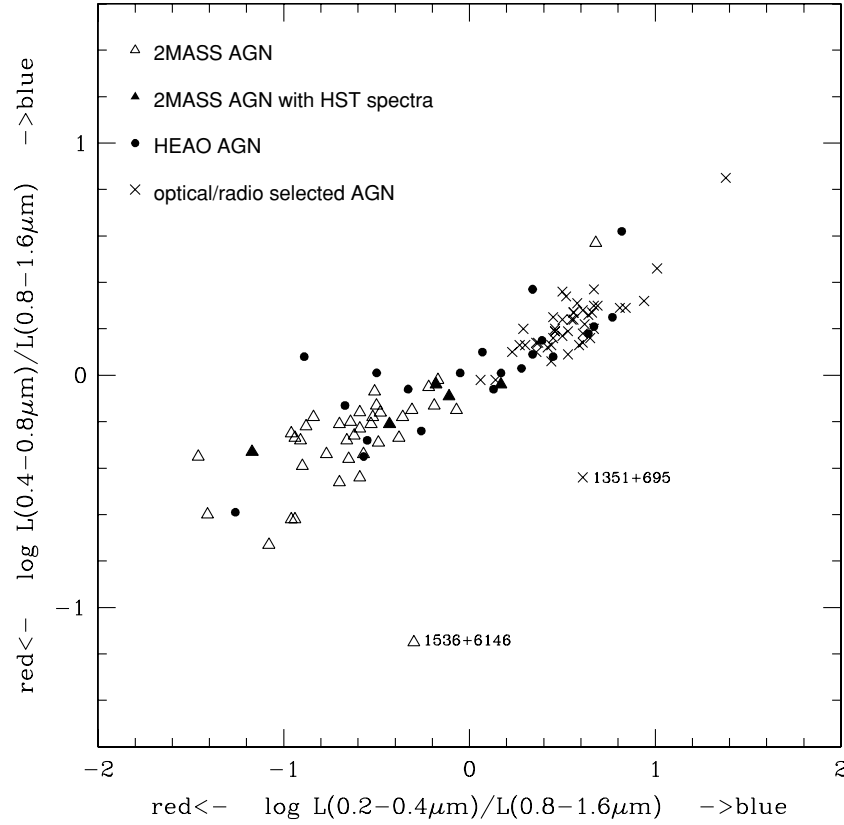
Figure 5. $L(0.4–0.8\ \mu m)/L(0.8–1.6\ \mu m)$ vs. $L(0.2–0.4\ \mu m)/L(0.8–1.6\ \mu m)$ color–color diagram. 2MASS AGNs are indicated by triangles (with those having *HST* spectra being filled triangles), hard-X-ray-selected *HEAO* AGNs (Kuraszkiewicz et al. 2003) by filled circles, and optical/radio-selected AGNs (Elvis et al. 1994) with crosses.

Table 8
Dependence of the Observed Optical and NIR Colors on Redshift

Observed Color	Redshift Dependence	Redshift Range
$(J − K) =$	$(2.013 ± 0.005) − (0.585 ± 0.062) × z$	$0 < z < 0.17$
$(J − K) =$	$(2.248 ± 0.056) − (1.947 ± 0.269) × z$	$0.18 \leqslant z < 0.24$
$(J − K) =$	$(2.132 ± 0.021) − (1.575 ± 0.047) × z$	$0.25 \leqslant z < 0.64$
$(J − K) =$	$(1.143 ± 0.001) − (0.035 ± 0.001) × z$	$0.65 \leqslant z \leqslant 1.50$
$(B − K) =$	$(3.526 ± 0.001) − (2.161 ± 0.001) × z$	$0 < z \leqslant 0.5$
$(B − K) =$	$(2.849 ± 0.002) − (0.794 ± 0.004) × z$	$0.51 < z \leqslant 0.7$
$(B − K) =$	$(2.255 ± 0.001) + (0.045 ± 0.001) × z$	$0.71 < z \leqslant 1.5$
$(B − R) =$	$(0.595 ± 0.001) − (0.702 ± 0.001) × z$	$0 < z \leqslant 0.47$
$(B − R) =$	$(0.024 ± 0.001) + (0.559 ± 0.001) × z$	$0.48 \leqslant z \leqslant 1.10$

Note. Colors are calculated using the median AGN SED of the optical/radio-selected quasars from Elvis et al. (1994).

X-ray fluxes, implying that the observed X-ray flux in these objects is dominated by direct rather than scattered light and is thus a good indicator of the AGN's intrinsic X-ray emission. The remainder of the sample, with low S/N (*A*) *Chandra* spectra, has lower hard-X-ray-to-[O III] flux ratios by a factor of 10–100. Possible explanations include the following:

1. The X-ray fluxes are intrinsically weak relative to the AGN ionizing optical/UV flux (that produces [O III] emission). The [O III] versus hard-X-ray luminosity correlation breaks down, because the hard X-ray flux is no longer a good indicator of AGN luminosity.
2. The X-ray absorption is higher than we assume (in *A* spectra we assumed absorption of $N_H = 7.6 × 10^{21}$ cm^{-2}, the median of the *C* sample).

3. The X-ray photon index is flatter than the normal, $\Gamma = 2$ photon index assumed for the *B* and *A* spectra, leading to an underestimate of the X-ray flux. The median photon index for the *C* sample is $\Gamma_X = 1.5$ (B. J. Wilkes et al. 2008, in preparation), however this change in photon index is too small to explain the 1–2 order-of-magnitude lower X-ray fluxes.

The first two options are discussed in detail in the following section.

6.2. Objects that do not Follow the [O III] Versus X Relation

As discussed in the previous section, objects with 10–100× lower than typical (E94) hard-X-ray-to-[O III] flux ratios are ei-

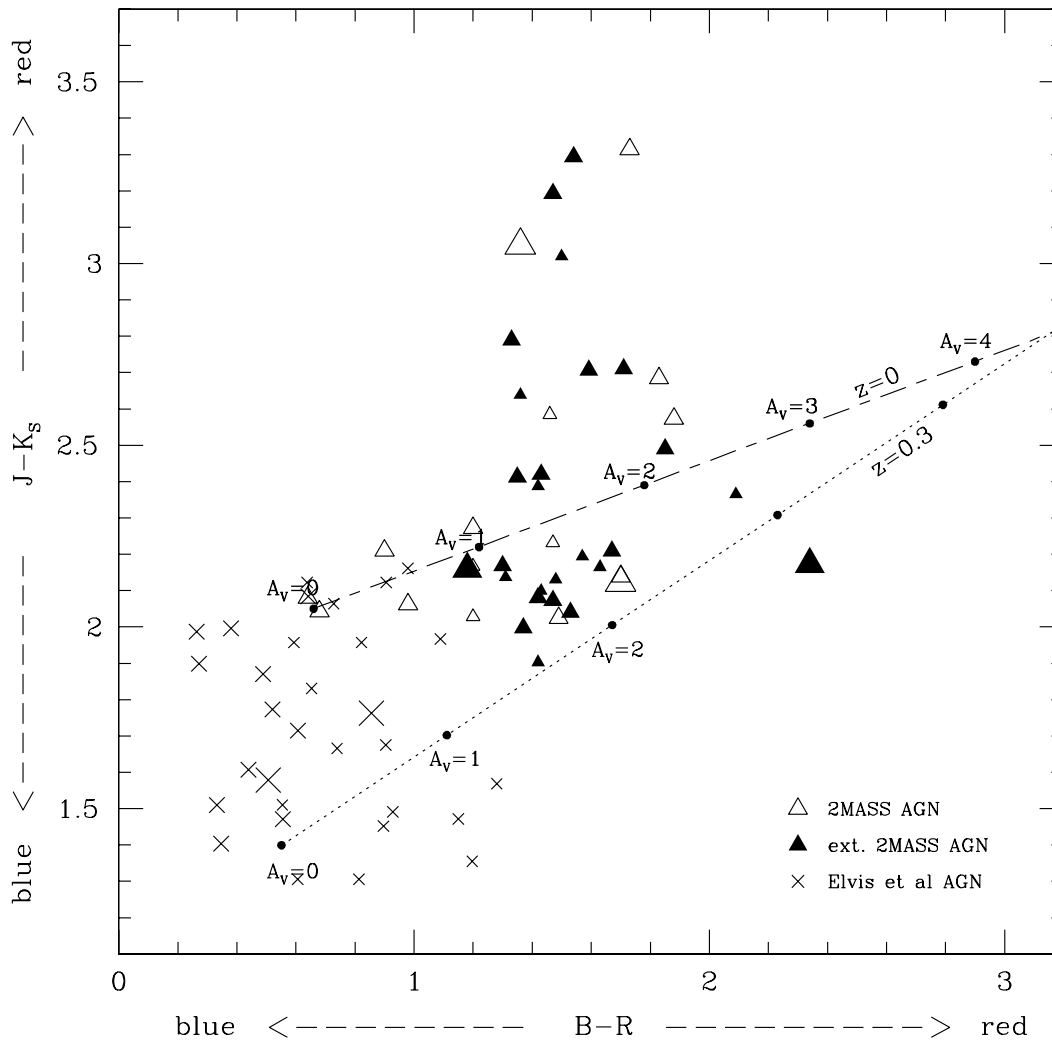**Figure 6.** Observed $J - K_S$ color vs. observed $B - R$ color diagram. Triangles denote 2MASS objects, where filled triangles are optically extended sources on B and R plates, and open triangles are point sources. Crosses denote objects in the Elvis et al. (1994) sample (colors not corrected for redshift or host galaxy; $J - K$ converted to $J - K_S$ using Bessell 2005). The size of the triangles and crosses is proportional to redshift (smallest symbols are for $z \leqslant 0.15$, medium symbols for $0.15 < z \leqslant 0.3$, and largest symbols for $0.3 < z < 0.4$). The long-dash–short-dash line shows colors of the median blue optical/radio-selected AGN SED (Elvis et al. 1994; $z = 0$, corrected for host galaxy) at $z = 0$ reddened by dust with A_V changing from 0 to 4 mag. The dotted line shows colors of this median at $z = 0.3$ ($\simeq$ highest redshift in our red 2MASS sample).

ther intrinsically X-ray weak or have high obscuration or both. The first group includes three AGNs: *0234+2438, 1258+2329, 2222+1959* with the lowest $F(1\ \mathrm{keV})/F_K$ and $F(1\ \mathrm{keV})/F_B$ ratios in the sample. Their optical and IR colors are blue ($B - R$= 0.68–1.18 mag and $J - K_S$ = 2.04–2.16 mag) and, when modeled, imply an unreddened AGN ($A_V \leqslant 1$ mag) with a weak ($<6\%$) host galaxy contribution at R band (see Table 7). Their optical spectra (Figure 1) show strong Fe II emission and weak (relative to Hβ) [O III] emission, resembling NLS1s and BALQSOs, which are thought to have high L/L_{Edd} ratios (e.g., Boller et al. 1996; Pounds et al. 1995; Kuraszkiewicz et al. 2000) that produce weak X-rays relative to the BBB (Witt et al. 1997). The second group includes *0348+1255, 0748+6947, 0955+1705, 1040+5934, 1307+2338, 1453+1353*, whose optical/IR colors are modeled with a highly obscured AGN (A_V = 10–15, i.e., N_H = (1.6–2.3) × 10^{22} cm^{-2}), and the host galaxy contributing 96%–100% to the total observed light at R band (Table 7). These objects have more absorption than assumed in the spectral fits, $N_H = 7.6 \times 10^{21}$ cm^{-2}, and thus their de-absorbed X-ray fluxes are underestimated causing them to diverge from the hard-X-

ray versus [O III] correlation. In the next section, we will further confirm high obscuration in these sources by studying their far-IR *IRAS* colors.

In summary, AGNs that are highly obscured ($N_H \approx 10^{22}$ cm^{-2}) or have high L/L_{Edd} ratios do not follow the [O III] versus hard-X-ray relation so the intrinsic hard-X-ray flux cannot be estimated from their [O III] emission. In the first case, the highly obscured X-rays are dominated by scattered light and hence appear weak and unabsorbed. In the second case, high L/L_{Edd} produces a more luminous BBB (see Witt et al. 1997), and so the X-rays seem relatively weak compared to the AGN's ionizing optical/UV continuum that produces the [O III] emission.

6.3. N_H Estimates from the Far-IR Flux Ratios

Twelve of the objects in our red 2MASS AGN sample were observed by IRAS. We plot their 12 μm to 60 μm flux ratio versus the 25 μm to 60 μm flux ratio dependence in Figure 16. As before, 2MASS AGNs with *Chandra* flux measurements of various S/N levels are indicated. Again, we compare the
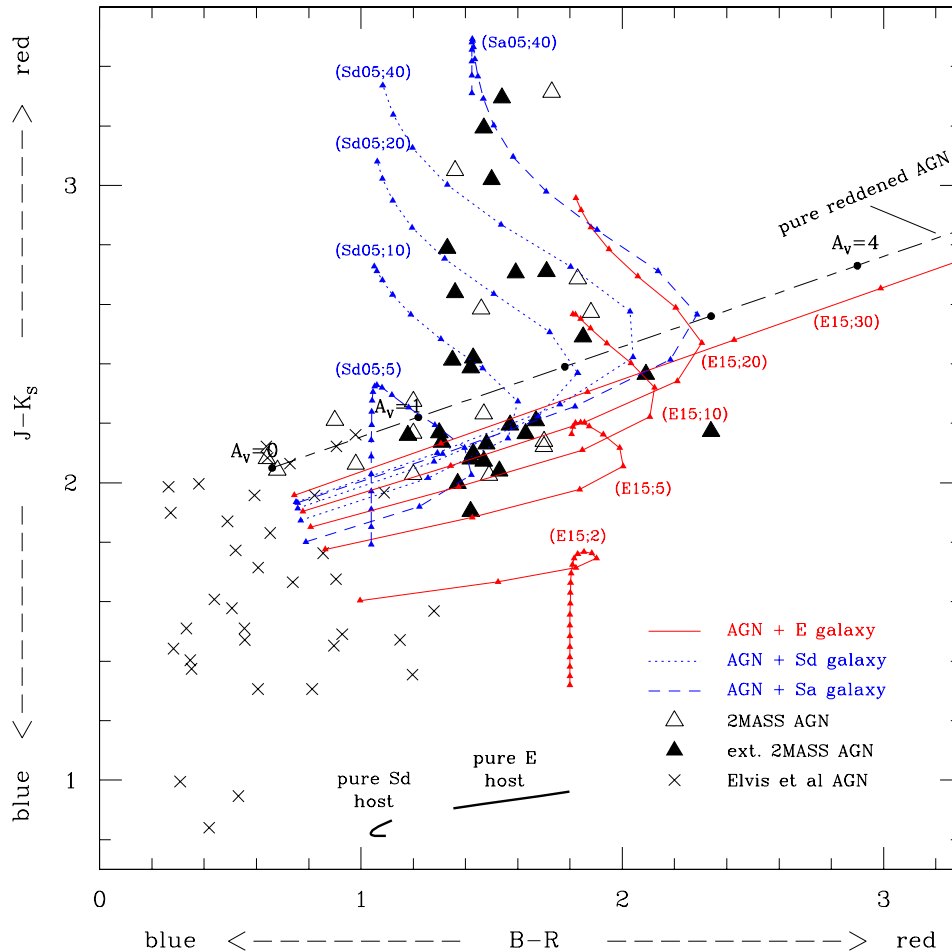
Figure 7. Colors of a reddened AGN combined with contributions from a host galaxy ($z = 0$). The solid lines represent AGNs with an elliptical host with a 15 Gyr stellar population (reddest in $B - R$ color), the dotted lines an AGN with an Sd host with a 5 Gyr stellar population (bluest in $B - R$), and the dashed line an AGN with an Sa host with a 5 Gyr stellar population (intermediate $B - R$ color). Each curve starts at the colors of an unreddened ($A_V = 0$) AGN + host galaxy (bluest optical/IR colors) and extends to the reddened $A_V = 10$ mag AGN + host galaxy in steps of 1 mag denoted by small triangles on the curves. Three curves, (E15;2), (Sd05;5), and (Sa05;40), have been extended to $A_V = 20$. Numbers in parenthesis give the host galaxy type and age of stars followed by the intrinsic, unreddened AGN/host galaxy flux ratio at the R band (e.g., (E15;20) is an E host with 15 Gyr stars and AGN/host flux ratio = 20). The thick solid curves indicate pure host galaxy (E and Sd) colors changing with star age (from 1 to 15 Gyr). The triangles and crosses represent the observed colors of red 2MASS and Elvis et al. (1994) AGN samples, respectively. (A color version of this figure is available in the online journal.)

2MASS sources with the optical/radio AGN sample of E94 (crosses) and X-ray-selected *HEAO* AGN (Kuraszkiewicz et al. 2003; open circles) but this time add Seyfert 2 nuclei from Heisler et al. (1997), some of which have broad-line emission observed in polarized light (stars) and some do not, possibly indicating higher obscuration (open triangles). The diagonal line shows the change in far-IR colors with differing amounts of dust reddening. As can be seen from the figure, the 2MASS objects have N_H in the range of 10^{22}–10^{23} cm^{-2}, consistent with N_H estimated from X-rays, although most of the fluxes are upper limits and strong conclusions cannot be drawn. The four low S/N (A) *Chandra* sources (*0748+6947, 1040+5934, 1307+2338, 1453+1353*) show the highest $N_H \sim 10^{23}$ cm^{-2}, confirming that these sources may have more absorption than the assumed $N_H = 7.6 \times 10^{21}$ cm^{-2} (*Chandra C* fits median) that was also suggested by the $B - R$ and $J - K_S$ color modeling.

7. EMISSION-LINE PROPERTIES AND COMPARISONS WITH OTHER SAMPLES

We measure the rest-frame equivalent widths, fluxes and full width at half-maximum (FWHM) of the strongest optical emis-

sion lines (Hα, Hβ, [O III] λ5007, Fe II, and [O II] λ3728) in the red 2MASS AGN spectra presented in Figure 1. The emission-line measurements were made using the modeling software *Sherpa*[12] (Freeman et al. 2001) originally developed for the *Chandra* mission, but applicable to any grid of multidimensional fitting. Each spectrum was fitted by a reddened power-law continuum (reddening curves of Cardelli et al. 1989 were used) to regions of the spectrum away from strong emission lines and blended iron emission. The blended optical (4400 Å $< \lambda_{rest} < 7000$ Å) iron emission was modeled using the Boroson & Green (1992) templates, broadened by convolving with Gaussian functions of width between 900 and 10,000 km s^{-1}, separated by steps of 250 km s^{-1}. This included several steps: (1) estimation of a crude flux normalization for a 2000 km s^{-1} template, (2) estimation of the width of the iron template, and (3) a fit of both the amplitude and width of the template. This was followed by another iteration of the continuum and the iron emission modeling. Finally, the emission lines were fitted with a single Gaussian, unless two or three components (broad, narrow, and intermediate, in the case of Hβ and Hα) were clearly needed.

---

[12] http://cxc.harvard.edu/sherpa/index.html
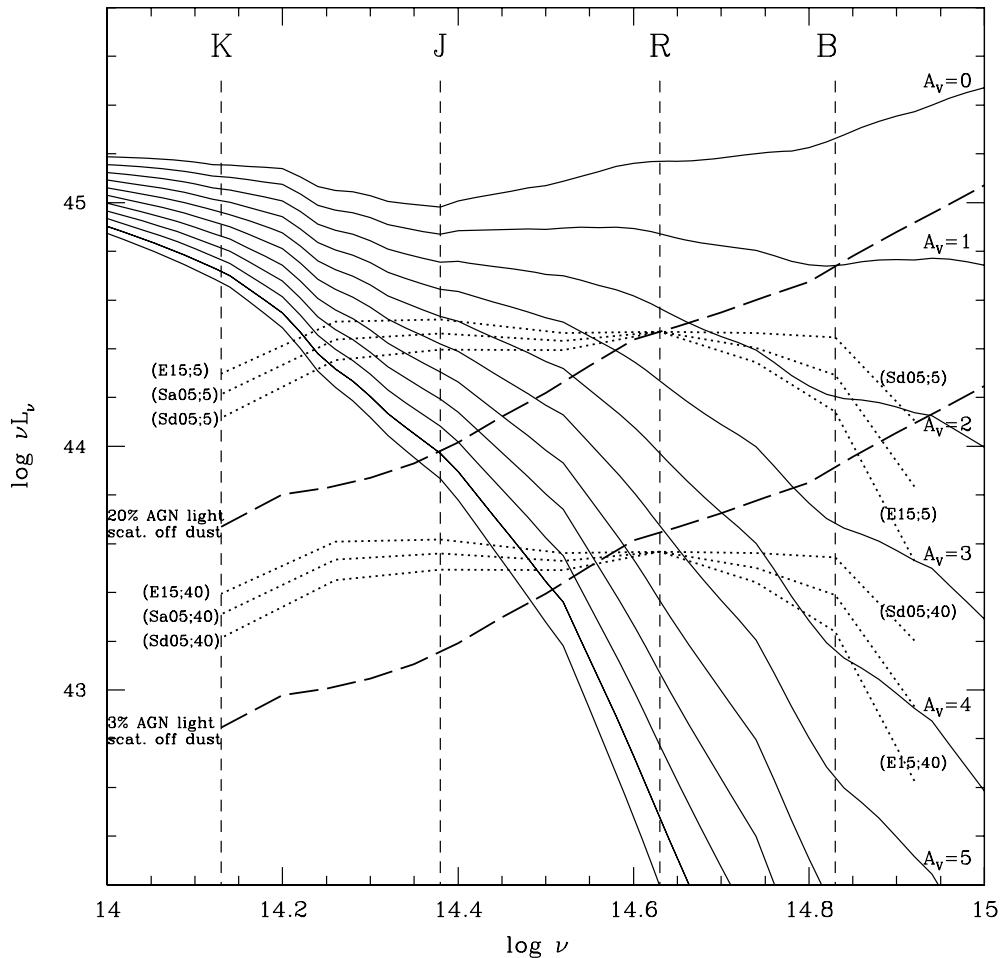
Figure 8. SEDs of a pure AGN (Elvis et al. 1994; median SED) reddened by A_V ranging from 0 to 10 mag (solid lines). The dotted lines show SEDs of three host galaxy templates from Buzzoni (2005; elliptical galaxy with a 15 Gyr stellar population, and Sd and Sa galaxies with a 5 Gyr stellar population) normalized in the R band to be five times and 40 times (top three and bottom three dotted curves, respectively) weaker than the AGN. The long-dashed lines show SED of nuclear AGN light scattered off dust normalized to 3% (lower dashed line) and 20% (upper dashed line) in the R band. The frequency of the J, K, R, and B band effective wavelengths are indicated by short-dashed lines. SEDs are at $z = 0$.

Multiple-line components were usually required for higher S/N spectra. The FWHM, peak amplitude of the Gaussian, and the position of the emission line were modeled. All model parameters were determined from a minimization of the χ^2 statistic with the Gehrels variance function (Gehrels 1986) and using the Powell optimization method. This technique proved successful in the analysis of spectra from the Large Bright Quasar Survey (LBQS) sample (Forster et al. 2001) and the Faint Object Spectrograph (FOS)/*HST* spectra (Kuraszkiewicz et al. 2002, 2004). We present the 2MASS AGN emission-line measurements in Table 9 and the fits are presented in a companion paper Kuraszkiewicz et al. (2009) and on our Web site, http://hea-www.harvard.edu//joasia/2MASSAGN/emissionline fits/table.html.

We calculate the mean equivalent widths for the red 2MASS AGNs and compare them with those obtained from the SDSS composite quasar spectrum (Vanden Berk et al. 2001) and the LBQS sample (Forster et al. 2001) in Table 9. The mean equivalent widths of Hα, Hβ, and Fe II of the 2MASS sample agree with the means measured for the SDSS composite. The Fe II mean is consistent with the LBQS mean, but mean $W_\lambda(H\beta)$ is lower for the 2MASS sample than the LBQS sample and is likely due to the presence of Types 1.8–2 objects that lie preferably at lower Hβ equivalent widths (see Figure 17(a)). The LBQS sample consists mostly

of broad-lined QSO and so is biased against these edge-on objects.

The mean equivalent widths of the forbidden [O III] and [O II] emission lines are much higher in the 2MASS sample than in the LBQS sample and the SDSS composite (Table 9). The distributions of the [O III] equivalent widths and the comparison with the LBQS sample is shown in Figure 17(b). The K–S test showed a 99% probability that the distributions are different such that the 2MASS sample is deficient in low EW([O III]) or overpopulated with high EW([O III]) sources. Under the assumption that viewing angle is the primary difference between the red 2MASS AGN and other AGN/QSOs (as suggested by the SEDs), we can explain their higher [O II] and [O III] equivalent widths as due to a lack of face-on objects (where the continuum is unobscured and so brighter) and/or to a higher number of inclined objects in the sample. This is the case since 85% of the sample consists of Types 1.2–2. In the unification model, Type 1.0 sources are those thought to be face-on, while Types 1.2, 1.5 etc., where the relative strength of the broad lines decreases relative to the narrow lines, are progressively more edge-on.

Assuming that obscuration increases with inclination angle (Baker 1997), the moderate amount of obscuration $N_H \approx 10^{21}$–10^{22} cm^{-2} found in our 2MASS sample is consistent with moderate inclination angles for the obscuring torus or accretion disk, such that we look through a wind or atmosphere above
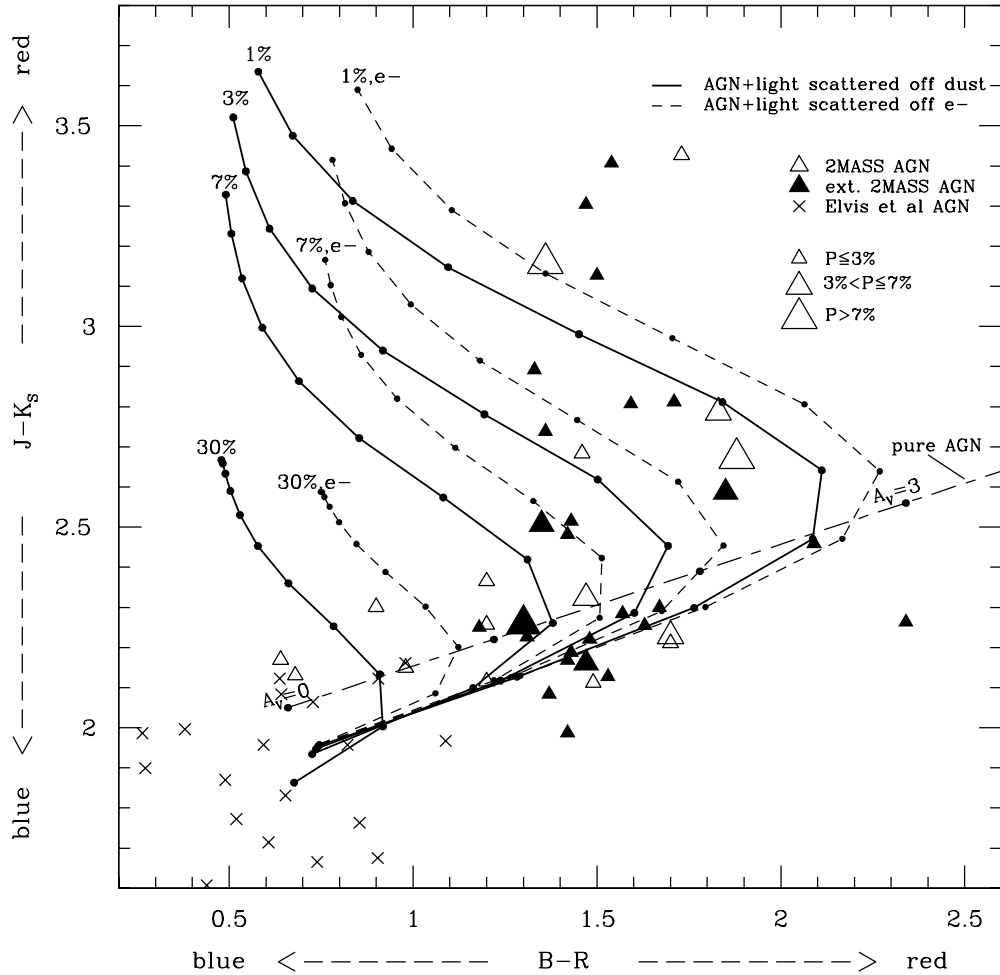
Figure 9. Effect of adding scattered AGN light to a reddened AGN continuum on the optical/NIR colors ($z = 0$). The long-dash–short-dash line shows the colors of a pure reddened AGN (small dots are at $A_V = 0, 1, 2, 3$ mag). The thick solid curves show the effect of adding to this reddened AGN continuum (Elvis et al. 1994; median AGN SED reddened by dust with A_V ranging from 0 to 10 mag—loci represented by small circles) an unreddened AGN continuum (Elvis et al. 1994; median SED) scattered off dust at scattering angle $\theta = 90°$. The dashed lines show the same but with scattering off electrons at $\theta = 90°$ (i.e., scattering is independent of wavelength). Scattered intrinsic AGN light at levels 1%, 3%, 7%, and 30% in the R band were added, which translates to 1%, 3%, 6.5%, and 23% scattered light relative to the total observed (AGN+scattered) flux at the R band, if the observed AGN is not reddened, or to a higher scattered light contribution if the observed AGN is reddened. Each 2MASS source is represented by a triangle, with size proportional to the amount of polarization measured at the R band. Extended sources are denoted by filled triangles. The triangles and crosses represent the observed colors of red 2MASS and Elvis et al. (1994) AGN samples, respectively.

the main structure. Alternatively, these column densities are consistent with a view through a host galaxy disk. The latter is supported by the findings of Marble et al. (2003), who studied the *HST*/WFPC2 *I*-band images of a different subset of 2MASS AGN, and concluded that these AGNs reside mostly in inclined host galaxies with inclination angles of $i = 50°-75°$. AGNs with such inclination angles will reshape the EW([O III]) distribution by adding higher equivalent widths to the distribution.

8. THE SAMPLE—A MIXED BAG OF OBJECTS

After analyzing the global properties of our red 2MASS AGN sample, we attempt to understand its make-up by looking at groups of objects divided according to optical type. We note that the spectra become redder in both $B - R$ and $J - K_S$ colors as we progress from Type 1, through the intermediate Types 1.2–1.9, to Type 2. This can be explained in terms of orientation-dependent dust obscuration.

8.1. The Type 1s

Only one object (*2344+1221*) in this class has an optical spectrum that looks like a genuine Type 1 object with broad

Balmer emission lines and strong [O III] emission. It lies on the borderline of our red $J - K_S$ selection, with $J - K_S = 1.997$. High S/N *XMM-Newton* observations (Pounds et al. 2005) show an obscuring column, $N_H \sim 10^{22}$ cm^{-2}, of moderately ionized gas or a lower column, $N_H \sim 3 \times 10^{21}$ cm^{-2}, of cold gas. Our optical/IR color modeling of this object implies reddening of $A_V = 2-3$, favoring the second scenario. Six other objects in this class show strong optical Fe II emission and extremely weak (relatively to Hβ) or nonexistent [O III] emission, resembling the spectra of NLS1/BALQSOs (Osterbrock & Pogge 1985; Weymann et al. 1981). The red $J - K_S > 2$ selection seems to pick a high percentage (86%) of these objects among Type 1s. It has been found that the IR SEDs of some NLS1s such as Mrk 1239, Mrk 766, and I Zw 1 (Rodriguez-Ardila & Mazzalay 2006; Rodriguez-Ardila et al. 2005; Rudy et al. 2000) show a significant 2.2 μm bump that can be modeled with a blackbody function with $T = 1200$ K, a temperature that is close to the evaporation temperature of graphite grains, indicating hot dust close to the nucleus. Hence, the red $J - K_S > 2$ selection picks Type 1 sources with high L/L_{Edd} *and* large amounts of hot circumnuclear dust. The optical/NIR colors of the red 2MASS Type 1s are mostly blue ($B - R \leqslant 1.4$ mag and $J - K_S <$

Table 9
Optical Emission-Line Properties

Name	$W_\lambda([\text{O\,II}]\lambda3727)$	$W_\lambda(\text{Fe\,II})$	$W_\lambda(\text{H}\beta\lambda4861)$	$W_\lambda([\text{O\,III}]\lambda5007)$	$W_\lambda(\text{H}\alpha\lambda6548)$	Narrow $\frac{H\alpha}{H\beta}$	Broad $\frac{H\alpha}{H\beta}$
0007+1554a	$53.8^{+2.3}_{-2.3}$	$2.9^{+0.9}_{-0.9}$	$40.0^{+2.4}_{-2.3}$	$125.9^{+3.9}_{-3.5}$	$314.3^{+7.1}_{-6.1}$	4.79	11.22
0007+1554b	$47.5^{+2.3}_{-2.2}$	$37.6^{+1.0}_{-1.0}$	$58.3^{+4.8}_{-4.3}$	$110.3^{+3.6}_{-3.7}$	$171.8^{+5.0}_{-5.3}$	3.18[a]	3.21[a]
0050+2933	$39.3^{+1.5}_{-1.5}$	$22.4^{+0.6}_{-0.6}$	$41.1^{+3.9}_{-3.6}$	$61.4^{+1.8}_{-1.7}$	$76.4^{+2.8}_{-2.2}$	3.86	1.64
0108+2148	$84.6^{+2.8}_{-2.8}$	$19.0^{+0.7}_{-0.7}$	$43.5^{+1.7}_{-1.7}$	$383.6^{+8.2}_{-6.9}$	$299.2^{+6.5}_{-10.0}$	0.00	0.00
0120+2003	$16.1^{+9.5}_{-0.9}$	$11.3^{+0.6}_{-0.6}$	$0.0^{+0.2}_{-0.0}$	$0.0^{+0.4}_{-0.0}$	$18.1^{+1.2}_{-0.0}$	0.00	0.00
0120+2003	$11.8^{+1.2}_{-1.2}$	$14.0^{+0.8}_{-0.8}$	$0.0^{+0.5}_{-0.0}$	$1.2^{+0.7}_{-0.6}$	$17.3^{+1.7}_{-1.3}$	0.00	0.00
0157+1712	$886.0^{+17.0}_{-17.0}$	$46.8^{+1.0}_{-1.0}$	$95.0^{+55.0}_{-3.6}$	$74.6^{+2.9}_{-2.5}$	$134.7^{+5.8}_{-6.4}$	0.00	0.00
0221+1327	$26.3^{+1.8}_{-1.7}$	$44.6^{+0.7}_{-0.7}$	$36.3^{+2.7}_{-2.6}$	$41.4^{+2.0}_{-1.8}$	$53.1^{+3.3}_{-3.2}$	2.52	1.74
0234+2438	$4.0^{+1.7}_{-1.3}$	$20.5^{+0.6}_{-0.6}$	$36.8^{+2.6}_{-2.5}$	$23.0^{+1.5}_{-1.4}$	$356.7^{+6.3}_{-6.7}$	4.93	5.69
0348+1255	$0.0^{+0.0}_{-0.0}$	$0.0^{+0.0}_{-0.0}$	$0.0^{+0.0}_{-0.0}$	$0.0^{+0.0}_{-0.0}$	$0.0^{+0.0}_{-0.0}$	0.00	0.00
0409+0758a	$24.4^{+1.4}_{-13.0}$	$51.8^{+1.1}_{-1.1}$	$86.1^{+3.5}_{-3.4}$	$83.9^{+2.8}_{-2.8}$	$281.0^{+8.10}_{-7.90}$	9.12	1.84
0409+0758b	$0.0^{+0.0}_{-0.0}$	$35.3^{+2.4}_{-2.4}$	$106.0^{+11.0}_{-9.8}$	$74.6^{+6.6}_{-6.4}$	$370.0^{+25.00}_{-25.00}$	5.97[a]	1.97[a]
0420−2047	$5.7^{+0.8}_{-0.8}$	$52.8^{+0.7}_{-0.7}$	$70.0^{+2.8}_{-2.7}$	$23.8^{+1.6}_{-1.6}$	$280.5^{+6.7}_{-5.9}$	0.00	0.00
0748+6947a	$138.1^{+3.9}_{-4.0}$	$15.9^{+0.6}_{-0.6}$	$23.7^{+1.5}_{-1.4}$	$82.1^{+2.8}_{-2.4}$	$120.1^{+4.5}_{-4.5}$	2.08[a]	0.00[a]
0748+6947b	$87.6^{+7.1}_{-6.9}$	$51.3^{+2.4}_{-2.4}$	$69.0^{+16.0}_{-13.0}$	$61.3^{+5.7}_{-5.5}$	$6.0^{+4.2}_{-3.2}$	0.93	0.00
0918+2117a	$15.3^{+1.3}_{-1.2}$	$72.4^{+1.0}_{-1.0}$	$55.5^{+2.4}_{-2.4}$	$64.5^{+2.5}_{-2.5}$	$294.3^{+6.7}_{-2.5}$	0.00	0.00
0918+2117b	$13.8^{+1.3}_{-1.2}$	$44.2^{+0.7}_{-0.7}$	$38.3^{+2.1}_{-2.3}$	$57.5^{+2.4}_{-2.5}$	$425.0^{+13.0}_{-13.0}$	0.00	0.00
0938+0057	$0.0^{+0.0}_{-1.1}$	$21.0^{+1.1}_{-1.0}$	$102.1^{+4.6}_{-4.2}$	$38.7^{+2.2}_{-2.2}$	$682.0^{+13.0}_{-13.0}$	0.00	0.00
0955+1705a	$5.3^{+1.1}_{-0.9}$	$39.6^{+0.9}_{-0.9}$	$106.3^{+3.7}_{-3.6}$	$40.6^{+1.8}_{-1.8}$	$160.9^{+7.7}_{-7.7}$	3.72	0.87
0955+1705b	$5.5^{+1.0}_{-0.9}$	$36.0^{+1.0}_{-1.0}$	$94.7^{+4.0}_{-3.8}$	$39.3^{+1.9}_{-1.9}$	$125.0^{+11.0}_{-9.0}$	3.38[a]	0.88[a]
1021+6311a	$55.9^{+2.2}_{-2.1}$	$42.1^{+0.8}_{-0.8}$	$57.4^{+6.6}_{-6.1}$	$82.1^{+2.9}_{-2.9}$	$86.9^{+6.4}_{-5.7}$	3.43[a]	1.30[a]
1021+6311b	$0.0^{+0.1}_{-0.0}$	$9.4^{+1.6}_{-1.6}$	$33.2^{+11.0}_{-8.4}$	$77.4^{+6.5}_{-6.3}$	$51.4^{+7.8}_{-7.0}$	1.86	1.36
1027+1219a	$10.0^{+0.0}_{-0.0}$	$21.1^{+0.8}_{-0.7}$	$48.3^{+2.1}_{-2.1}$	$36.1^{+1.8}_{-1.8}$	$235.3^{+5.8}_{-5.8}$	0.00	0.00
1027+1219b	$8.1^{+3.4}_{-2.7}$	$52.8^{+2.4}_{-2.4}$	$79.0^{+12.0}_{-11.0}$	$55.1^{+5.9}_{-5.6}$	$0.0^{+0.0}_{-0.0}$	0.00	0.00
1040+5934a	$63.5^{+2.2}_{-2.2}$	$0.0^{+0.4}_{-0.9}$	$6.6^{+0.9}_{-0.8}$	$19.6^{+1.2}_{-1.2}$	$126.6^{+4.8}_{-4.6}$	0.00	0.00
1040+5934b	$51.1^{+5.2}_{-5.0}$	$26.2^{+2.5}_{-2.5}$	$19.0^{+14.0}_{-9.0}$	$20.6^{+3.6}_{-3.3}$	$78.0^{+12.0}_{-11.0}$	6.19[a]	2.87[a]
1049+5837	$14.8^{+1.1}_{-1.1}$	$0.0^{+0.1}_{-0.0}$	$17.5^{+2.3}_{-2.2}$	$69.4^{+2.5}_{-2.4}$	$138.0^{+4.6}_{-4.5}$	3.63	12.31
1051+3539a	$0.0^{+0.0}_{-0.0}$	$27.5^{+0.9}_{-1.0}$	$21.2^{+2.7}_{-0.8}$	$98.8^{+3.1}_{-3.0}$	$148.5^{+4.4}_{-3.9}$	0.00	0.00
1051+3539b	$23.5^{+1.5}_{-1.4}$	$11.5^{+0.6}_{-0.6}$	$41.8^{+5.8}_{-5.1}$	$39.5^{+1.8}_{-1.8}$	$96.5^{+4.5}_{-3.9}$	3.07[a]	2.18[a]
1127+2432a	$0.0^{+0.0}_{-0.0}$	$7.3^{+1.0}_{-1.0}$	$22.0^{+2.6}_{-2.3}$	$22.3^{+1.6}_{-1.5}$	$147.9^{+4.8}_{-4.8}$	0.00	0.00
1127+2432b	$2.9^{+2.0}_{-1.5}$	$30.9^{+1.9}_{-1.9}$	$33.6^{+9.6}_{-7.7}$	$19.6^{+3.5}_{-3.2}$	$64.9^{+9.5}_{-8.5}$	2.04[a]	2.32[a]
1230+0302a	$13.0^{+1.0}_{-1.0}$	$15.8^{+0.6}_{-0.6}$	$63.2^{+2.9}_{-3.4}$	$55.0^{+2.1}_{-2.3}$	$484.6^{+7.6}_{-8.3}$	5.56[a]	8.07[a]
1230+0302b	$27.0^{+4.7}_{-4.3}$	$31.2^{+2.3}_{-2.3}$	$61.8^{+8.5}_{-7.6}$	$46.6^{+4.9}_{-4.7}$	$254.0^{+14.0}_{-13.0}$	1.83	4.42
1243−0802a	$44.6^{+1.7}_{-1.8}$	$20.0^{+0.7}_{-0.7}$	$52.0^{+2.0}_{-1.8}$	$301.0^{+6.4}_{-6.4}$	$266.9^{+5.7}_{-6.8}$	0.00	0.00
1243−0802b	$51.5^{+5.4}_{-5.2}$	$23.0^{+2.2}_{-2.2}$	$99.0^{+12.0}_{-10.0}$	$364.0^{+19.0}_{-19.0}$	$256.0^{+16.0}_{-16.0}$	2.9[a]	3.43[a]
1258+2329	$0.7^{+0.6}_{-0.2}$	$34.8^{+0.5}_{-0.5}$	$21.2^{+1.5}_{-1.5}$	$0.8^{+0.5}_{-0.4}$	$0.0^{+0.0}_{-0.0}$	0.00	0.00
1300+1632a	$36.8^{+0.0}_{-19.0}$	$23.3^{+0.7}_{-0.7}$	$47.0^{+6.6}_{-5.9}$	$40.4^{+1.8}_{-1.9}$	$98.3^{+10.0}_{-9.2}$	0.00	0.00
1300+1632b	$0.0^{+0.0}_{-0.0}$	$7.8^{+0.9}_{-0.9}$	$18.7^{+4.2}_{-3.8}$	$24.5^{+1.0}_{-2.7}$	$29.8^{+5.0}_{-4.2}$	8.64[a]	1.23[a]
1307+2338	$0.0^{+0.0}_{-0.0}$	$14.9^{+1.0}_{-1.0}$	$0.0^{+0.0}_{-0.0}$	$0.0^{+0.0}_{-0.0}$	$87.6^{+4.7}_{-4.3}$	0.00	0.00
1317−1739	$350.0^{+180.0}_{-7.4}$	$0.0^{+0.0}_{-0.0}$	$45.3^{+2.1}_{-2.0}$	$72.0^{+2.0}_{-2.0}$	$166.0^{+19.0}_{-18.0}$	0.00	0.00
1350−0632	$7.7^{+1.4}_{-1.2}$	$45.5^{+0.6}_{-0.6}$	$51.1^{+2.1}_{-2.0}$	$4.1^{+0.8}_{-0.7}$	$346.9^{+8.3}_{-7.9}$	0.00	0.00
1402+2631	$1.5^{+0.3}_{-0.7}$	$50.6^{+0.7}_{-0.7}$	$78.8^{+2.5}_{-2.5}$	$10.8^{+0.9}_{-0.8}$	$0.0^{+0.0}_{-0.0}$	0.00	0.00
1418+6804a	$0.0^{+0.1}_{-0.0}$	$4.0^{+0.9}_{-0.9}$	$0.0^{+0.0}_{-0.0}$	$13.5^{+1.0}_{-1.1}$	$57.2^{+3.0}_{-2.6}$	0.00[a]	0.00[a]
1418+6804b	$0.0^{+0.1}_{-0.0}$	$31.7^{+2.2}_{-2.2}$	$0.0^{+0.0}_{-0.0}$	$11.6^{+3.2}_{-2.8}$	$38.9^{+8.1}_{-7.0}$	0.00	1.54
1453+1353a	$0.0^{+0.0}_{-0.0}$	$31.8^{+0.6}_{-0.6}$	$0.0^{+0.0}_{-0.0}$	$14.5^{+1.3}_{-1.1}$	$67.9^{+3.4}_{-3.4}$	0.00	0.00
1453+1353b	$0.0^{+0.3}_{-0.0}$	$8.9^{+1.7}_{-1.7}$	$0.0^{+0.0}_{-0.0}$	$16.0^{+3.6}_{-3.2}$	$30.5^{+7.2}_{-6.1}$	0.00	0.00
1501+2329a	$434.8^{+8.7}_{-8.8}$	$0.0^{+0.0}_{-0.0}$	$14.4^{+1.3}_{-1.1}$	$3.8^{+0.6}_{-1.7}$	$112.6^{+5.6}_{-5.5}$	0.00	0.00
1507−1225	$475.0^{+19.0}_{-18.0}$	$4.6^{+0.4}_{-0.5}$	$12.8^{+1.3}_{-1.2}$	$8.2^{+1.0}_{-1.0}$	$194.5^{+4.4}_{-5.2}$	0.00	0.00
1511+0518a	$0.0^{+0.0}_{-0.0}$	$0.0^{+0.0}_{-0.0}$	$31.2^{+3.1}_{-2.9}$	$70.8^{+3.0}_{-2.9}$	$45.7^{+5.6}_{-5.0}$	0.00	0.00
1511+0518b	$0.0^{+0.0}_{-0.0}$	$1.1^{+1.9}_{-1.1}$	$24.9^{+7.8}_{-7.5}$	$46.9^{+4.8}_{-4.6}$	$17.9^{+9.5}_{-6.4}$	0.44[a]	0.78[a]
1516+1900a	$0.0^{+0.0}_{-0.0}$	$0.0^{+0.0}_{-0.0}$	$0.0^{+0.0}_{-0.0}$	$0.0^{+0.0}_{-0.0}$	$0.0^{+0.0}_{-0.0}$	0.00	0.00
1516+1900b	$3.5^{+3.4}_{-1.7}$	$32.6^{+0.9}_{-0.9}$	$82.2^{+4.6}_{-4.3}$	$12.1^{+1.3}_{-1.3}$	$512.9^{+8.6}_{-8.6}$	5.29[a]	3.87[a]
1536+6146	...	...	...	...	...	...	...
1637+2221	$0.0^{+0.1}_{-0.0}$	$0.0^{+0.0}_{-0.0}$	$35.7^{+2.1}_{-1.9}$	$29.5^{+1.4}_{-1.3}$	$206.7^{+5.8}_{-6.0}$	0.00	0.00
1659+1834	$27.6^{+1.7}_{-1.6}$	$12.9^{+0.7}_{-0.7}$	$71.4^{+3.9}_{-3.8}$	$96.5^{+3.0}_{-3.1}$	$336.1^{+9.8}_{-4.7}$	3.32	4.55
1714+2602a	$1.5^{+0.9}_{-0.6}$	$53.6^{+1.2}_{-1.2}$	$74.7^{+2.5}_{-2.4}$	$11.9^{+1.3}_{-1.2}$	$253.9^{+7.1}_{-6.8}$	0.00	0.00
1714+2602b	$2.3^{+2.4}_{-1.3}$	$34.6^{+1.0}_{-1.0}$	$54.3^{+2.3}_{-2.2}$	$9.4^{+1.2}_{-1.1}$	$164.1^{+5.0}_{-5.0}$	0.00	0.00
1755+6751a	$74.2^{+2.7}_{-2.6}$	$0.0^{+0.1}_{-0.0}$	$0.0^{+0.1}_{-0.0}$	$22.8^{+1.4}_{-1.3}$	$208.0^{+13.0}_{-9.4}$	0.00	0.00
1755+6751b	$65.4^{+7.4}_{-6.8}$	$32.0^{+2.5}_{-2.2}$	$4.0^{+4.7}_{-4.1}$	$25.7^{+4.5}_{-4.1}$	$0.0^{+0.0}_{-0.0}$	0.00	0.00
2024−5723	$104.4^{+2.6}_{-2.6}$	$37.0^{+0.0}_{-0.0}$	$299.4^{+6.1}_{-6.0}$	$718.0^{+14.0}_{-12.0}$	$584.9^{+10.0}_{-9.6}$	2.61	4.17
2025−4958	$8.6^{+0.7}_{-0.7}$	$108.0^{+0.8}_{-0.8}$	$81.8^{+3.9}_{-3.7}$	$28.5^{+1.5}_{-1.5}$	$142.6^{+4.4}_{-7.1}$	0.72	4.10

Table 9
(Continued)

Name	$W_\lambda([\text{O\,II}]\lambda3727)$	$W_\lambda(\text{Fe\,II})$	$W_\lambda(\text{H}\beta\lambda4861)$	$W_\lambda([\text{O\,III}]\lambda5007)$	$W_\lambda(\text{H}\alpha\lambda6548)$	Narrow $\frac{\text{H}\alpha}{\text{H}\beta}$	Broad $\frac{\text{H}\alpha}{\text{H}\beta}$
2222+1952	$15.9^{+1.3}_{-1.3}$	$9.0^{+0.0}_{-0.0}$	$173.4^{+4.8}_{-4.8}$	$106.1^{+2.9}_{-2.9}$	$451.0^{+11.0}_{-11.0}$	1.74	3.17
2222+1959a	$1.7^{+0.8}_{-0.6}$	$12.7^{+0.8}_{-0.8}$	$120.6^{+3.8}_{-3.5}$	$51.2^{+2.0}_{-2.0}$	$722.0^{+10.0}_{-10.0}$	10.81[a]	4.34[a]
2222+1959b	$4.5^{+1.1}_{-0.9}$	$13.6^{+0.8}_{-0.8}$	$111.3^{+4.9}_{-4.1}$	$56.0^{+2.3}_{-2.2}$	$551.0^{+12.0}_{-10.0}$	4.16	3.27
2225+1958	$8.3^{+1.1}_{-1.1}$	$44.6^{+0.9}_{-0.9}$	$35.2^{+3.4}_{-3.5}$	$35.5^{+1.8}_{-1.8}$	$27.8^{+2.0}_{-2.4}$	0.00	0.00
2344+1221	$5.5^{+1.0}_{-0.9}$	$36.4^{+0.8}_{-0.8}$	$66.9^{+3.1}_{-2.9}$	$30.2^{+1.6}_{-1.6}$	$417.9^{+6.5}_{-7.0}$	4.33	4.62
Mean 2MASS	57.5 ± 8.7	24.1 ± 3.6	43.9 ± 6.6	59.8 ± 9.0	161.6 ± 24.4		
Mean SDSS QSO composite	1.56 ± 0.03	21.47 ± 0.22	46.21 ± 0.16	13.23 ± 0.16	194.52 ± 0.62		
Mean LBQS[b]	3.2 ± 0.4	23.8 ± 1.6	61.2 ± 3.4	21.6 ± 2.8	$\dots$		

Notes.
[a] This ratio was used in the PCA analysis in Kuraszkiewicz et al. (2009).
[b] For the LBQS sample we quote the Kaplan–Meier estimated means, which account for both the detections and upper limits in the data.

2.2 mag) and modeled as pure AGN ($A_V \leqslant 1$ mag) with little/no ($< 17\%$ at R band) host galaxy contribution (see Table 7). An exception is *1501+2329* with red optical color ($B - R = 1.9$ mag) and $J - K_S = 2.5$ mag, modeled as a reddened AGN ($A_V = 3$ mag) with a 30% host galaxy contribution. Absorbing column densities of the red 2MASS Type 1s agree with those obtained from X-ray fitting, where $N_H \leqslant 5.6 \times 10^{21}$ cm^{-2} is

consistent with typical values found in Type 1 AGN (Malizia et al. 1997). The polarization values in our 2MASS Type 1s are generally low, except in *1501+2329*, where $P = 3\%$, and in *1516+1900* for which $P = 9.3\%$.

1516+1900 has a polarized light spectrum dominated by broad Balmer lines and lacks narrow lines that are present in the total flux spectrum (Smith et al. 2000). The total flux spectrum
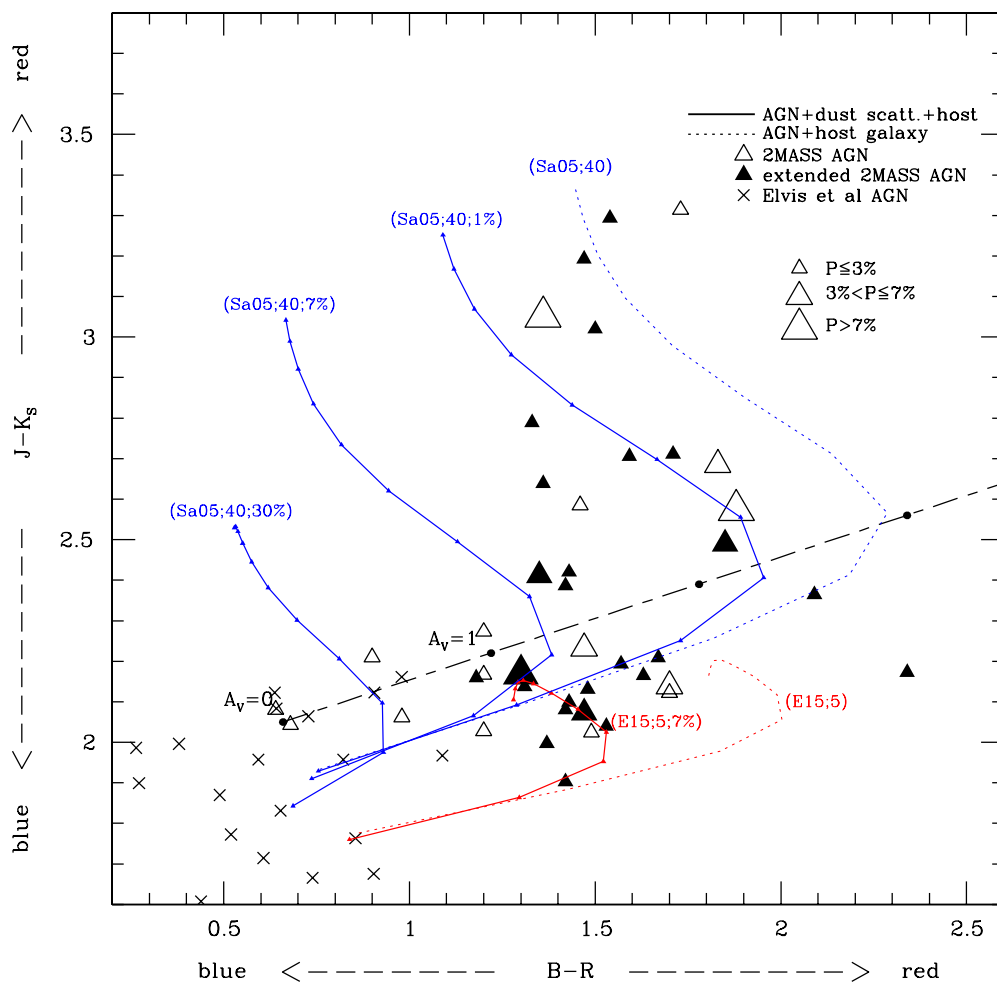
Figure 10. Effect of adding host galaxy and scattered AGN light to a reddened AGN continuum on the optical/NIR colors ($z = 0$). The solid curves represent the colors for a reddened AGN (A_V changing from 0 to 10 mag—small triangles at loci) + host galaxy (Sa spiral with 5 Gyr stars and elliptical with 15 Gyr stars: Sa05 and E15, respectively) + unreddened AGN light scattered off dust (1%, 7%, 30% of unreddened Elvis et al. 1994 median AGN SED added at the R band). The dotted lines show AGN + host galaxy colors as in Figure 7. The long-dash–short-dash line represents a pure reddened AGN where dots are at $A_V = 0, 1, 2, 3$ mag loci.
(A color version of this figure is available in the online journal.)
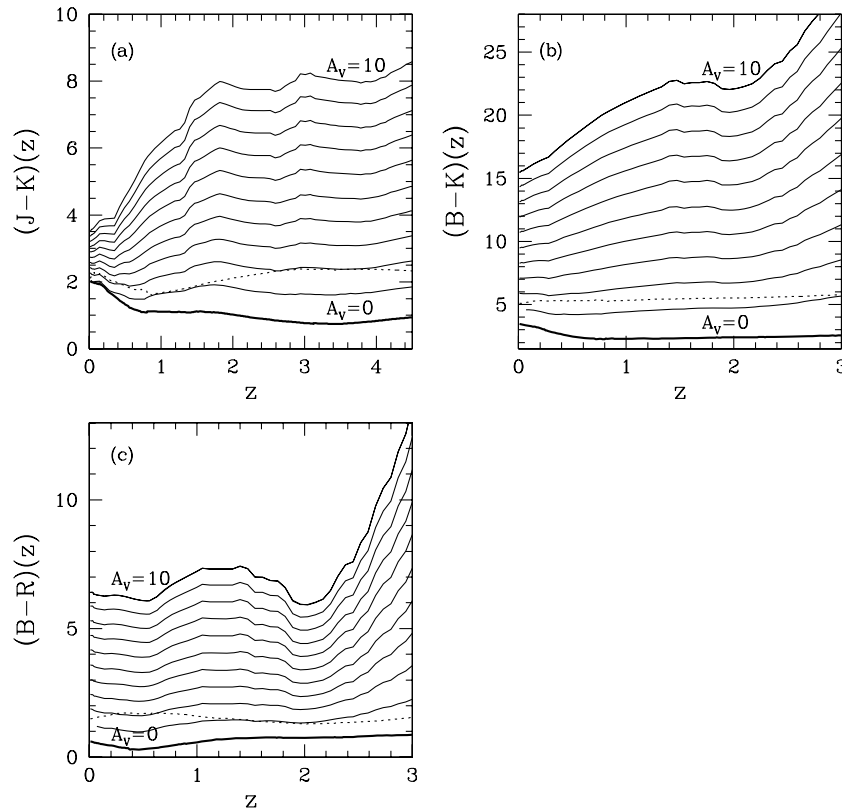
Figure 11. $J - K$, $B - K$, and $B - R$ observed color dependence on redshift. The bottom solid and bold curve in (a)–(c) shows the redshift dependence for the unreddened Elvis et al. (1994) median. The solid curves above this curve show the redshift dependence of the reddened Elvis et al. (1994) median where A_V changes from 1 to 10 mag. The dotted line in all figures shows the color redshift dependence when a 2MASS median is used ($A_V = 0$).
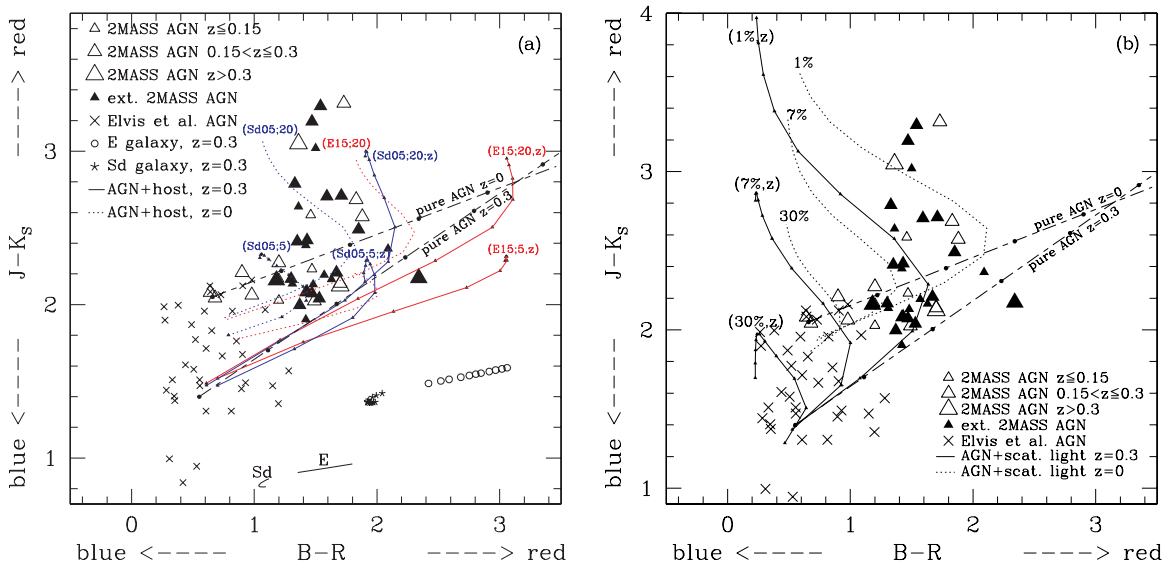
Figure 12. (a) Redshift dependence of the reddened AGN+host galaxy colors. Four reddened AGN + host galaxy curves were chosen from Figure 7: (E15;5), (E15;20), (Sd05;5), and (Sd05;20) (represented here by dotted lines) and redshifted to $z = 0.31$ (solid lines). (Sd05;5;z) denotes colors of a reddened AGN ($A_V = 0$–10 mag) + Sd (5 Gyr stars) host galaxy at $z = 0.31$, where the *rest-frame R* band intrinsic AGN to host galaxy ratio is 5. At the bottom of the figure, the thick solid lines marked with "Sd" and "E" show colors of a pure Sd and elliptical host galaxy at $z = 0$. These colors redshifted to $z = 0.31$ are marked as stars and circles, respectively. (b) Redshift dependence of the reddened AGN+scattered light colors. The dotted lines are the reddened AGN + dust-scattered intrinsic AGN light curves from Figure 9. The solid lines are the same curves (i.e., same 1%, 7%, 30% normalization of scattered light at *rest-frame R* and A_V changing from 0 to 10 mag) redshifted to $z = 0.31$. In both figures, the size of triangles is proportional to the redshift of the 2MASS AGNs. The filled triangles are extended sources, and the open triangles are point sources.

(A color version of this figure is available in the online journal.)

is blue in the optical with broad permitted emission lines and is extremely steep and red in the near-UV (see Figure 1). These

properties imply large amounts of dust lying near/within the NLR that partially obscure the AGN, scatter the continuum and
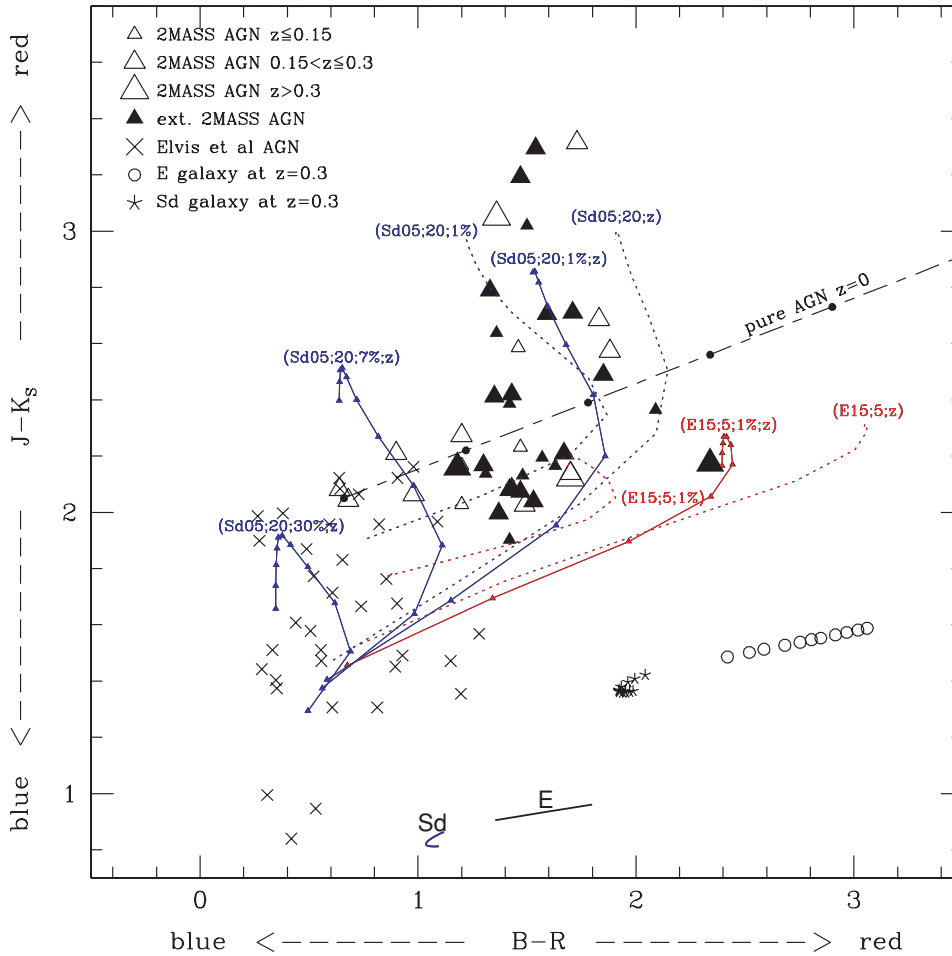
Figure 13. Redshift dependence of the $B - R$ and $J - K_S$ colors of a reddened AGN contaminated by both host galaxy emission and scattered AGN light. Two reddened AGN + host galaxy curves were chosen from Figure 7: (E15;5) and (Sd05;20). 1%, 7%, and 30% of scattered intrinsic AGN light at the R band were added to the (Sd05;20) curve and 1% to (E15;5) curve, and then redshifted to $z = 0.31$ yielding (Sd05;20;1%;z), (Sd05;20;7%;z), (Sd05;20;30%;z), and (E15;5;1%;z) curves (solid line). For comparison we also plot the redshifted AGN + host galaxy curves (E15;5;z) and (Sd05;20;z) from Figure 12(a) (dotted line). The triangles and crosses represent the observed colors of red 2MASS and Elvis et al. (1994) AGN samples, respectively. The size of the triangles is proportional to the redshift of the 2MASS AGNs.

(A color version of this figure is available in the online journal.)

BLR light and also redden the scattered light itself (as, e.g., in the case of IRAS+13349+2438; Hines et al. 2001).

8.2. The Types 1.2 and 1.5s

Most (10/17) of the optical spectra in this class are flat ($B - R \sim 1.4$ mag) in F_λ versus λ, four are red ($B - R > 1.5$ mag), and three are blue ($B - R \sim 1.2$ mag). 0234+2438, the bluest source in this class, shows particularly strong Fe II, weak [O III] emission and weak X-ray emission, resembling the behavior of the Type 1s discussed above. Most objects (13/17) in this class have $N_H < $ few $\times 10^{21}$ cm^{-2}, consistent with the typical Type 1 values (Malizia et al. 1997). Four: $0420 - 2047$, $1027+1219$, $1659+1834$ and $0955+1705$, have $N_H \sim$ few $\times 10^{22}$ cm^{-2}, higher than the typical Type 1 value. The first three are high S/N (C) Chandra sources for which N_H was measured and shown to be the highest in the sample. $0955+1705$ is a low S/N (A) Chandra object with high $A_V = 15$ mag estimated from modeling of the optical/IR colors. The host galaxy contribution at R band, obtained from optical/IR color modeling, is <50% in about half (8/17) of these intermediate-type sources.

The group of Types 1.2–1.5 2MASS AGNs includes the highest number (5/17) of highly polarized ($5\% < P < 13\%$)

objects: ($0420 - 2047$, $0918+2117$, $0938+0057$, $1659+1834$, $2222+1952$). This is consistent with Smith et al. (2002) who find the highest polarization in intermediate-type objects. Only three AGNs from different optical types, $1516+1900$ (Type 1), $1049+5837$ (Type 1.8), and $0108+2148$ (Type 1.9), show high polarization ($P = 9.27$%, $P \geqslant 8$% and $P = 5.07$%, respectively).

8.3. The Types 1.8 and 1.9s

All spectra in F_λ versus λ are either flat (6/9) or red (3/9). Two objects, $0108+2148$ (Type 1.9) and $1049+5837$ (Type 1.8), in this class have high polarization ($P \geqslant 5$%). $1049+5837$ shows variations in the degree and position angle of polarization with wavelength implying two scattering components: one with $P \geqslant 8$% from material originating from the polar scattering lobes and the other dominating at $\lambda \lesssim 4500$ Å with $P \geqslant 20$% lying along a less reddened line of sight (Schmidt et al. 2007; complex absorbing and scattering properties are also visible in X-rays, Wilkes et al. 2008). The $B - R$ and $J - K_S$ colors of Types 1.8–1.9s, as expected, are redder than those of the Types 1–1.5 discussed above. Modeling of the optical/IR colors finds six moderately absorbed ($A_V = 3$–6 mag, i.e., $N_H = (4.8$–$9.7) \times 10^{21}$ cm^{-2}) and three highly absorbed

$(A_V = 10$ mag; $N_H = 1.6 \times 10^{22}$ cm^{-2}) sources with substantial ($>60\%$) host galaxy contribution at R band. An exception is 2024−5723 with a ~30% host galaxy contribution.

8.4. The Type 2s

This group of 11 objects includes the two reddest $J - K_S$ sources in our red 2MASS AGN sample: *0348+1255* and *1307+2338* ($J - K_S = 3.294$ and 3.314, respectively). Column densities obtained from X-ray spectral fitting and optical/ IR color modeling are $N_H = (0.7\text{–}3.5) \times 10^{22}$ cm^{-2}, which are at the low end of the N_H distribution for Seyfert 2s (Risaliti et al. 1999). Since typical, highly absorbed (i.e., edge-on $N_H \gtrsim 10^{23}$ cm^{-2}) Type 2s have AGNs completely obscured both in optical and NIR, their colors are consistent with pure host galaxy colors, i.e., $B - R = 1\text{–}1.8$ and $J - K_S = 0.8\text{–}1$. However, the low N_H, red 2MASS Type 2s are obscured at optical wavelengths, but not in the NIR, so the $J - K_S$ colors are dominated by the reddened AGN light and will be picked up by the red $J - K_S > 2$ mag selection. The host galaxy contribution in the red 2MASS Type 2s from optical/IR color modeling is strong and responsible for 76%–100% of the total observed flux at R band. This is also confirmed by strong galactic absorption lines, a 4000 Å dip in the optical spectra of *1453+1353* and *2225+1958*, and extended images on the B and R plates. Dilution by the large contribution of the host galaxy is likely to explain the low observed polarization of Type 2 red 2MASS AGNs (Smith et al. 2002, 2003).

Malizia et al. (1997) suggested that, since low-absorption ($N_H \sim 10^{22}$ cm^{-2}) Type 2 AGNs show little/no change in N_H over time, they must have an absorber lying further away from the nucleus, possibly in the host galaxy inclined to our line of sight. This may be the case in half of the red 2MASS Type 2 AGNs, which have typical Type 2 optical spectra with strong [O III] emission (*0050+2933, 1021+6311, 1300+1632, 1307+2338, 2225+1958*). The other half (*0157+1712, 1453+1353, 1755+6751*) have weak or nonexistent (*0348+1255, 1507−1225*) [O III] emission, implying either absorption closer to the nucleus (to dampen the ionizing photons before they reach the NLR), or perhaps a host galaxy absorber *and* an AGN with high $L/L_{\rm Edd}$, similar to the high $L/L_{\rm Edd}$ NLS1s and BALQSOs which have weak [O III] emission.

9. CONCLUSIONS

We have analyzed a sample of 44 AGNs selected from the 2MASS survey based on their red $J - K_S > 2$ color and later observed by *Chandra*. The sample includes a mixed bag of objects: seven Type 1s, whose spectra (except for one) resemble NLS1/BALQSOs (strong Fe II and weak [O III] emission), 11 Type 2s with relatively low (for Type 2s) $N_H < $ few $\times 10^{22}$ cm^{-2}, that allows the reddened AGN colors to dominate in the NIR, and 26 intermediate-type sources (1.2–1.9), where eight show high optical polarization.

The red $J - K_S$ selection picks AGNs in which circumnuclear and/or host galaxy obscuration result in unusually red NIR colors. It also picks high $L/L_{\rm Edd}$ Type 1 sources with hot circumnuclear dust emission. Sources which are obscured are most likely viewed at an intermediate angle, and offer an opportunity to study the contributions of weaker components that are normally outshone by the AGN light. The sample shows the following properties:
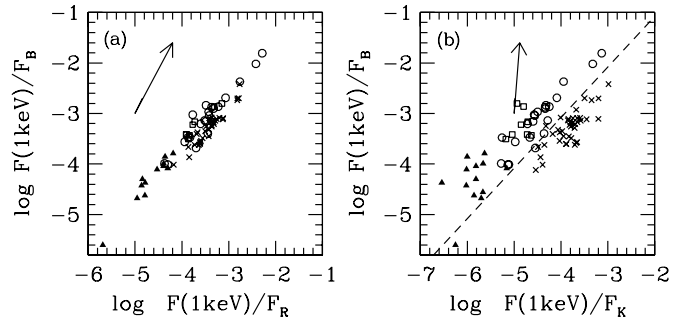

Figure 14. Relation between the intrinsic 1 keV X-ray flux to observed B flux ratio and the intrinsic 1 keV X-ray flux to observed R and K flux ratios. The X-ray flux is corrected for Galactic and intrinsic extinction while the B, R, and K fluxes are corrected only for Galactic extinction. The crosses represent optical/radio-selected AGNs from Elvis et al. (1994). The 2MASS sources are delineated by the S/N: high-S/N *Chandra* spectra (C fits) by circles, medium-S/N *Chandra* spectra (B fits) by squares, and low-S/N *Chandra* spectra (A fits) by filled triangles. The arrows indicate how the ratios change when intrinsic dust with $A_V = 3.1$ mag ($N_H = 5 \times 10^{21}$ cm^{-2} assuming a Milky Way dust-to-gas ratio) reddens the optical/IR fluxes. The dashed line in (b) shows the $B - K_S = 4.3$ color cut used to select the red 2MASS AGNs. 1258+2329 (object with lowest $F(1$ keV$)/F_B$) lies below this color cut, since SuperCOSMOS, not the USNO-A2 B magnitude (initially used for color selection), is used here to calculate the $F(1$ keV$)/F_B$ ratio.

1. The 2MASS AGN median SED is redder (by ~1 mag in $B - R$) in the optical/UV than the blue optically/radio-selected AGNs from Elvis et al. (1994), and redder than the hard-X-ray-selected AGNs from Kuraszkiewicz et al. (2003).

2. Seven of the 44 sample objects show pure AGN optical and IR colors (with $A_V = 0\text{–}1$ mag; SED and emission-line properties indicate high $L/L_{\rm Edd}$). The remaining sources show redder colors, which are modeled as a mixture of a reddened AGN ($A_V = 0\text{–}22$, i.e., $N_H \leqslant 4.2 \times 10^{22}$ cm^{-2}), host galaxy emission (approaching 100% at R band in 1/3 of the sample, with intrinsic AGN/host galaxy ratio = few to 40 at R band), and, in a few sources, AGN scattered light emission.

3. Sources with high polarization, when modeled, turn out to have a $<2\%$ scattered AGN light contribution at R relative to the intrinsic AGN light. The scattered light becomes significant as the direct AGN light is absorbed in our line of sight.

4. The column densities obtained from X-ray spectral fitting are between 10^{21} cm^{-2} and 7×10^{22} cm^{-2}. These values are consistent with those found from modeling of the optical/ NIR colors ($N_H \leqslant 4.2 \times 10^{22}$ cm^{-2}) and the far-IR *IRAS* colors where the 12 μm/60 μm and 25 μm/60 μm flux ratios give crude estimates of $N_H < 10^{23}$ cm^{-2}. The consistency of N_H values obtained from optical colors and X-ray spectral fitting is due to our detailed modeling of the optical colors, which accounts for the effects of reddening, host galaxy emission, and scattered AGN light emission. Without such detailed analysis, N_H values may disagree by up to 3 orders of magnitude (Maiolino et al. 2001).

5. The deficiency of low equivalent widths in the [O III] distribution, relatively to the LBQS and SDSS QSO samples, implies a predominance of inclined objects with intermediate viewing angles in the red 2MASS sample.

6. The analysis of SED and emission-line properties implies that the weakness of X-ray emission (low $F(1$ keV$)/F_K$ and $F(2\text{–}10$ keV$)/F([$O III$])$ ratios) shown by a large number of the red 2MASS AGNs (Wilkes et al. 2002) relative to the
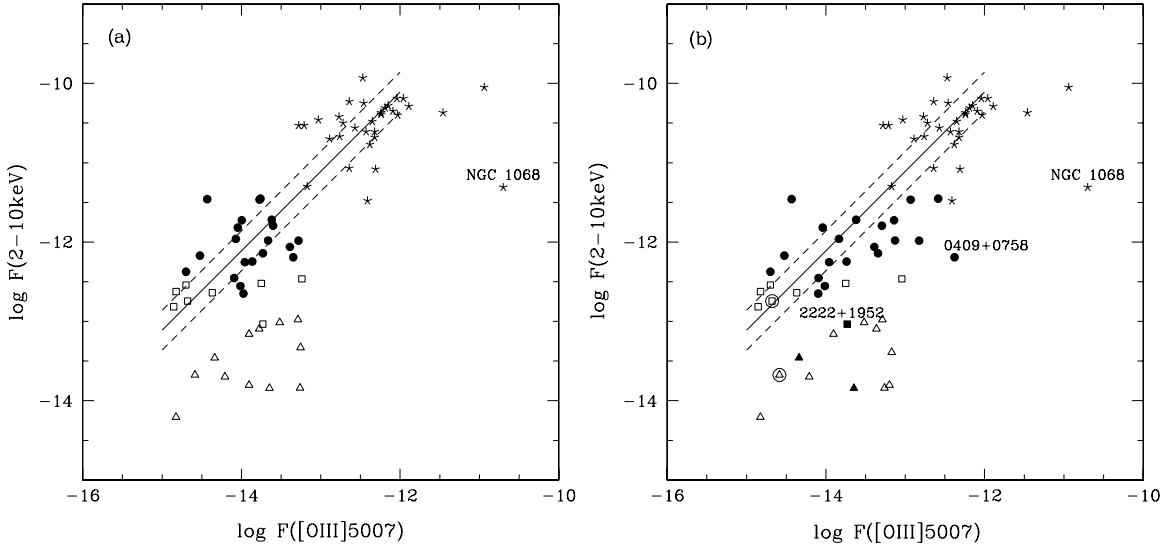
Figure 15. Relation between the narrow emission-line [O III] λ5007 flux and the hard-X-ray flux at 2–10 keV (corrected for intrinsic absorption): (a) with no reddening correction to [O III]; (b) applying a reddening correction based on the Hβ/Hα narrow-line ratio to the 2MASS AGN. In both plots, stars represent Seyfert 1s and 2s from Mulchaey et al. (1994). The 2MASS objects are delineated by their *Chandra* S/N classifications, with filled circles, open squares, and open triangles representing our 2MASS objects with *C* (highest S/N), *B* (medium S/N), and *A* (low S/N) spectral types, respectively. The filled triangles and squares represent the reddest $J - K_S$ > 3 objects. Two objects with undetermined reddening corrections (due to lack of Hβ emission) are surrounded by an open circle. The solid and dashed lines represent the mean $\log F[\text{O III}]/F(2\text{–}10\,\text{keV}) = -1.89 \pm 0.25$ found for Seyfert 1s and 2s in Mulchaey et al. (1994).
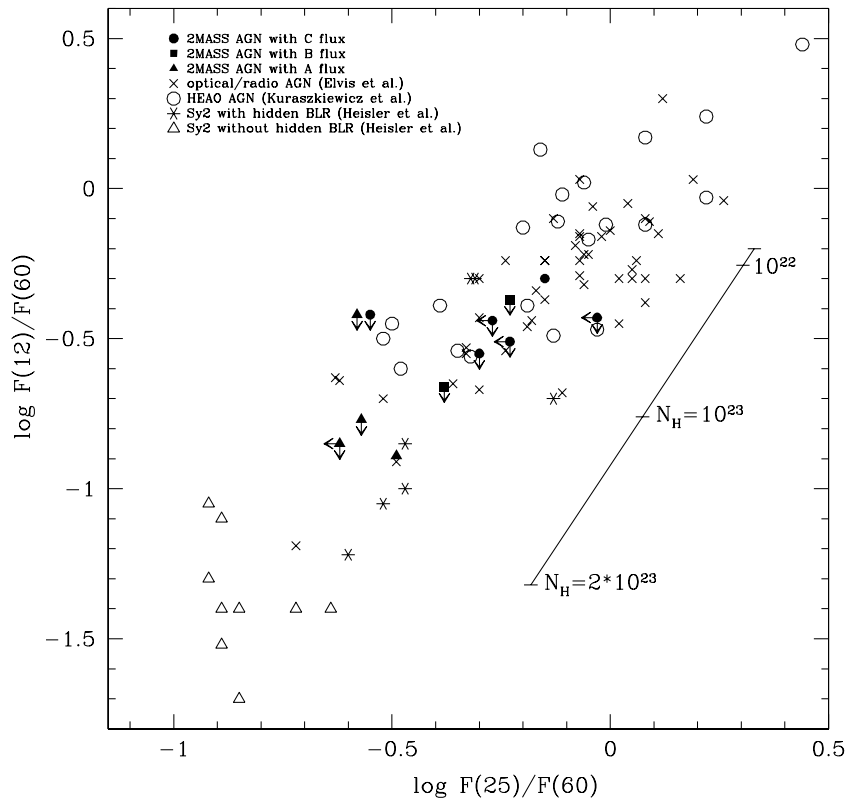
Figure 16. 12/60 vs. 25/60 flux ratios. Filled circles are 2MASS AGNs with high-S/N *Chandra* spectra (*C* flux), filled squares 2MASS AGNs with medium-S/N *Chandra* spectra (*B* flux), and filled triangles 2MASS AGNs with low-S/N *Chandra* spectra (*A* flux). X-ray-selected Seyferts from the *HEAO* sample (Kuraszkiewicz et al. 2003) are represented by open circles, blue QSOs from Elvis et al. (1994) by crosses, Seyfert 2s with a hidden broad line region by stars, and Seyfert 2s without a hidden broad line region (higher N_H) by open triangles (Heisler et al. 1997).

blue optically/radio-selected QSOs (Elvis et al. 1994) is due to either higher intrinsic obscuration or high L/L_{Edd} ratios, or both.

7. We find that objects with weak (relative to the BBB) X-ray emission (high obscuration or/and L/L_{Edd}) depart from the $F(2\text{–}10\,\text{keV})$ versus [O III] relation found for Seyfert 1s and 2s (Mulchaey et al. 1994) which limits its usefulness for estimating the AGN's intrinsic X-ray emission.
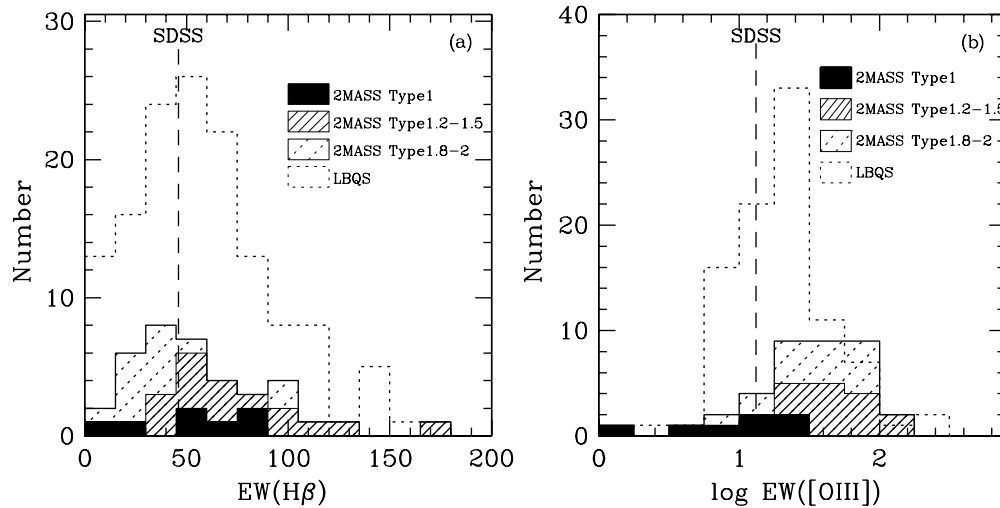
Figure 17. Comparison of the distributions of Hβ and [O III] emission-line equivalent widths between 2MASS AGNs (shaded areas) and LBQS sample (dotted line; Forster et al. 2001). The dashed lines show equivalent widths from the SDSS mean composite spectrum (Vanden Berk et al. 2001).

REFERENCES

Alexander, D. M., et al. 2003, AJ, 126, 539
Alonso-Herrero, A., Ward, M. J., & Kotilainen, J. K. 1997, MNRAS, 288, 977
Antonucci, R. 1993, ARA&A, 31, 473
Antonucci, R., & Miller, J. S. 1985, ApJ, 297, 621
Baker, J. 1997, MNRAS, 286, 23
Barkhouse, W. A., & Hall, P. B. 2001, AJ, 121, 2843
Barthel, P. D. 1989, ApJ, 336, 606
Bassani, L., Dadina, M., Maiolino, R., Salvati, M., Risaliti, G., dellaCeca, R., Matt, G., & Zamorani, G. 1999, ApJS, 121, 473
Bessell, M. S. 2005, ARA&A, 43, 293
Boller, Th., Brandt, W. N., & Fink, H. 1996, A&A, 305, 53
Boroson, T. A., & Green, R. F. 1992, ApJS, 80, 109
Boyle, B. J., & di Matteo, T. 1995, MNRAS, 277, L63
Burstein, D., & Heiles, C. 1978, ApJ, 225, 40
Buzzoni, A. 2005, MNRAS, 361, 725
Cardelli, J. A., Clayton, G. C., & Mathis, J. S. 1989, ApJ, 345, 245
Comastri, A., Setti, G., Zamorani, G., & Hasinger, G. 1995, A&A, 296, 1
Cutri, R. M., Nelson, B. O., Francis, P. J., & Smith, P. S. 2002, in ASP Conf. Proc. 284, AGN Surveys (Proc. IAU Colloquium 184), ed. R. F. Green, E. Y. Khachikian, & D. B. Sanders (San Francisco, CA: ASP) 127
Czerny, B., Loska, Z., Szczerba, R., Cukierska, J., & Madejski, G. 1995, AcA, 45, 623
Daddi, E., et al. 2008, ApJ, 670, 173
Dickey, J. M., & Lockman, F. J. 1990, ARA&A, 28, 215
Draine, B. T. 2003a, ARA&A, 41, 241
Draine, B.T. 2003b, ApJ, 598, 1017

Elvis, M., et al. 1994, ApJS, 95, 1
Feigelson, E. D., & Nelson, P. I. 1985, ApJ, 293, 192
Fiore, F., et al. 2008, ApJ, 672, 94
Forster, K., Green, P. J., Aldcroft, T., Vestergaard, M., Foltz, C. B., & Hewett, P. C. 2001, ApJS, 134, 35
Francis, P. J., Drake, C. L., Whiting, M. T., Drinkwater, M. J., & Webster, R. L. 2001, PASA, 18, 221
Francis, P. J., Nelson, B. O., & Cutri, R. M. 2004, AJ, 127, 646
Freeman, P., Doe, S., & Siemiginowska, A. 2001, Proc. SPIE 4477, 76
Gehrels, N. 1986, ApJ, 303, 336
Gilli, R., Comastri, A., & Hasinger, G. 2007, AA, 463, 79
Gilli, R., Risaliti, G., & Salvati, M. 1999, A&A, 347, 424
Hambly, N. C., Davenhall, A. C., Irwin, M. J., & MacGillivray, H. T. 2001a, MNRAS, 326, 1315
Hambly, N. C., Irwin, M. J., & MacGillivray, H. T. 2001b, MNRAS, 326, 1295
Hambly, N. C., et al. 2001c, MNRAS, 326, 1279
Heisler, C. A., Lumsden, S. L., & Bailey, J. A. 1997, Nature, 385, 700
Hines, D. C., Schmidt, G. D., Gordon, K. D., Smith, P. S., Wills, B. J., Allen, R. G., & Sitko, M. L. 2001, ApJ, 563, 512
Hutchings, J. B., Maddox, N., Cutri, R. M., & Nelson, B. O. 2003, AJ, 126, 63
Isobe, T., Feigelson, E. D., & Nelson, P. I. 1986, ApJ, 306, 490
Jester, S., et al. 2005, AJ, 130, 873
Kim, D.-W., & Elvis, M. 1999, ApJ, 516, 9
Kuraszkiewicz, J. K., Green, P. J., Crenshaw, D. M, Dunn, J., Forster, K., Vestergaard, M., & Aldcroft, T. L. 2004, ApJS, 150, 165
Kuraszkiewicz, J. K., Green, P. J., Forster, K., Aldcroft, T. L., Evans, I. N., & Koratkar, A. 2002, ApJS, 143, 257
Kuraszkiewicz, J. K., Wilkes, B. J., Czerny, B., & Marthur, S. 2000, ApJ, 542, 692
Kuraszkiewicz, J. K., Wilkes, B. J., Schmidt, G., Smith, P. S., Cutri, R. M., & Czerny, B. 2009, ApJ, 692, 1180
Kuraszkiewicz, J. K., et al. 2003, ApJ, 590, 128
Lacy, M., Petric, A. O., Sajina, A., Canalizo, G., Storrie-Lombardi, L. J., Armus, L., Fadda, D., & Marleau, F. R. 2007, AJ, 133, 186
Maddox, S. J., Efstathiou, G., Sutherland, W. J., & Loveday, J. 1990, MNRAS, 243, 692
Maddox, N., & Hewett, P. C. 2006, MNRAS, 367, 717
Maiolino, R., Marconi, A., Salvati, M., Risaliti, G., Severgnini, P., Oliva, E., La Franca, F., & Vanzi, L. 2001, A&A, 365, 28
Maiolino, R., Salvati, M., Bassani, L., Dadina, M., dellaCeca, R., Matt, G., Risaliti, G., & Zamorani, G. 1998, A&A, 338, 781
Malizia, A., Bassani, L., Stephen, J. B., Malaguti, G., & Palumbo, G. G. C. 1997, ApJS, 113, 311
Marble, A. R., Hines, D. C., Schmidt, G. D., Smith, P. S., Surace, J. A., Armus, L., Cutri, R. M., & Nelson, B. 2003, ApJ, 590, 707
Monet, D., et al. 1998, USNO-A2.0 Catalog of Astrometric Standards (Washington, DC: US Naval Obs.)
Moshir, M., et al. 1990, The IRAS Faint Source Catalog Version 2 (Pasadena, CA: IPAC)
Mould, J. R., et al. 2000, ApJ, 529, 786

Mulchaey, J. S., Koratkar, A., Ward, M. J., Wilson, A. S., Whittle, M., Antonucci, R. R. J., Kinney, A. L., & Hurt, T. 1994, ApJ, 436, 586

Osterbrock, D. E., & Pogge, R. W. 1985, ApJ, 297, 166

Polletta, M., et al. 2006, ApJ, 642, 673

Polletta, M., et al. 2007, ApJ, 663, 81

Pounds, K. A., Done, C., & Osborne, J. 1995, MNRAS, 277, L5

Pounds, K. A., & Wilkes, B. J. 2007, MNRAS, 380, 1341

Pounds, K. A., Wilkes, B. J., & Page, K. L. 2005, MNRAS, 362, 784

Ptak, A., Heckman, T., Levenson, N. A., Weaver, K., & Strickland, D. 2003, ApJ, 592, 782

Richards, G. T., et al. 2002, AJ, 123, 2945

Richards, G. T., et al. 2003, AJ, 126, 1131

Risaliti, G., Maiolino, R., & Salvati, M. 1999, ApJ, 522, 157

Rodriguez-Ardila, A., Contini, M., & Viegas, J.S. 2005, MNRAS, 357, 220

Rodriguez-Ardila, A., & Mazzalay, X. 2006, MNRAS, 367, L57

Rudy, R. J., Mazuk, S., Puetter, R. C., & Hamann, F. 2000, ApJ, 539, 166

Savage, B. D., & Mathis, J. S. 1979, ARA&A, 17, 73

Schmidt, G. D., Smith, P. S., Hines, D. C., Tremonti, C. A., & Low, F. J. 2007, ApJ, 666, 784

Schmidt, G. D., Stockman, H. S., & Smith, P. S. 1992, ApJ, 398, L57

Schneider, D. P., et al. 2007, AJ, 134, 102

Shakura, N. I., & Sunyaev, R. A. 1973, A&A, 24, 337

Skrutskie, M. F., et al. 2006, AJ, 131, 1163

Smith, P. S., Schmidt, G. D., Hines, D. C., Cutri, R. M., & Nelson, B. O. 2000, ApJ, 545, L19

Smith, P. S., Schmidt, G. D., Hines, D. C., Cutri, R. M., & Nelson, B. O. 2002, ApJ, 569, 23

Smith, P. S., Schmidt, G. D., Hines, D. C., & Foltz, C. B. 2003, ApJ, 593, 676

Soifer, B. T., et al. 1984, ApJ, 278, L71

Stark, A., Gammie, C. F., Wilson, R. W., B. J., Linke, R. A., Heiles, C., & Hurwitz, M. 1992, ApJS, 79, 77

Treister, E., et al. 2006, ApJ, 640, 603

Turner, T. J. 1999, ApJ, 511, 142

Turner, T. J., George, I. M., Nandra, K., & Mushotzky, R. F. 1997, ApJ, 113, 23

Vanden Berk, D. E., et al. 2001, AJ, 122, 549

Webster, R. L., Francis, P. J., Peterson, B. A., Drinkwater, M. J., & Masci, F. J. 1995, Nature, 375, 469

Weingartner, J. C., & Draine, B. T. 2001, ApJ, 548, 296

Weymann, R. J., Carswell, R. F., & Smith, M. G. A. 1981, ARA&A, 19, 41

White, N. E., Giommi, P., & Angelini, L. 1994, IAU Circ. 6100

Wilkes, B. J., Pounds, K. A., & Schmidt, G. D. 2008, ApJ, 680, 110

Wilkes, B. J., Schmidt, G. D., Cutri, R. M., Ghosh, H., Hines, D. C., Nelson, B., & Smith, P. S. 2002, ApJ, 564, L65

Wills, B. J., Netzer, H., & Wills, D. 1985, ApJ, 288, 9

Witt, H. J., Czerny, B., & Życki, P. 1997, MNRAS, 286, 848

Zakamska, N. L., et al. 2006, AJ, 132, 1496